Development of an ultra-low field magnetic resonance imaging scanner and DC SQUID based current sensors for the investigation of hyperpolarization techniques

Dissertation
der Mathematisch-Naturwissenschaftlichen Fakultät
der Eberhard Karls Universität Tübingen
zur Erlangung des Grades eines
Doktors der Naturwissenschaften
(Dr. rer. nat.)

vorgelegt von
Matthias Rudolph
aus Stuttgart

Tübingen
2017

Gedruckt mit Genehmigung der Mathematisch-Naturwissenschaftlichen Fakultät der Eberhard Karls Universität Tübingen.

Tag der mündlichen Prüfung:	15.12.2017
Dekan:	Prof. Dr. Wolfgang Rosenstiel
1. Berichterstatter:	Prof. Dr. Dieter Kölle
2. Berichterstatter:	Prof. Dr. Reinhold Kleiner

Kurzfassung

Kernspinresonanzspektroskopie und Kernspinresonanztomographie sind etablierte Verfahren in der Strukturanalyse und der medizinischen Bildgebung. Aufgrund der hohen Kosten bei der Anschaffung und dem Betrieb der Spektrometer und Tomographen, welche hauptsächlich aus den benötigten supraleitenden Elektromagneten resultieren, gibt es ein wachsendes Interesse an kostengünstigen Geräten. Spektrometer und Tomographen auf Basis von normalleitenden Elektromagneten erlauben kostengünstige Systeme, was jedoch aufgrund der niedrigeren Magnetfeldstärke und einer damit einhergehenden niedrigeren Probenpolarisierung zu Lasten des Messsignals geht. Um Signalverluste teilweise zu kompensieren werden in Niederfeldsystemen Detektoren auf Basis von gleichstrombetriebenen (DC) supraleitenden Quanteninterferometern (SQUIDs) verwendet, welche eine deutlich höhere Empfindlichkeit als konventionelle Detektionsspulen aus Kupfer besitzen. Zusätzlich bieten neuartige Hyperpolarisierungsmethoden auf Basis von Parawasserstoff, welche bei niedrigen Magnetfeldstärken im Bereich weniger mT anwendbar sind, die Möglichkeit, die Probenpolarisierung durch die Übertragung der Spinordnung von Parawasserstoff-Kernen auf Wasserstoff-Kerne der Probe um mehrere Grössenordnungen zu erhöhen. Zur erfolgreichen Hyperpolarisierung der zu untersuchenden Proben werden Polarisierungstransfer-Katalysatoren benötigt.

In dieser Arbeit wird zum Einen die Konzeption und der Aufbau eines Ultra-Niederfeld Kernspinresonanzspektrometers/-tomographen mit einem DC SQUID basierten Magnetfeldsensor zur kontrollierten Charakterisierung von neu entwickelten Polarisierungstransfer-Katalysatoren für Hyperpolarisierungsanwendungen vorgestellt. Der gesamte Aufbau wurde durch weitestgehende Vermeidung von metallischen Komponenten auf möglichst niedrige Magnetfeldrauschwerte $S_B^{1/2}$ und homogene Magnetfelder hin op-

timiert, was sich in einem Magnetfeldrauschen $S_B^{1/2} = 1.15\,\mathrm{fT/Hz^{1/2}}$ im Bereich weißen Rauschens und Linienbreiten der Kernspinresonanz $< 1\,\mathrm{Hz}$ zeigt.

Zum Anderen wurden im Rahmen der Arbeit DC SQUID basierte Stromsensoren zur Erfassung der Kernspinresonanz-Signale entworfen, welche auf dem Niedertemperatur-Supraleiter Niob basieren. Dabei konnte sowohl ein Supraleiter/Normalleiter/Supraleiter (SNS) als auch auf einen Supraleiter/Isolator/Supraleiter (SIS) Trilagen-Herstellungsprozess zurückgegriffen werden. Der Stromsensorentwurf wurde an die kritische Stromdichte j_c des jeweiligen Herstellungsprozesses angepasst, was in unterschiedlichen SQUID-Entwürfen und Ankoppelschemata der Signalaufnehmer-Spulen an das SQUID resultiert. Transport- und Rauscheigenschaften wurden bei einer Temperatur von $T = 4.2\,\mathrm{K}$ bestimmt. Für die SNS basierten Stromsensoren konnte eine Eingansempfindlichkeit $1/M_{in} = 37.8\,\mu\mathrm{A}$ gefunden werden, was in Kombination mit einem Flussrauschen $S_\Phi^{1/2} = 590\,\mathrm{n\Phi_0/Hz^{1/2}}$ im Bereich weißen Rauschens zu einer Stromempfindlichkeit $S_i^{1/2} = 21.9\,\mathrm{pA/Hz^{1/2}}$ führt. Mit SIS basierten Stromsensoren konnte eine Eingangsempfindlichkeit $1/M_{in} < 1\,\mu\mathrm{A}$ erreicht werden. Die tatsächliche Stromempfindlichkeit konnte jedoch nicht bestimmt werden, da aufgrund von herstellungsbedingten Schichtisolationsproblemen sehr hohe Flussrauschwerte resultierten.

Anhand von hyperpolarisiertem Pyridin konnte ein Signalverstärkungsfaktor von ≤ 200 gegenüber thermisch polarisiertem Pyridin gemessen werden. Daran anschließend wurden drei weitere Probensubstanzen untersucht, welche sowohl ^{1}H- als auch ^{19}F-Kerne enthalten und in Hochfeldmessungen vielversprechende Resultate zeigten. Dabei zeigten zwei Probensubstanzen ein Verhalten des Polarisationstransfers, welches mit der etablierten Theorie auf Basis von J-Kopplung erklärt werden kann. Die dritte Probe hingegen zeigt ein Verhalten, was nicht mit J-Kopplung der Kerne erklärt werden kann und auf alternative Hyperpolarisierungsmechanismen schließen lässt.

Contents

1 Introduction

Since the discovery of nuclear magnetic resonance (NMR) by Edward M. Purcell and Felix Bloch in 1946 [PTP46, BHP46], NMR spectroscopy and magnetic resonance imaging (MRI) have developed to important and reliable tools in research and healthcare. Proton spins are polarized along a static magnetic field $\vec{B}_0$ which leads to a sample magnetization $\vec{M}$. The magnetization $\vec{M}$ can be manipulated to precess about $\vec{B}_0$ by means of an excitation magnetic field $\vec{B}_1$ oscillating with the proton Larmor frequency $\omega_L = \gamma|\vec{B}_0|$, where $\gamma/2\pi = 42.576\,\mathrm{MHz/T}$ is the gyromagnetic ratio. NMR spectroscopy has become one of the most important tools in structure analysis for chemists and pharmacists (since it allows the precise determination of the atomic composition of molecules). Further, MRI became one of the most important and powerful imaging techniques in medical diagnosis. MRI offers superior contrast and unmatched image quality for soft tissue for which reason it is commonly employed for the noninvasive examination of organs. In combination with electrocardiography or electroencephalography it is also employed for functional anatomical research [LDH06].

A high spatial resolution and signal-to-noise ratio (SNR) is achieved by utilizing high magnetic fields. Typical clinical MRI scanners are equipped with electromagnets which generate 1.5 T, while more modern scanners reach 3 T or even 7 T. NMR spectrometers reach even higher fields (up to 23.5 T) due to a smaller bore of the coil used. The ongoing endeavor for even higher magnetic fields relies on the utilized signal detection scheme and the increasing polarization of the sample, respectively. On the one hand, the signal detection relies on Faradays law of inductance and incorporates coils made of copper wire as part of a tuned tank circuit. Higher fields lead to higher Larmor frequencies ω_L and consequently to a larger

induced oscillating voltage output of the detection coil $V \propto \omega_0 M$. On the other hand, an increase in the magnetic field strength linearly increases the sample polarization. Since both M and ω_0 scale with B_0, the detected signal V roughly scales as B_0^2. Higher magnetic fields, however, are literally paid dearly since practical electromagnet realizations employ superconducting coils. Full-body MRI scanners roughly cost $1 million per Tesla, mostly owed to the superconducting magnets. Due to this downside and an increasing global demand for healthcare in the same turn, the development of low and ultra-low field (ULF) MRI scanners with measurement fields below 0.5 T, often even below 1 mT, has begun over 20 years ago [Sep96]. Besides the cost advantage, low and ultra-low field (ULF) offer very interesting prospects like hybrid systems that allow both MRI and Magnetoencephalography (MEG) measurements [VNZ+13], imaging in the vicinity of metals [MHM+06] or a drastically greater difference in the longitudinal relaxation time T_1 of different tissue types [LMM+05, BHM+12].

However, due to the lower field strength the Larmor frequency and especially the sample polarization drops. This becomes problematic especially when dealing with very low field strength below 25 mT due to noise arising from the detection coil windings, in addition to its high pass behavior [Mye06]. Therefore, low field scanners are typically equipped with superconducting quantum interference device (SQUID) based detectors operated at a temperature $T = 4.2\,\mathrm{K}$. SQUIDs are not only amongst the most sensitive detectors for magnetic flux and show very low noise figures but also detect the field directly instead of its time derivative and offer a frequency independent sensitivity [KEMV14, CB04].

To counteract the signal loss, two strategies have been developed. The first strategy employes a relatively high prepolarization magnetic field of the order of $10 - 200\,\mathrm{mT}$ which will be turned off right before the data acquisition at measurement fields below 1 mT. This allows both relatively high sample polarizations while maintaining the mentioned advantages of the ULF regime. The effectiveness of this approach has been demonstrated impressively, for instance, by the group of J. Clarke at the UC Berkeley. They were able to perform promising MRI scans of a pepper belt, a human head and a human knee at fields below $150\,\mu\mathrm{T}$ [MHM+06, Mye06, IBS+13].

The second approach to enhance the signal relies on so-called hyperpolarization techniques, which are fairly new in this context [BSB+96, HCH+09, ZOM+10, BSH+13, HSL+13]. The term hyperpolarization refers to a sample polarization which drastically exceeds the so-called thermal polariza-

tion predicted by Curie's Law for a given temperature T and magnetic field B_0. Various hyperpolarization techniques exist and utilize different physical effects to achieve the non-thermal polarization, yet they all lead to a drastically boosted sample polarization by a few orders of magnitude. The breakthrough of these techniques was impeded by three main issues: a limited polarization lifetime, the necessity of external polarizer devices and its single-shot characteristics. Recent advances allow for a relatively high hyperpolarization repetition rate of just a few seconds and long life times of the polarization. Zotev et al. reported a signal enhancement of up to 100 for a hyperpolarization technique based on the nuclear Overhauser effect [ZOM+10]. Hövener et al. implemented a practically continuous hyperpolarization technique based on parahydrogen (pH_2) named signal amplification by reversible exchange (SABRE), which allows for signal enhancements of over 1000 [HSL+13, HKS+14]. Additionally, both techniques perform ideally in the ULF regime $B_0 < 10\,\mathrm{mT}$ which renders them as a perfect tool for ULF NMR/MRI experiments. However, both hyperpolarization techniques require chemical substances or a polarization transfer catalyst to make the hyperpolarization possible. This has turned out to be a huge obstacle for the adaption of this techniques for *in vivo* applications because the substances are not biocompatible due to poisonous solvents. The possible advantages, however, have drawn much attention by chemists, resulting in the development of new substances with the goal of biocompatibility.

Therefore, to investigate the hyperpolarizability of newly developed substances and transfer catalysts at ultra-low magnetic fields it was the goal of our[1] collaboration to develop and build a low magnetic field noise NMR/MRI spectrometer which employs a direct current (DC) SQUID as detector. The goals of this thesis are twofold. The first goal is the creation of a NMR/MRI spectrometer. The complete system design, realization and characterization has been performed by the author, in close collaboration with Dr. Kai Buckenmaier of the Max Planck Institute for Biological Cybernetics, and will be described. The system design also features the complete infrastructure needed for the investigation of a hyperpolarization technique based on pH_2. The pH_2 based hyperpolarization technique SABRE has been chosen for a first implementation of the hyperpolarization

[1] Max Planck Institute for Biological Cybernetics Tübingen, Institute of Physics Tübingen, Institute of Inorganic Chemistry Tübingen

technique due to the high signal enhancement factors reported in literature [LAB+12, HSL+13, LAB+14]. However, the system design is strictly kept as flexible as possible to allow for an easy implementation of other hyperpolarization techniques. Further, in the scope of *in vivo* measurements of promising transfer catalysts, the burden for the specimen under test should be kept as low as possible. The measurement time should be as short as possible. This requires both very low detector noise as well as low environmentally caused noise. Therefore, the second goal of this thesis is the design of ultra-low magnetic flux noise DC SQUID based current sensors. An experimental detector implementation relying on cross correlation of various detector channels is designed to cancel out environmentally caused noise [KE16]. In addition, to provide the possibility of an increased field of view (FOV) in MRI measurements, conventional SQUID based current sensors are designed which offer the needed feedback mechanisms for proper multi channel operation.

The thesis is divided into four main parts. It starts with the basic principles of superconductivity, DC SQUID based magnetic field sensors, NMR and the hyperpolarization technique used. This is followed by a detailed explanation of the involved fabrication processes of the DC SQUID as well as a presentation and characterization of the designed devices. Subsequently, all components of the constructed NMR/MRI system will be explained and characterized in detail and first NMR measurements will be presented. The thesis closes with a detailed series of measurements on three different hyperpolarization substances and a discussion of the results.

2 | Basics

2.1. Basics of superconductivity

2.1.1. Superconductivity

Superconductivity is a low temperature phenomenon, where the electrical resistance vanishes below a material specific critical temperature T_c. It was first observed in 1911 by Heike Kamerling Onnes who performed transport measurements on mercury while cooling it down to $T = 4.2\,\mathrm{K}$, the temperature of liquid helium [KO11]. Walther Meissner and Robert Ochsenfeld discovered in 1933 on tin and lead samples a second effect, characteristic for superconductors. When superconductors are cooled below their critical temperature T_c, they expel an applied magnetic Field $\vec{B}$ almost completely and maintain this field free state up to a critical magnetic field $\vec{B}_c$ [MO33]. In this so-called Meissner state, superconductors show a magnetic susceptibility $\chi = -1$, thus they are often referred to as perfect diamagnets. The Meissner state does not depend on the order of applying a magnetic field and subsequent cooling below T_c or vice versa. This proves that the superconducting state is a real thermodynamic phase. For a hypothetical ideal conductor with the specific resistance $\rho = 0$ below T_c, the Meissner state would not be present, thus the sequence of applying a magnetic field and subsequent cooling below T_c or vice versa is of importance [MO33].
In the framework of the phenomenological London theory, which is based on classical electrodynamics, the Meissner state could be explained [LL35]. Inside the superconductor the magnetic field decays exponentially at the scale of the London penetration depth $\lambda_L = \sqrt{m_s/\mu_0 n_s q_s^2}$, with μ_0 the permeability of free space, m_s the mass, n_s the density and q_s the charge of superconducting charge carriers. λ_L is a material specific quantity and

varies between a few tens up to several hundred nano meters [BK13].
In 1957, Bardeen, Cooper and Schrieffer proposed the BCS theory, a microscopic theory of superconductivity based on quantum mechanics [BCS57]. Below T_c, the theory assumes an attractive interaction between two conduction electrons that is mediated via phonons. These two electrons form a so-called Cooper pair which are the charge carriers in superconductors, therefore $q_s = 2\,e$ with $e = 1.602 \cdot 10^{-19}\,\mathrm{C}$. They have opposed spins $\vec{s}$ and canonical momentum $\vec{p} = \hbar\vec{k}$, with $\vec{k}$ the wave vector of the electron and $\hbar = h/2\pi$ the reduced Planck constant. The total spin and total momentum of a Cooper pair is zero. The entirety of Cooper pairs forms a macroscopic wave function

$$\Psi(\vec{r},t) = |\Psi(\vec{r},t)|\, e^{i\varphi(\vec{r},t)} = \sqrt{n_s(\vec{r},t)}\, e^{i\varphi(\vec{r},t)}. \tag{2.1}$$

Here, $|\Psi(\vec{r},t)|^2 = n_s(\vec{r},t)$ is the position and time dependent Cooper pair density and $\varphi(\vec{r},t)$ is the phase of the wave function, describing the center-of-mass motion of all pairs.

2.1.2. Fluxoid quantization

The existence of the phase coherent macroscopic wave function immediately introduces a quantization. If one considers a superconducting ring structure, a superconducting current can be induced by an applied magnetic flux density $\vec{B}$ which is not decaying due to $\rho = 0$ [GM12]. To achieve a non-decaying supercurrent, the macroscopic wave function has to be single valued at any point in space $\vec{r}$ at any time t. Thus, the change in phase of the macroscopic wave function $\vec{\nabla}\varphi$ in a closed path C around the ring has to obey the condition

$$\oint_C \vec{\nabla}\varphi\, d\vec{l} = n\,2\pi. \tag{2.2}$$

with $n \in \mathbb{Z}$. Using the canonical momentum $\vec{p}/\hbar = \vec{\nabla}\phi = q_s\vec{A}/\hbar + m_s\vec{j}_s/q_s\hbar$ where $\vec{A}$ is the vector potential and $\vec{j}_s$ the superconducting current density [Tin96], this leads to

$$n\,2\pi = \frac{q_s}{\hbar}\oint_C \vec{A}\, d\vec{l} + \frac{m_s}{q_s\,\hbar}\oint_C \vec{j}_s\, d\vec{l}. \tag{2.3}$$

Employing Stoke's theorem and the definition of λ_L yields the fluxoid quantization:

$$n\,\Phi_0 = \Phi_a + \mu_0 \lambda_L^2 \oint_C \vec{j}_s\, d\vec{l}, \tag{2.4}$$

with $\Phi_0 = h/2e \approx 2.07 \cdot 10^{-15}$ Vs being the magnetic flux quantum and Φ_a the magnetic flux applied to the ring. If a closed path is considered, which is far away ($\gg \lambda_L$) from the superconductor surface, the supercurrent density j_s vanishes. Then the fluxoid quantization (2.4) can be reduced to the flux quantization

$$\Phi_a = n\,\Phi_0. \tag{2.5}$$

2.2. Type-I and type-II superconductors

Shubnikov found in 1937 that a variety of superconductors show a behavior that differs from the Meissner state [SKSR37]. It was observed that these superconductors expel applied magnetic fields $|\vec{B}_a|$ completely only up to a material specific threshold field strength $|\vec{B}_{c1}|$. If the applied magnetic field gets increased further, however, the superconductor does not become normal conducting but gets penetrated by magnetic flux while still maintaining the zero-resistance state. This state is referred to as the Shubnikov phase. The superconductivity eventually breaks down for applied magnetic fields $|\vec{B}_{c2}| > |\vec{B}_{c1}|$. Superconductors showing this behavior are referred to as type-II superconductors while superconductors showing the conventional behavior are called type-I superconductors. A schematic phase diagram of both superconductor types is shown in Fig. 2.1. Abrikosov gave an explanation for the observed behavior within the framework of the phenomenological Ginzburg-Landau (GL) theory [Abr57, GL50]. The GL theory is based on two coupled differential equations with two important variables: the density of superconducting charge carriers $\vec{j}(\vec{r})$ and the order parameter $\Psi(\vec{r})$, which identifies with the macroscopic wave function of equation (2.1). Additionally, the GL theory incorporates two characteristic length scales. The first length scale relates to $\vec{j}(\vec{r})$ and identifies with the already mentioned London penetration depth λ_L. The other length scale is the so-called coherence length ξ_{GL} which describes the length on which variations of $\Psi(\vec{r})$ are counterbalanced. The Ginzburg-Landau parameter, given by

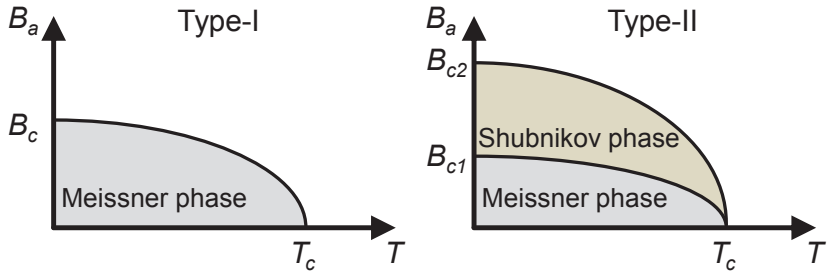

Figure 2.1.: Schematic phase diagram of type-I (a) and type-II (b) superconductors.

the ratio of both length scales, allows for a differentiation between type-I and type-II superconductors:

$$\kappa = \frac{\lambda_L}{\xi_{\mathrm{GL}}}. \tag{2.6}$$

Type-I superconductors show a value of $\kappa < 1/\sqrt{2}$ while type-II superconductors exhibit $\kappa > 1/\sqrt{2}$. Abrikosov found, that for a type-II superconductor in case of applied magnetic fields $|\vec{B}_{\mathrm{a}}| < |\vec{B}_{\mathrm{c1}}|$ it is energetically more favorable to allow magnetic flux to enter the superconductor. This leaves the superconductor segmented into superconducting and normal conducting regions. Flux penetrates the superconductor at the normal conducting region (the core) of so-called Abrikosov vortices. The normal conducting core has a diameter of $2\xi_{\mathrm{GL}}$ where $\Psi(\vec{r})$ is suppressed completely. The vortex cores are surrounded by a superconducting circulating current. Each vortex holds exactly one Φ_0 of magnetic flux. Figure 2.2 schematically shows a cross section of a vortex.

2.3. Josephson junctions

In 1962, Josephson predicted that Cooper pairs can tunnel between two superconductors that are separated by a thin insulating barrier, forming a Josephson junction (JJ) [Jos62]. Such a JJ offers quite unique transport characteristics. The macroscopic wave functions of the two superconductors Ψ_1 and Ψ_2 decay exponentially into the barrier. If the barrier is thin

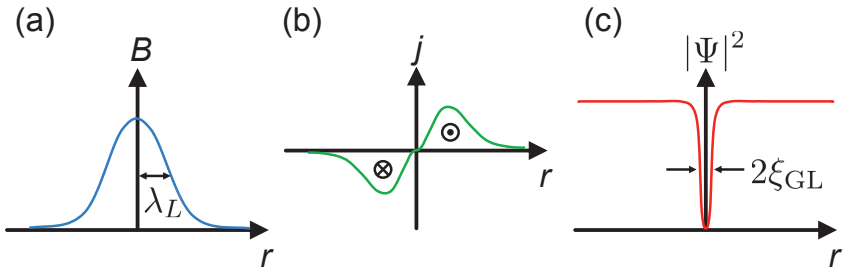

Figure 2.2.: Schematic cross section of a vortex. Magnetic flux density (a), density of superconducting charge carriers (b) and cooper pair density (c) vs. the distance r from the vortex center.

enough that both wave functions overlap and weakly couple, a superconducting tunneling current I_s can flow across the barrier which offers quite unique transport characteristics (cf. Fig. 2.3). I_s is described by the 1. Josephson equation

$$I_s = I_0 \sin\delta. \tag{2.7}$$

Here, $I_0 = j_0 \cdot A_{\mathrm{JJ}}$ is the maximum supercurrent (at $T = 0\,\mathrm{K}$) that depends on the critical supercurrent density j_0 as well as on the area A_{JJ} of the JJ and is carried solely by Cooper pairs. δ is the phase difference of the two macroscopic wave functions φ_1 and φ_2 and a contribution originating from the vector potential $\vec{A}$, given by

$$\delta = \varphi_2 - \varphi_1 - \frac{q_s}{\hbar} \oint A_x \, dx. \tag{2.8}$$

Assuming that a current $I > I_0$ is applied to the JJ, in addition to I_s a quasiparticle (i.e. unpaired, single electrons) current I_{qp} occurs, that leads to a voltage drop U across the JJ. The phase difference of the JJ becomes time dependent and is governed by the 2. Josephson equation

$$\frac{\mathrm{d}\delta}{\mathrm{dt}} = \frac{2\pi}{\Phi_0} U. \tag{2.9}$$

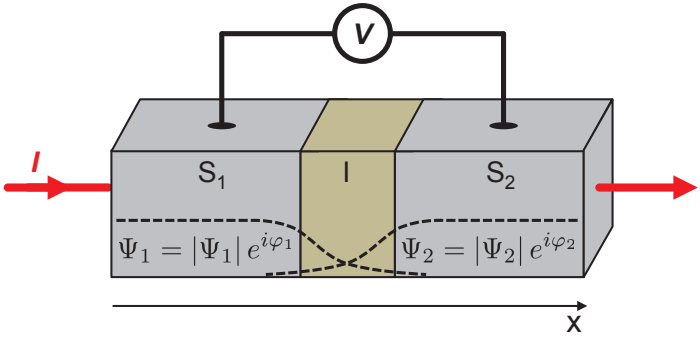

Figure 2.3.: Schematic illustration of a Josephson junction. The two superconductors are separated by a thin, insulating layer. The macroscopic wave functions of both superconductors are indicated by the dashed lines.

For a nonzero time averaged voltage $V = \langle U \rangle$ the phase difference grows in time, leading to supercurrents oscillating with a frequency

$$f_{\mathrm{JJ}} = \frac{V}{\Phi_0} \approx 483.6 \, \frac{\mathrm{GHz}}{\mathrm{mV}} \, V. \tag{2.10}$$

Already in 1963 the Josephson effect was experimentally observed by Anderson and Rowell on a JJ based on tin and lead, separated by a thin tin oxide layer [AR63]. Today, a variety of possible realization methods for JJs exist, involving a variety of barrier layers, e.g. also normal conducting metals [BK13]. The most commonly used JJ type, however, is based on a multilayer thin-film technology employing the superconductor niobium in combination with aluminum oxide barriers which allows for very well defined junction parameters (cf. chapter 3.1).
To describe the $I-V$ characteristics of such a JJ, the resistively and capacitively shunted junction (RCSJ) model is employed [Ste68, McC68]. Here, the JJ is modeled by four current contributions to the current I through the junction (cf. Fig. 2.4). The first current term originates from the supercurrent and is given by $I_s = I_0 \sin\delta$. The second term comes from the layer structure, which resembles a plate capacitor with the displacement current $I_d = C \, \mathrm{d}V/\mathrm{d}t$. The third contribution arises from the resistance R of the tunnel barrier for quasi particles $I_{qp} = V/R$. The last contribution emerges for temperatures $T > 0\,\mathrm{K}$, where a thermally induced noise current

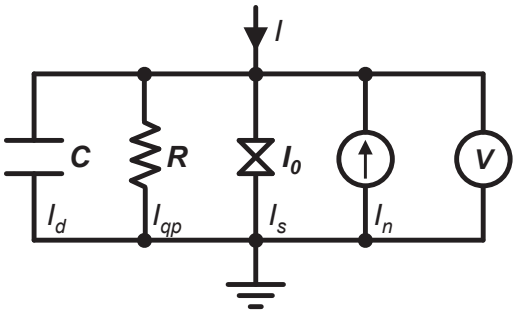

Figure 2.4.: Equivalent circuit of a Josephson junction in the framework of the RCSJ model.

$I_n(t)$ from the resistor with a power spectral density $S_{i,n} = 4k_BT/R$ (with Boltzmann's constant $k_B = 1.38 \cdot 10^{-23}\,\mathrm{J/K}$) is present [Joh28, Nyq28]. Employing Kirchhoff's law, the 1. and 2. Josephson equation, a differential equation for the phase difference δ is found

$$I = I_0 \sin\delta + \frac{\Phi_0}{2\pi R}\dot{\delta} + \frac{C\Phi_0}{2\pi}\ddot{\delta} + I_n(t). \tag{2.11}$$

By normalizing all currents to I_0 ($i = I/I_0$ and $i_n = I_n/I_0$), the time to $\tau = 1/\omega_c = \Phi_0/(2\pi I_0 R)$, voltages to $u = I_0 R$ and by introducing the Josephson plasma frequency $\omega_p = \sqrt{2\pi I_0/\Phi_0 C}$, equation (2.11) simplifies to

$$i = \sin\delta + \dot{\delta} + \beta_C\ddot{\delta} + i_n(t). \tag{2.12}$$

Here, the Stewart-McCumber parameter $\beta_C = 2\pi I_0 R^2 C/\Phi_0$ is introduced. β_C describes the damping behavior of the JJ and is often simply referred to as damping parameter. For $\beta_C < 0.7$ the case of strong damping is present. Here, the JJ shows non-hysteretic behavior, offering single valued $I(V)$ characteristics. Non-hysteretic behavior is desired when implementing JJs in sensor applications like SQUIDs (cf. chap. 2.4). If $\beta_C > 0.7$, the junction is in the underdamped regime and shows hysteretic behavior and non-single valued $I(V)$ characteristics. Fig. 2.5 shows the influence of β_C on the $I(V)$ characteristics. β_C is usually tuned to the desired value by a resistor in the range of a few Ω connected in parallel to shunt the junction. Due to

the large tunnel junction resistance in the range of a few Ω, practically, β_C is determined solely by the shunt resistor. The influence of the finite

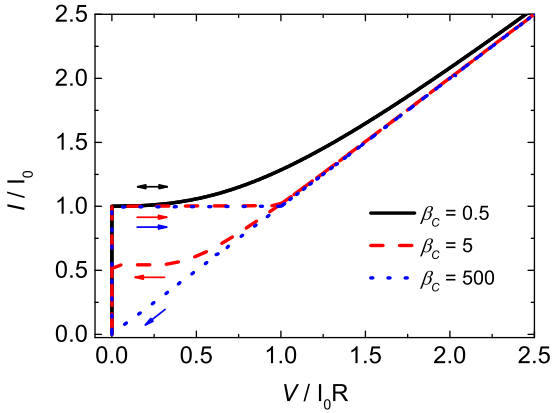

Figure 2.5.: Numerical simulation results of equation (2.11) and (2.12) showing the influence of the Stewart-McCumber parameter β_C on the $I(V)$ characteristics of a Josephson junction.

temperature $T > 0\,\mathrm{K}$ is captured by the noise parameter

$$\Gamma = \frac{2\pi k_B T}{I_0 \Phi_0} = \frac{E_T}{E_J} = \frac{I_{th}}{I_0}. \tag{2.13}$$

Γ is defined by the ratio of the thermal energy $E_T = k_B T$ and the Josephson coupling energy $E_J = I_0 \Phi_0 / 2\pi$, however, it can also be interpreted as the ratio of the thermally induced noise current $I_{th} = 2\pi k_B T / \Phi_0$ of the resistor and the critical current I_0 at $T = 0\,\mathrm{K}$ [CB04]. Since in experiments the temperature T is always greater than $T = 0\,\mathrm{K}$, the noise parameter $\Gamma > 0$. Subsequently, for bias currents I close to I_0, small noise currents I_{th} can push the JJ into the resistive state. As a consequence the critical current $I_c(T)$ of the JJ is always less than I_0. As can be seen in Fig. 2.6, already for very small values of $\Gamma = 0.05$ a quite drastic so-called noise rounding of the $I(V)$ curve can be observed whereas for $\Gamma = 1$ the Josephson effect is completely suppressed.

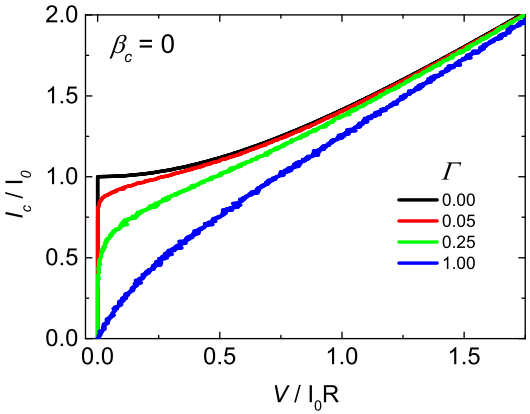

Figure 2.6.: Influence of the noise parameter Γ on the $I(V)$ characteristics for $\beta_C = 0$ (numerical simulations).

2.4. DC SQUIDs

Superconducting quantum interference devices (SQUIDs) consist of a superconducting ring with inductance L (cf. 2.7(b)) intersected by either one (radio frequency (RF) SQUID) or two JJs (DC SQUID) [CB04]. In this work, however, only the latter devices are of interest. DC SQUIDs combine the fluxoid quantization (cf. chapter 2.1.2) and the Josephson effect and were first realized by Jaklevic et al. in 1964 [JLSM64]. DC SQUIDs are extremely sensitive detectors for magnetic flux, capable of detecting changes of magnetic flux down to a few tens parts in a billion of Φ_0 [VAE+13]. Fig. 2.7 shows a schematic layout of a DC SQUID (a) and the corresponding RCSJ equivalent circuit (b). The SQUID is biased with a bias current I that splits up into two currents, I_1 flows through JJ_1 and I_2 which flows through JJ_2. If the SQUID is penetrated by the magnetic flux Φ_a induced by an applied magnetic field $\vec{B}$, a circulating screening current J is induced. Using J, the two currents I_1 and I_2 can be rewritten to

$$I_1 = \frac{I}{2} + J \quad , \quad I_2 = \frac{I}{2} - J. \tag{2.14}$$

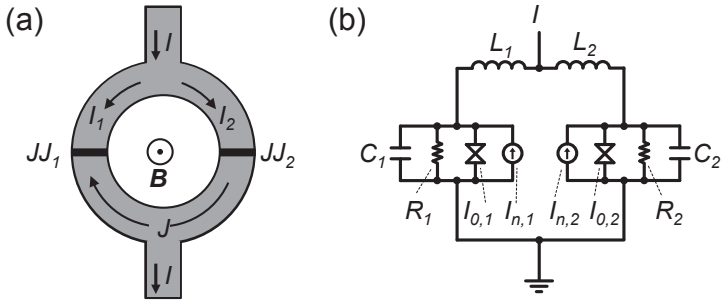

Figure 2.7.: Schematic illustration of a SQUID (a) and its equivalent circuit in the RCSJ model (b).

In combination with the 1. Josephson equation and the assumption of identical (i.e. symmetric) JJ parameters, this leads to

$$\frac{I}{2} + J = I_0 \sin\delta_1 \ , \ \frac{I}{2} - J = I_0 \sin\delta_2. \tag{2.15}$$

To analyze the influence of the applied flux Φ_a to the phase differences across both JJs in the DC SQUID, the fluxoid quantization (2.3) is used. Evaluating the line integral using a closed path within the SQUID including the phase contributions of the JJs by employing equation (2.8), for the phase differences

$$\delta_2 - \delta_1 = \frac{2\pi}{\Phi_0}\Phi_{\text{tot}} = \frac{2\pi}{\Phi_0}(\Phi_a + LJ) \tag{2.16}$$

can be found. Here, $\Phi_{\text{tot}} = \Phi_a + LJ$ is the sum of the applied flux Φ_a and the flux caused by the screening current J via the SQUID inductance L. Depending on the orientation of J, J is added to either I_1 and subtracted from I_2, or vice versa. Without loss of generality, lets add J to I_1. Thus, the critical current $I_{0,1}$ of JJ_1 is reached for current values $I_1 < I_0$ which leads to a flux-dependent reduction of the critical current $I_c < 2I_0$ of the SQUID. J, however, can not exceed I_0. Once Φ_a reaches $\Phi_0/2$, it is energetically more favorable to increase the flux state of the SQUID by one Φ_0 and invert the direction of J [Dru16, CB04]. Thus, further increasing of Φ_a reduces J and I_c increases again. The behavior $I_c(\Phi_a)$ is described by the Langevin equations, a set of coupled differential equations. They are

obtained by inserting the 2. Josephson equation into equations (2.15) and combining them with equation (2.16). In a normalized form (all currents are normalized to $I_0 = (I_{0,1} + I_{0,2})/2$ and times to $\tau = \Phi_0/(2\pi I_0 R)$) (assuming $R_1 = R_2 = R$) it is found:

$$\frac{i}{2} + j = \sin\delta_1 + \dot{\delta_1} + \beta_c \ddot{\delta_1} \tag{2.17}$$

$$\frac{i}{2} - j = \sin\delta_2 + \dot{\delta_2} + \beta_c \ddot{\delta_2} \tag{2.18}$$

with the phase relation

$$\delta_2 - \delta_1 = 2\pi \left(\Phi_a + \frac{1}{2}\beta_L j \right). \tag{2.19}$$

Here, the screening parameter $\beta_L = 2I_0L/\Phi_0$ was introduced. It quantifies the maximum possible flux induced by the screening current $J_{\max}L = I_0L$ normalized to $\Phi_0/2$. The Langevin equations can only be solved analytically for two special cases. On the one hand, for vanishing SQUID inductances ($\beta_L \to 0$) one finds

$$I_c \approx 2I_0 \left| \cos\left(\frac{\pi\Phi_a}{\Phi_0} \right) \right|, \tag{2.20}$$

where I_c modulates from $I_c(\Phi_a = n\Phi_0) = 2I_0$ down to $I_c(\Phi_a = n\Phi_0/2) = 0$. On the other hand, for $\beta_L \gg 1$, $I_c \approx 2I_0$ with a modulation $\Delta I_c = 2I_0/\beta_L$. However, real SQUID implementations are typically somewhere in between the two special cases. In fact, Tesche et al. showed, that the optimum sensitivity is achieved for $\beta_L \approx 1$ [TC77]. Thus, to obtain the $I_c(\Phi_a)$ characteristics, numerical simulations of the Langevin equations have to be performed. Fig. 2.8 illustrates the influence of various β_L values on the $I_c(\Phi_a)$ characteristics. Figure 2.9 shows $I(V)$ characteristics of a SQUID with $\beta_L = 1$ under the influence of an applied magnetic flux Φ_a. While for $\Phi_a = n\,\Phi_0$ the maximum critical current $I_c = 2\,I_0$ is achieved, for increasing Φ_a I_c gets suppressed. For $\Phi_a = (n+0.5)\,\Phi_0$, the critical current is minimized (and in reverse J is maximized). If Φ_a is increased further, the fluxoid number is increased to $(n+1)\Phi_0$ and J changes its direction. For bias currents $I > 2\,I_0$, the influence of the supercurrents ceases and the $I(V)$ characteristics approaches the ohmic quasiparticle branch $V = IR/2$. Since I_c is flux dependent, the voltage drop across the SQUID for a given

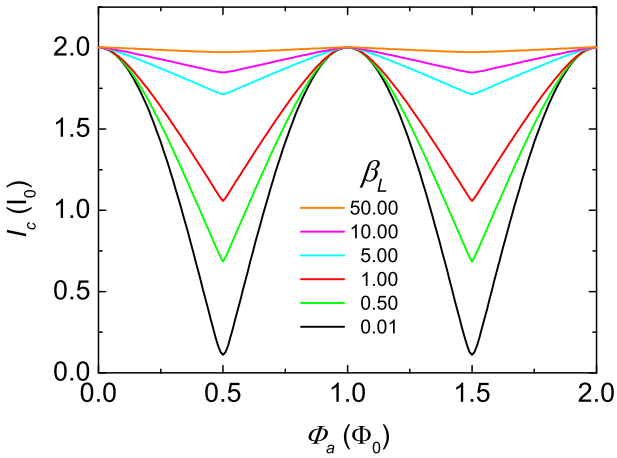

Figure 2.8.: Influence of the screening parameter β_L on the $I_c(\Phi_a)$ curve (numerical simulations).

bias current depends on Φ_a. Thus a SQUID can be used as a flux-to-voltage converter. To illustrate this behavior in more detail, Fig. 2.10(a) shows the $I(V)$ characteristics with flipped current and voltage axis while Fig. 2.10(b) shows a $V(\Phi_a)$ characteristics of a SQUID for two arbitrarily chosen bias currents $I_1 = 1.9\,I_0$ and $I_2 = 2.5\,I_0$. It can be seen, that the voltage swing caused by the change of applied flux Φ_a differs quite drastically between the two bias currents. In combination with Fig. 2.10(a), one can understand in which region of the $I(V)$ the SQUID is operated. In Fig. 2.10(b), the working points with the steepest slope $\delta V/\delta\Phi_a$ for both bias currents are indicated by green dots, respectively. It can be seen instantly, that $\delta V_2/\delta\Phi_a < \delta V_1/\delta\Phi_a$. To operate the SQUID as a flux-to-voltage converter in an ideal manner, the combination of bias current I and flux value Φ_a, which yields the largest flux-to-voltage conversion factor (the so-called transfer function)

$$V_\Phi = \left|\left(\frac{\partial V}{\partial \Phi_a}\right)\right|_{\max} \tag{2.21}$$

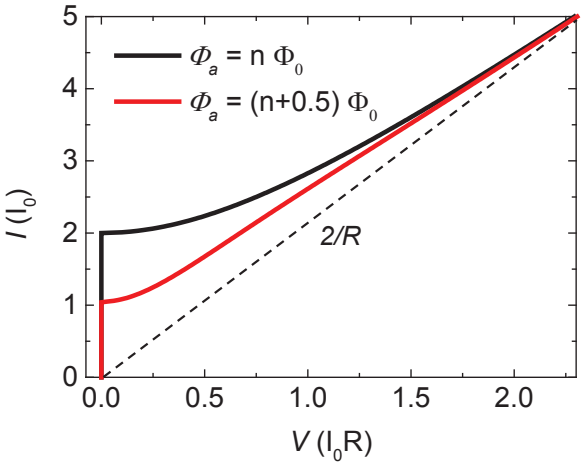

Figure 2.9.: $I(V)$ characteristics of a DC SQUID for $\Phi_a = n\,\Phi_0$ (black) and $\Phi_a = (n + 0.5)\,\Phi_0$ (numerical simulations).

is determined experimentally. For the case of $\beta_L \approx 1$, the transfer function can be approximated by

$$V_\Phi \approx \frac{\Delta V}{\frac{1}{2}\Phi_0} \approx \frac{I_0 R}{\frac{1}{2}\Phi_0} \approx \frac{R}{L}. \tag{2.22}$$

According to equation (2.22) it is advantageous to equip the JJs with large resistors R (however keep $\beta_C < 0.7$) while making the SQUID inductance L as small as possible or maximize the critical voltage $V_c = I_0 R$. A widely used, more general estimate for V_Φ (which also captures the effect of large thermal fluctuations) can be achieved by using the expression

$$V_\Phi \approx \frac{4\,I_0\,R}{\Phi_0(1+\beta_L)} \exp\left(-3.5\pi^2\,\frac{k_B T L}{\Phi_0^2}\right) \tag{2.23}$$

derived by Enpuku et al. [ESK93]. The sensitivity of a SQUID, however, is limited by the thermal noise voltage of the junction resistors. They show a frequency independent (so-called white) power spectral density $S_{\mathrm{V,R}} = 4k_B T R$. Tesche et al. showed, that this contribution is even

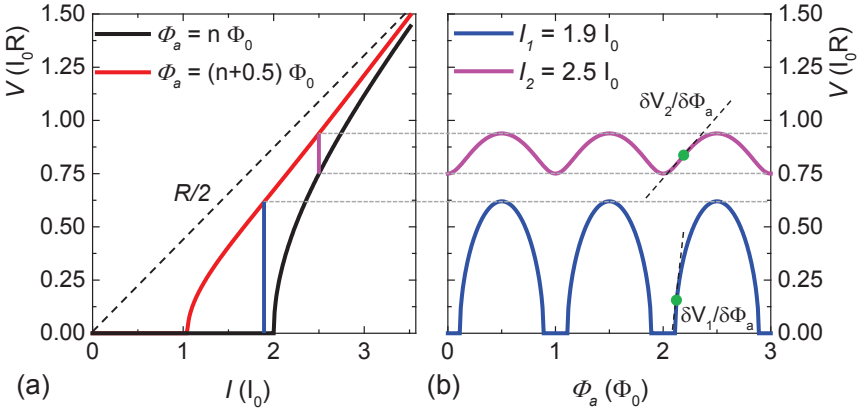

Figure 2.10.: (a) $I(V)$ characteristics with flipped current and voltage axis for $\Phi_a = n\,\Phi_0$ (black) and $\Phi_a = (n + 0.5)\,\Phi_0$ (red). The blue and the pink vertical bars illustrate the Φ_a dependent voltage swing, corresponding to the $V(\Phi_a)$ curves illustrated in (b).

increased by a factor ≈ 4 (in the limit of $\beta_L = 1$ small $\beta_C \gg 1$) due to the nonlinear behavior of the JJs, which results from downconversion effects of noise contributions of the resistor at the Josephson frequency [TC77]. A more comprehensive discussion which covers all relevant parameter limits is given in [CB04].
The power spectral density of voltage noise can be translated into an equivalent spectral density of flux noise by using the transfer functions (2.21)

$$S_\Phi^{1/2} = \frac{S_V^{1/2}}{V_\Phi} \overset{\beta_L \approx 1}{\approx} \frac{\sqrt{16 k_B T R}}{R/L} \approx \sqrt{\frac{16 k_B T L^2}{R}}. \tag{2.24}$$

In addition to the frequency independent white noise, Josephson effect based devices show an additional noise phenomena at low frequencies. In the frequency range below $f \cong 1\,\mathrm{kHz}$, so-called $1/f$ noise is present. The name originates from the shape of the spectral noise density, which scales with $1/f$. $1/f$ noise is mainly caused by two effects. First, fluctuations in the critical current density j_c, caused by temporal trapping of electrons within the barrier [CB04]. Second, thermally induced motion of superconducting vortices between defects in the superconductor (which provide

pinning centers) causes additional low frequency noise [Mar96]. If the $1/f$ noise interferes with the frequency range of interest, there are techniques to minimize its contribution, e.g. artificial pinning centers or using modulated readout techniques [CB04].

Asymmetries in DC SQUIDs

Up to now, identical electrical parameters of the JJs and a symmetrical distribution of the SQUID inductance to both arms has been assumed. However, during fabrication of the devices, variations in the JJ parameters can occur. Additionally, the systematic implementation of asymmetries can even improve the performence of a SQUID or simplify the readout by lowering the influence of preamplifier voltage noise [RNM+12, DAB+07, Dru16]. To be able to parameterize and quantify asymmetries it is useful to introduce asymmetry parameters [CB04]. Therefore, averaged values of the important parameters I_0, C, R and L are introduced:

$$\begin{aligned} I_0 &= \frac{(I_{0,1} + I_{0,2})}{2} \quad ; \quad R = \frac{2\,R_1\,R_2}{(R_1 + R_2)} \\ C &= \frac{(C_1 + C_2)}{2} \quad ; \quad L = L_1 + L_2 \ , \end{aligned} \tag{2.25}$$

where the indices $1, 2$ denote the corresponding JJ. Now it is possible to introduce an asymmetry parameter α ($\alpha \in [-1, 1]$):

$$I_{0,1} = I_0(1 - \alpha_I) \ ; \ R_1 = \frac{R}{(1 - \alpha_R)} \quad ; \ C_1 = C(1 - \alpha_C) \ ; \ L_1 = L\,\frac{(1 - \alpha_L)}{2}$$

$$I_{0,2} = I_0(1 + \alpha_I) \ ; \ R_2 = \frac{R}{(1 + \alpha_R)} \quad ; \ C_2 = C(1 + \alpha_C) \ ; \ L_2 = L\,\frac{(1 + \alpha_L)}{2} \ . \tag{2.26}$$

2.5. DC SQUID based current sensors

SQUIDs are suitable to measure any physical quantity, that can be translated into a magnetic flux Φ [CB04]. Due to their extremely high sensitivity they are predestinated for current sensing applications. There are two approaches to couple a current to the SQUID: inductively (cf. Fig. 2.11(a))

and galvanically (directly) (cf. Fig. 2.11(b)). In the inductively coupled approach the SQUID has to be equipped with an input coil which is magnetically coupled to the SQUID via the mutual inductance M_{in}. A current I_{in} flowing through the input coil will produce a magnetic field that couples flux into the SQUID. For the directly coupled SQUID-based current sensor (SCS) approach, the input inductance L_{in} is a part of the SQUID geometry itself [BRD+15]. In the optimum case, L_{in} approaches the SQUID inductance $L_{\mathrm{in}} \rightarrow L = L_1 + L_2$ which maximizes the coupling. The cou-

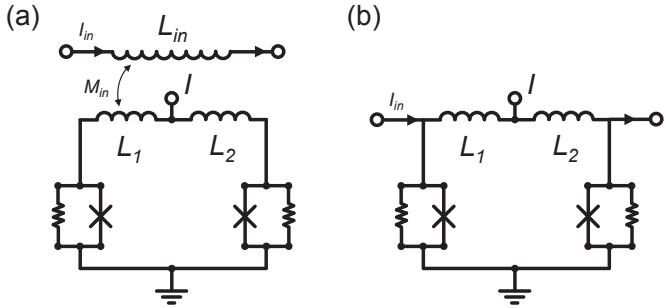

Figure 2.11.: Schematic layouts of SQUID-based current sensors. (a) An input coil with the inductance L_{in} is inductively coupled to the SQUID inductance L by the mutual inductance M_{in}. (b) shows a galvanically coupled SCS.

pling strength between the input coil L_{in} and the SQUID inductance L is quantified by the coupling factor

$$k = \frac{M_{\mathrm{in}}}{\sqrt{L_{\mathrm{in}} L}}. \tag{2.27}$$

It ranges within $k = 0..1$, where $k = 0$ represents no coupling and $k = 1$ perfectly coupled inductors. An approach of an inductively tightly coupled device was presented by Ketchen et al., where the input coil was patterned directly onto the SQUID washer [Ket87] and $k = 0.7$ was achieved. The first figure of merit of such a SCS is the input sensitivity. It is given by the inverse of the mutual inductance M_{in} and is a measure for how much current I_{in} is needed to couple one Φ_0 into the SQUID:

$$\frac{1}{M_{\mathrm{in}}} = \frac{I_{\mathrm{in}}}{\Phi_0}. \tag{2.28}$$

In combination with the equivalent flux noise density $S_\Phi^{1/2}$ of the SQUID, the second figure of merit can be derived. It is the current noise $S_I^{1/2}$ which is given by

$$S_I^{1/2} = \frac{S_\Phi^{1/2}}{M_{\text{in}}}. \tag{2.29}$$

$S_I^{1/2}$ is a measure of the minimal current that can be detected in a given SCS arrangement.

2.6. Magnetic field sensors

When the quantity of interest in an experiment is the magnetic flux density B instead of a magnetic flux Φ (as it is in NMR/MRI experiments), SCSs are often preferred over common SQUIDs. The reason for this is quite simple. The sensitivity of a SQUID for a magnetic flux density is given by $B = \Phi/A_{\text{eff}}$, where A_{eff} is the effective SQUID loop area. A larger A_{eff} allows one to resolve a smaller variation in B. However, since L of a SQUID is roughly proportional to its loop area, restrictions in the loop size arise from other parameters like β_L or the critical current density j_c. This limitation can be overcome by connecting a superconducting pickup coil with the inductance L_p and the area A_p, which senses the magnetic field and translates it into a current that is fed to the SCS (cf. Fig. 2.12). A magnetic flux density B applied to the pickup loop induces a screening

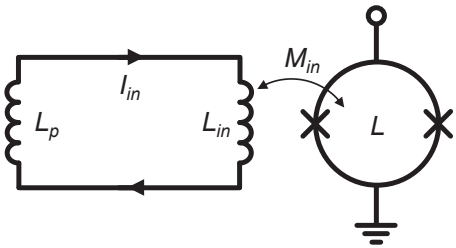

Figure 2.12.: Schematic layout of a SQUID-based current sensor equipped with an input coil with the inductance L_p.

current $I_{\text{in}} = B\,A_p/(L_p + L_{\text{in}})$. For the flux applied to the SQUID it follows

$\Phi_a = M_{\mathrm{in}} I_{\mathrm{in}} \pm B A_s$ (with A_s the effective area of the SQUID loop) and in combination with equation (2.27), the effective area

$$A_{\mathrm{eff}} = \frac{k\sqrt{L_{\mathrm{in}} L}}{L_p + L_{\mathrm{in}}} A_p \pm A_s \tag{2.30}$$

is found. In case of a magnetically shielded SQUID, this expression reduces to $A_{\mathrm{eff}} = A_p k\sqrt{L_{\mathrm{in}} L}/(L_p + L_{\mathrm{in}})$. Maximizing equation (2.30) to find the optimum ratio of L_{in}/L_p by taking the derivative $\partial A_{\mathrm{eff}}/\partial L_{\mathrm{in}}$ leads to a maximized A_{eff} for $L_{\mathrm{in}} = L_p$. Fig. 2.13 shows a plot of equation (2.30) for constant k, L and a variable ratio of L_{in}/L_p, which indicates that a small inductance mismatch L_{in}/L_p has no drastic influence on A_{eff}, e.g. $L_{\mathrm{in}}/L_p = 0.4$ still leads to $A_{\mathrm{eff}} = 0.9\, A_{\mathrm{eff,max}}$. Pickup coils are typ-

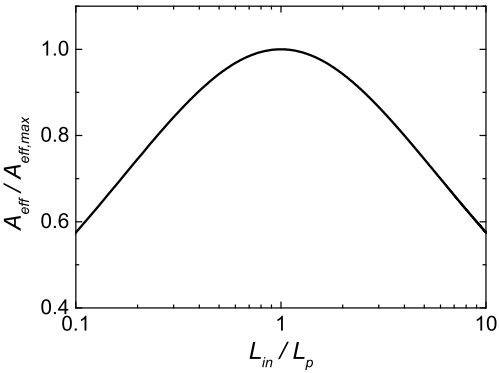

Figure 2.13.: Influence of the mismatch between the input inductance L_{in} and the pickup coil inductance L_p to A_{eff} of the SQUID based magnetic field sensor.

ically wire-wound using superconducting wire made of niobium and have inductances $L_p \approx 0.1 - 2\,\mu$H (cf. chapter 5). To achieve such a large inductance L_{in} for the input coil a large number of coil turns ($n > 50$) needs to be patterned on top of the Superconducting Quantum Interference Device (SQUID) washer [Ket87, Pol99, KJ82, JK81]. This arrangement basically forms a parasitic capacitance $C_{p,i}$ between L_{in} in the top and the SQUID washer in the bottom niobium layer which are separated by the insulating SiO_x layer [CB04]. This can lead to a parasitic tank circuit with

the resonance frequency $f_{p,i} = 1/2\pi\sqrt{L_{\mathrm{in}}C_{p,i}}$. Furthermore, the SQUID washer acts as a ground plane for L_{in}, which forms a microstrip transmission line [KAT87, KKS+88, CB04]. This can lead to microwave resonances with a high quality factor (Q factor) in the GHz range. Depending on the voltage of the SQUID's ideal working point and hence the frequency of the working point $f_{wp} = V_{wp}/\Phi_0$, the parasitic resonance frequencies may lay in the same range as f_{wp}. This interference can strongly affect the SQUID dynamics, leading to strong distortions in the characteristic curves and thus render the SQUID inoperable [HC85, KAT87, KKS+88]. An established approach to minimize the parasitic capacitance $C_{p,i}$ and keep the SQUID inductance low, yet achieving tight coupling, is to add a superconducting intermediate transformer (cf. Fig. 2.14(a)) [MJC83, DAB+07]. The

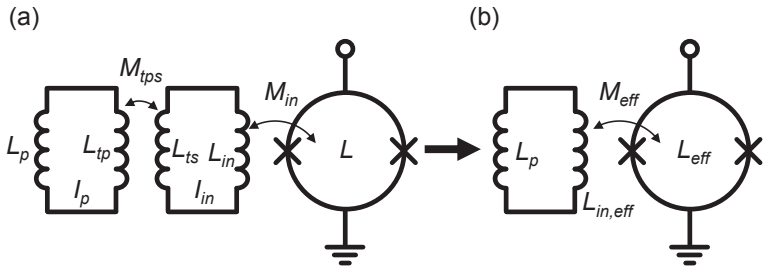

Figure 2.14.: Schematic layout of a SQUID-based current sensor equipped with an input coil with the inductance L_p and an intermediate transformer.

matching transformer is inserted between the input coil and the SQUID. By taking into account the flux conservation in the inserted superconducting flux transformer and replacing the mutual inductances by the corresponding expression for the coupling factor, one finds

$$L_{\mathrm{eff}} = L\left(1 - k_{\mathrm{in}}^2 \frac{L_{\mathrm{in}}}{L_{\mathrm{in}} + L_{\mathrm{ts}}}\right) \tag{2.31}$$

$$L_{\mathrm{in,eff}} = L_{\mathrm{tp}}\left(1 - k_{\mathrm{tps}}^2 \frac{L_{\mathrm{ts}}}{L_{\mathrm{in}} + L_{\mathrm{ts}}}\right) \tag{2.32}$$

$$M_{\mathrm{eff}} = k_{\mathrm{tps}} k_{\mathrm{in}} \frac{\sqrt{L_{\mathrm{tp}} L_{\mathrm{ts}} L_{\mathrm{in}} L}}{L_{\mathrm{in}} + L_{\mathrm{ts}}} \tag{2.33}$$

Due to the presence of the superconducting intermediate circuit, the input inductance and the SQUID inductance are reduced due to superconducting screening currents [Pol99, CB04].
An important figure of merit of a SQUID based magnetic field sensor is the spectral density of magnetic field noise

$$S_B^{1/2} = \frac{S_\Phi^{1/2}}{A_{\text{eff}}} \tag{2.34}$$

with the spectral density of equivalent flux noise $S_\Phi^{1/2}$ of the SQUID and effective area A_{eff} of the sensor arrangement.

2.7. Gradiometric pickup coils

As described in chapter 2.6, a pickup loop can increase A_{eff} of the magnetic field sensor arrangement drastically. Pickup coils are typically realized by wire-wound coils, but thin film implementations exist as well [CB04]. The most simple pickup coil approach is achieved by a single turned coil (i.e. a magnetometer). However, due to the extremely high sensitivity of the SQUID, gradiometric configurations are more feasible. They consist of at least two oppositely wound loops (indicated by the loop color in Fig. 2.15(a)). Uniform magnetic background fields or noise ideally couples equally into all loops. Thus, induced currents in the individual loops cancel out each other, resulting in an insensitivity to uniform fields and distant noise sources. Gradiometers are characterized by their loop radius r, the separation of their loops which is the so-called gradiometer baseline b, their orientation (planar or axial), their order and their balance. Fig. 2.15 shows the pickup coil configurations that are implemented for the experimental setup. Those are first- (Fig. 2.15(b)) and second-order (Fig. 2.15(c)) axial gradiometers. The order of the gradiometer denominates the magnetic field derivative, to which the configuration is susceptible. Higher order gradiometers can be built by combining lower order gradiometers, for instance a second-order gradiometer is yielded by combining two first-order gradiometers (cf. Fig. 2.15(c)). While first-order gradiometers are susceptible to field changes along its axis, e.g. along the z-axis $\partial B_z/\partial z \approx \Delta B_z/b$, second-order gradiometers are susceptible to the second derivative of the field $\partial^2 B_z/\partial z^2 \approx \Delta B_z^2/b^2$ and so on. The sample in a NMR experiment

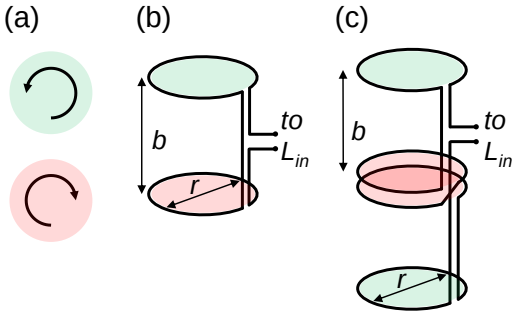

Figure 2.15.: Schematic illustration of axial gradiometric pickup coils. (a) illustrates the opposite winding orientations. (b) Layout of a first-order gradiometer. (c) Layout of second-order gradiometer composed of two first-order gradiometers.

produces a dipole magnetic field, that decays $\propto 1/|\vec{r}|^3$ where $\vec{r}$ is the distance between the dipole and the point of interest. Since the sample is placed closely to the lowest loop of the gradiometer, for the distance d between sample and loop this yields the condition $d < b$. Therefore, as a first approximation the signal originating from the sample only penetrates the lowest loop.
The balance (also known as the common mode rejection ratio (CMRR)) for a uniformly applied magnetic flux density B, is given by the ratio

$$\text{CMRR} = \frac{\text{signal of a magnetometer}}{\text{signal of the gradiometer}}, \tag{2.35}$$

where a magnetometer is a single loop pickup coil. Hand made wire wound gradiometers typically achieve CMRR $\approx$ 100 − 1000 [BK13, KEMV14, CB04].

2.8. Determination of L_{in} of a SQUID-based current sensor

To determine the input inductance of a SCS, the input coil is shorted using a small resistor R_{short} (with the inductance L_{short}), which forms a LR low-pass filter [Rue08]. Subsequently, a voltage noise spectrum is recorded using

a flux locked loop (FLL) circuit (cf. appendix A). Due to the low-pass filter behavior, the spectrum exhibits a cut-off frequency $f_{-3\mathrm{dB}}$. By evaluating $f_{-3\mathrm{dB}}$, the input inductance can be calculated using the expression

$$L_{in} = \frac{R_{\mathrm{short}}}{2\pi\, f_{-3\mathrm{dB}}} - L_{\mathrm{short}}. \tag{2.36}$$

R_{short} is realized by an aluminium bond wire, which typically has a resistance of $R_{\mathrm{short}} = 5 - 25\,\mathrm{m\Omega}$. L_{short} was generously estimated and typically set to $L_{\mathrm{short}} = 10\,\mathrm{nH}$. The resulting values for L_{in} are consistently $10-15\,\%$ smaller than the expected values simulated using 3D-MLSI (cf. chapter 3.4) due to the screening currents of the SQUID. As has been shown above (cf. fig 2.13), a small deviation from the design value has no big influence on the sensor performance. Consequently, L_{in} was not determined for every SQUID but rather rarely since the determination requires a separate cool down.

2.9. Principles of nuclear magnetic resonance

Nuclear magnetic resonance (NMR) experiments study the time evolution of the magnetization of a sample originating from its nuclear spin $\vec{I}$ which can be manipulated by means of externally applied magnetic fields.

2.9.1. The origin of the sample magnetization

Elements having a nuclear spin $\vec{I} \neq 0$ in their ground state exhibit a nuclear magnetic moment μ_I given by $\mu_I = \gamma \vec{I}$. Here, γ is the element specific gyromagnetic ratio. In an applied magnetic field $\vec{B}_0$, which is without loss of generality assumed to be oriented in the z direction, the potential energy of the nuclei $E_{m_I} = -\mu_I |\vec{B}_0| = -\gamma \hbar m_I |\vec{B}_0|$. Here, $m_I = -I, -I + 1, ..., I - 1, I$ is the projection of $\vec{I}$ along the z axis. For $\vec{B}_0 = 0$, the levels are degenerated. Since for $\vec{B}_0 = 0$ there is no preferred energy level, the nuclear spins are aligned randomly, yielding a net magnetization along the z axis $\vec{M}_0 = 0$. As soon as $\vec{B}_0 \neq 0$, the potential energy for all possible projections m_I is no longer degenerated, but Zeeman splitting into $2I + 1$ levels occurs. The energy splitting between two levels $m_{I,n}$ and $m_{I,m}$ is given by $\Delta E = (m_{I,m} - m_{I,n})\, \gamma \hbar |\vec{B}_0|$. For the most commonly used element ^{1}H with the nuclear spin $I = 1/2$, this leads to two possible levels with $m_I = \pm 1/2$. These two levels are split by the energy $\Delta E = \hbar \omega_0$, where

$$\omega_L(\vec{B}_0) \equiv \omega_0 = \gamma |\vec{B}_0| \tag{2.37}$$

is the Larmor frequency referred to a specific magnetic field $\vec{B}_0$.
In thermal equilibrium the distribution of the population of these energy levels is governed by a Boltzmann distribution

$$P_{m_I} = \frac{N}{Z} e^{-\frac{E_{m_I}}{k_B T}} = \frac{N}{Z} e^{-\frac{-\gamma \hbar m_I |\vec{B}_0|}{k_B T}} \tag{2.38}$$

with the number of spins N and $Z = \sum_{m_I} e^{-\frac{E_{m_I}}{k_B T}}$ being a normalization factor. For the thermal equilibrium magnetization of the sample in the limit of small magnetic fields and high temperatures (around room temperature)

the exponent of the Boltzmann distribution $\frac{\gamma\hbar m_I|\vec{B}_0|}{k_B T} \ll 1$, which leads to Curie's law [BCH+14]

$$|\vec{M}_0| = \frac{N\, I(I+1)\gamma^2\hbar^2}{3k_B T}|\vec{B}_0| \overset{I=1/2}{=} \frac{N\,\gamma^2\hbar^2}{4k_B T}|\vec{B}_0|. \tag{2.39}$$

The resulting magnetization $\vec{M}_0$ is created by the number of excess spins ΔN occupying the energetically lower state where the spins are aligned parallel to $\vec{B}_0$. Their number is approximately given by

$$\Delta N = N\frac{\gamma\hbar}{k_B T}|\vec{B}_0|. \tag{2.40}$$

$\Delta N/N$ is an extremely small number even for relatively strong magnetic fields. For example, for $|\vec{B}_0| = 1\,\mathrm{T}$ at $T = 300\,\mathrm{K}$ one obtains $\Delta N/N = 6.8{\cdot}10^{-6}$. The reason for NMR being a macroscopically observable effect for structure analysis in chemistry and for noninvasive examination methods like magnetic resonance imaging (MRI) is the huge amount of nuclei of approx. $10^{23}\,\mathrm{cm}^{-3}$ [HSL+13].

2.9.2. Manipulation of $\vec{M}_0$

As has been shown in chapter 2.9.1, for ^{1}H in a magnetic field $\vec{B}_0$ two energy levels exist. The dynamics of such a two-level system can be mapped onto the Bloch sphere where the state vector is given by the sample magnetization vector $\vec{M}$ [BCH+14]. Excitations from the energetically lower to the higher state can be achieved by irradiating the sample with a RF magnetic field perpendicular to $\vec{B}_0$ at the Larmor frequency $\omega_0 = |\gamma||\vec{B}_0|$ with the amplitude $|\vec{B}_1|$. This offers a tool to change the level population and thus the magnetization along the z axis $\vec{M} = |\vec{M}_0|\hat{e}_z$ can be manipulated. Within the framework of the Bloch sphere, the manipulation of $\vec{M}_0$ can be understood as a rotation of $\vec{M}$ along the angle Θ (cf. Fig. 2.16). For an RF magnetic field with the amplitude $|\vec{B}_1|$ applied along the x axis for the time $t_{\vec{B}_1}$, the rotation angle Θ of $\vec{M}$ can be calculated as

$$\Theta = \gamma \int_{t_{B1}} |\vec{B}_1| dt. \tag{2.41}$$

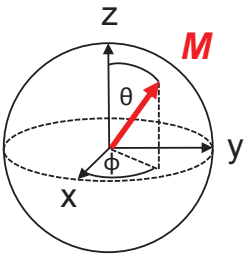

Figure 2.16.: Illustration of the magnetization vector $\vec{M}$ in the framework of the Bloch sphere.

The dynamics of the magnetization vector is governed by the Bloch equation

$$\frac{d\vec{M}(t)}{dt} = \gamma \vec{M}(t) \times \vec{B}(t) \tag{2.42}$$

In case of $\Theta \neq 0°$ and a magnetic field $\vec{B}_0$ parallel to the z axis, $\vec{M}$ experiences a torque in the $x-y$ plane which leads to a precession of $\vec{M}$ about $\vec{B}_0$ with the frequency ω_0 [BCH+14].

2.9.3. Relaxation

To manipulate $\vec{M}$ out of its thermal equilibrium magnetization $\vec{M}_0$ along the z axis, energy is pumped into the system via a $\vec{B}_1$ pulse. After switching off $\vec{B}_1$, the system will relax back into the thermal equilibrium magnetization. This relaxation process is governed by two different processes. The first process is known as spin-lattice relaxation and describes the relaxation of the longitudinal component $M_z(t)$ (parallel to the z axis) of the magnetization $\vec{M}_0$. Before an excitation pulse is applied, the longitudinal magnetization $M_z(t)$ is given by $M_z(t) = \vec{M}_0$. After an excitation pulse $M_z(t) < |\vec{M}_0|$, and the excited spins will start to dissipate the excess energy $\hbar\omega_0$ into the surrounding atomic structure (lattice) to approach the energetically lower thermal equilibrium state [BCH+14]. The behavior of $M_z(t)$ is described by

$$M_z(t) = |\vec{M}_0| - (|\vec{M}_0| - M_z(0))\, e^{-t/T_1} \tag{2.43}$$

where T_1 is the spin-lattice relaxation time.
The second relaxation process is known as spin-spin relaxation, and it affects the transversal magnetization $M_t(t)$. As the magnetization is tipped into the $x-y$ plane, it starts to precess about $\vec{B}_0$. Random spatial motion of nuclei due to diffusion processes and the interaction of neighboring spins alter the local field strength of $\vec{B}_0$ to $|\vec{B}_0| \pm |\delta\vec{B}|$ on a microscopic scale. This slight deviation from $\vec{B}_0$ induces position dependent Larmor frequencies $\omega_0(\vec{r})$ which leads to some spins either precessing with a slightly higher Larmor frequency $\omega_0 + \delta\omega$ or a slightly decreased frequency $\omega_0 - \delta\omega$. This effectively leads to a rapid dephasing of the individual spins from the initially induced coherent spin ensemble and $M_t(t)$ vanishes. Intrinsic inhomogeneities of the $\vec{B}_0$ magnetic field accelerate the dephasing process. The transversal magnetization $M_t(t)$ is governed by

$$M_t(t) = M_t(0)\, e^{-t/T_2^*} \tag{2.44}$$

where T_2^* is the effective spin-spin relaxation time. T_2^* contains both the contributions of the spin-spin interaction as well as $\vec{B}_0$ inhomogeneities:

$$\frac{1}{T_2^*} = \frac{1}{T_2} + \gamma\delta B \tag{2.45}$$

The time constant caused by the spin-spin interaction T_2 is typically larger than T_2^*. The relaxation time T_2 can be determined by a multi-spin echo sequence (cf. chapter 2.9.5). The resulting Bloch equations including the relaxation time constants are given by

$$\frac{\mathrm{d}M_x}{\mathrm{dt}} = \gamma\left(\vec{M}(t)\times\vec{B}(t)\right)_x - \frac{1}{T_2}M_x \tag{2.46}$$

$$\frac{\mathrm{d}M_y}{\mathrm{dt}} = \gamma\left(\vec{M}(t)\times\vec{B}(t)\right)_y - \frac{1}{T_2}M_y \tag{2.47}$$

$$\frac{\mathrm{d}M_z}{\mathrm{dt}} = \gamma\left(\vec{M}(t)\times\vec{B}(t)\right)_z - \frac{1}{T_1}(M_z - |\vec{M}_0|) \tag{2.48}$$

$$\tag{2.49}$$

2.9.4. FID sequence

The most simple way to acquire spectroscopic information on a sample is by performing a so-called free induction decay (FID) sequence. Fig. 2.17 illustrates both the time evolution of the pulse sequence (top) as well as the behavior of the magnetization vector $\vec{M}$ in the framework of the Bloch sphere (bottom). The NMR-sample is placed into a static magnetic field $\vec{B}_0$ that defines the Larmor frequency ω_0. After the sample was exposed to $\vec{B}_0$ for a time $t > T_1$, such that the thermal equilibrium magnetization has been built up (cf. Fig. 2.17 **I**), a 90° pulse is applied to the sample in x direction that rotates the magnetization vector into the $x - y$ plane of the Bloch sphere (**II**).

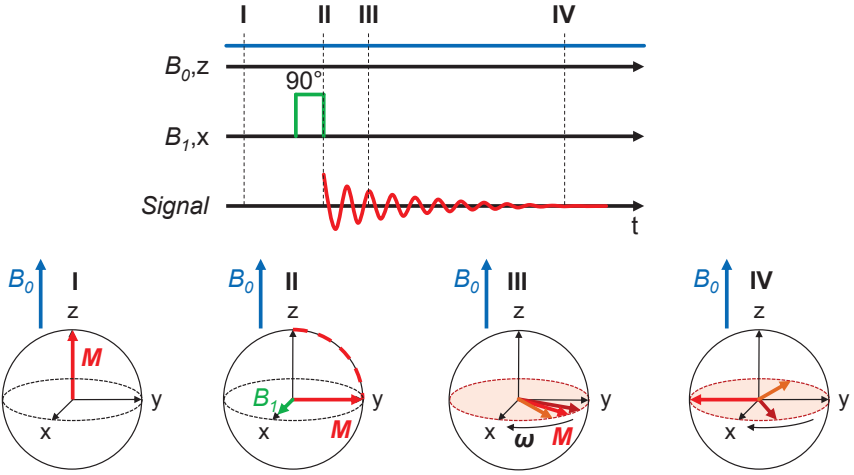

Figure 2.17.: Illustration of a FID sequence. The upper part shows the timing and the pulses of the sequence, while the lower part demonstrates schematically the spin dynamics of the sequence.

Now, $\vec{M}$ experiences a torque in the $x - y$ plane and it starts to rotate about $\vec{B}_0$. A detector that is sensitive to the magnetic field directly (or magnetic field changes) in the $x - y$ plane now can acquire a signal at the frequency ω_0. Due to the spin-spin relaxation explained above, the spins responsible for $\vec{M}$ start to dephase (cf. **III**, indicated by the differently

colored arrows). After letting the system evolve in time, the dephasing increases and the detectable transversal magnetization vanishes (cf. **IV**). The envelope function of the acquired time trace is given by the exponential decay according to equation (2.44) with the effective spin-spin relaxation time T_2^*. The time trace can be transformed into the frequency domain to investigate the frequency characteristics by means of a fast Fourier transform (FFT).

2.9.5. Spin echo sequence

The spin echo sequence employs two tipping pulses and is schematically illustrated in Fig. 2.18. The magnetization vector is tipped into the $x-y$ plane by a 90° $\vec{B}_1$ pulse in the x direction. Now it starts to perform a FID and spin-spin relaxation causes a dephasing of the spins (cf. 2.17 **III**) due to local deviations $\pm\delta\omega$ from ω_0.

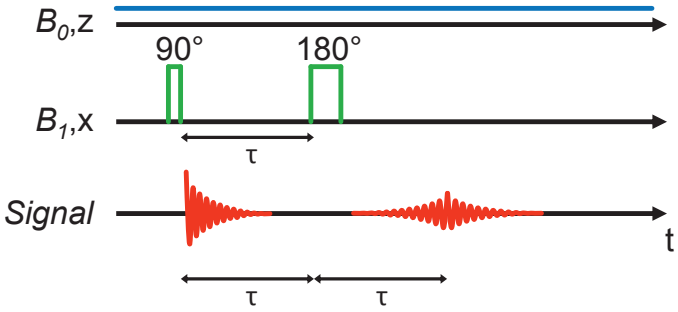

Figure 2.18.: Timing diagram of a spin echo sequence.

By applying a 180° $\vec{B}_1$ pulse in the x direction after the time τ, the magnetization vector gets flipped within the $x-y$ plane which effectively inverts the phase relation of the dephasing spins. Thus, as time evolves, the spins start to refocus. After waiting for $t=\tau$ after the second pulse, all spins are refocused and the spin echo can be observed at the echo time $t_E = 2\tau$. By applying a 180° pulse every t_E, a multi-spin echo sequence is formed. Due to the reappearing spin phase inversions, stationary local $\vec{B}_0$ inhomogeneities are effectively canceled out. Therefore, by investigating the time evolution of the area under peak for each spin echo signal, the

envelope function decays exponentially with the time constant T_2, turning the multi spin echo sequence into a tool for directly measuring the T_2 time constant.

2.10. Ultra-low field NMR

Conventional NMR or MRI applications are striving for higher and higher $\vec{B}_0$ fields [BCH+14]. The reason for this endeavor becomes quite obvious when inspecting Curie's law (2.39) and the Larmor frequency (2.37) and taking into account that the signal acquisition is done by normal conducting coils.

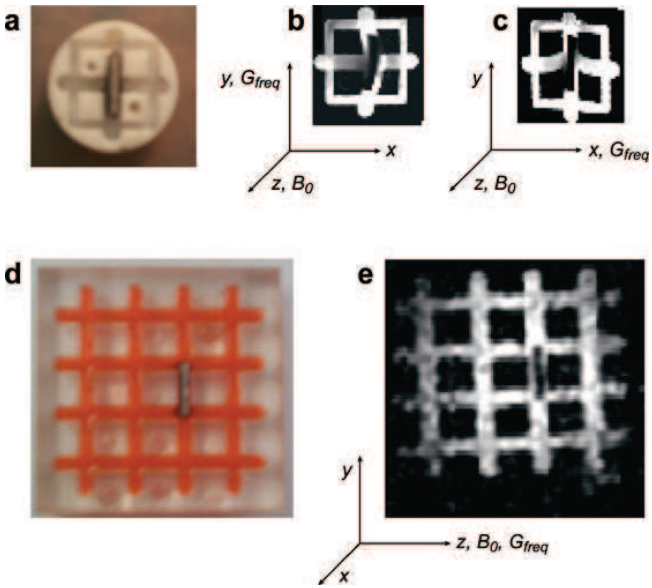

Figure 2.19.: Distortion effect caused by the susceptibility differences between water and a titanium rod in a MRI phantom (a) at $|\vec{B}_0| = 7\,\mathrm{T}$ (b,c). (d) shows a different MRI phantom using the same titanium rod at $|\vec{B}_0| = 66\,\mu\mathrm{T}$ (e), where almost no artifacts can be observed. Figure taken from [CHM07].

Since the magnetization of the sample $M \propto |\vec{B}_0|$ and the voltage output of a coil according to Faraday's law $V \propto dM/dt \propto \omega_0 \propto |\vec{B}_0|$, the

NMR signals scales $\propto |\vec{B}_0|^2$ and is additionally part of a tank circuit tuned to one specific Larmor frequency. This approach is highly successful in medical imaging, where typically MRI scanners with $|\vec{B}_0| = 1.5\,\mathrm{T}$ are employed, however also scanners with higher fields of $3 - 9\,\mathrm{T}$ are found in fundamental research. Although such high magnetic fields can also be produced by normal conducting coils, practical coil implementations with bore diameters large enough for investigating human beings are realized using persistent mode superconducting $\vec{B}_0$ coils. As a result, high field scanners are extraordinarily expensive and become quite bulky and immobile. Also, imaging in the vicinity of metals (e.g. implants) is not possible without any problems. Susceptibility differences between the metal and the surrounding tissue cause local field inhomogeneities $\propto \vec{B}_0$ which reduces T_2^*. In the best case, these artifacts are rendering the image unusable (cf. Fig. 2.19(a),(b) and (c)) whereas they also can be confused with a pathology and lead to a false indication [KBF15]. This effect, however, can be neglected at low $\vec{B}_0$ fields (cf. Fig. 2.19(d) and (e)) [MHM$^+$06, CHM07]. Additionally, eddy currents induced in metal parts by the $\vec{B}_1$ pulse distort the phase and amplitude relation of the nearby area. This effect also vanishes for low $\vec{B}_0$ fields since the skin depth δ scales as $\delta \propto 1/\sqrt{f_0}$ [CHM07]. At high fields, this becomes not only a problem for metal parts but also for skin tissue. High field scanners require $\vec{B}_1$ pulses in the range of a few hundreds of MHz which therefore have to be high-powered to penetrate the body. As a result, it must be ensured that the specific absorption rate (SAR) levels are on a tolerable level at any time. This becomes more and more complicated when going to higher $\vec{B}_0$ fields since on the one hand $\vec{B}_1$ frequencies deposit more energy. On the other hand the wavelength λ of the RF irradiation becomes comparable to the size of a human. Therefore, there can be field nodes within the body where no spin excitation is possible while at field antinodes the deposited energy can be intolerably high [PSS16].
Many of the mentioned problems are not present when going to low $\vec{B}_0$ fields. Susceptibility-difference induced artifacts practically vanish and SAR levels become uncritical [KEMV14]. The most striking advantage is, however, that no superconducting coils are needed to produce $\vec{B}_0$, it can be done by conventional copper coils. This allows for the design of open and easily accessible coil setups, and also mobile setups could be realized. Handling in the vicinity of the magnet becomes safe because the field can simply be turned off. However there are also drawbacks. Since

the sample polarization is $\propto |\vec{B}_0|$ the resulting magnetization gets reduced drastically. Since the signal output of coils $V \propto dM/dt \propto \omega_0 \propto |\vec{B}_0|$, the coil effectively acts as a high pass filter. Additionally the intrinsic current and voltage noise becomes a limiting factor [Mye06].
Employing an untuned SQUID as detector becomes advantageous for low frequency NMR applications. The detected signal no longer scales $\propto |\vec{B}_0|^2$ but only $\propto |\vec{B}_0|$ since the SQUID detects the magnetization directly and not its time derivative. The very high, frequency independent intrinsic sensitivity of a SQUID sensor (except for the $1/f$ region) becomes superior to that of a copper wound coil below $\approx 25\,\mathrm{mT}$ (cf. Fig. 2.20). Additionally, the frequency independent high sensitivity (in the white region) allows a flexible choice of $\vec{B}_0$ and thus ω_0 since the detector no longer needs to be part of a tuned tank circuit. Another advantage of a untuned sensor approach is, that it allows for the detection of NMR signals of various nuclei at the same time.

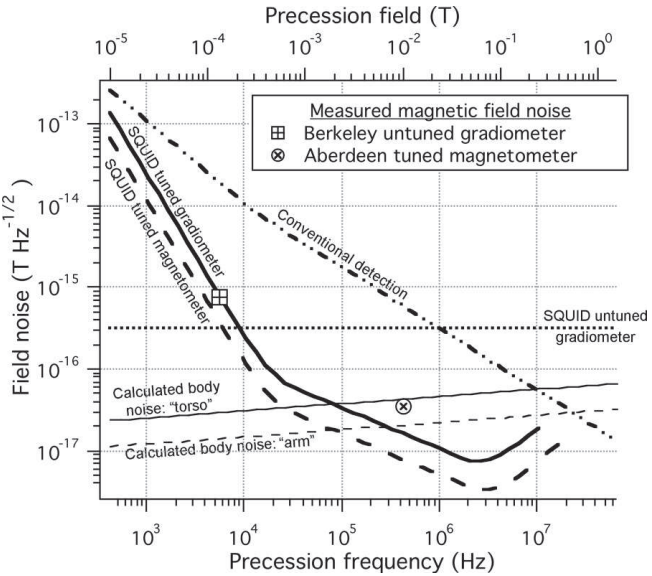

Figure 2.20.: Frequency dependent noise contributions of various different detection schemes. Taken from [Mye06].

2.10.1. Prepolarization

As described earlier, when dealing with NMR measurements in low and ultra-low field regimes (ULF regime: $|\vec{B}_0| < 10\,\mathrm{mT}$), the resulting sample magnetization is quite low (cf. equation 2.39) [KEMV14]. A simple yet effective way to increase the magnetization and thus the resulting signal is achieved by prepolarizing the sample using a magnetic field $|\vec{B}_P| \gg |\vec{B}_0|$ with a separate prepolarization coil. $\vec{B}_P$ is aligned perpendicular to $\vec{B}_0$ to minimize the mutual inductive coupling between the two coils that would limit the ramping-down time of the $\vec{B}_P$ field. $\vec{B}_0$ is still present during prepolarization, however since $|\vec{B}_P| \gg |\vec{B}_0|$, the resulting magnetization is practically unaffected by $\vec{B}_0$. This results in a magnetization increase of $\approx |\vec{B}_P|/|\vec{B}_0|$. Once the sample was prepolarized for a time larger than T_1, $\vec{B}_P$ gets turned off adiabatically (turnoff time typically $1 - 1.5\,\mathrm{ms}$) [KEMV14]. The magnetization vector follows the resulting field vector adiabatically, eventually making a transition back parallel to $\vec{B}_0$. The magnetization, however, starts to decay back to the level achieved by using $\vec{B}_0$ only. Therefore, the time between turning off the prepolarization coil and starting the measurement should be kept as short as possible.

2.10.2. T_1 determination using $\vec{B}_P$

A very elegant method to determine the spin-lattice relaxation time constant T_1 at ULF conditions makes use of the prepolarization field $\vec{B}_P$. After waiting for the time τ_d once the $\vec{B}_P$ pulse was turned off, a 90° $\vec{B}_1$ pulse is applied which flips the rebuilt magnetization vector into the $x - y$ plane and a FID can be observed. By varying τ_d and plotting the FID peak height versus τ_d, T_1 can be extracted. Additionally, a common inversion recovery (IR) sequence, which is commonly used in high field applications, can be employed [BCH+14].

2.11. Hyperpolarization

Hyperpolarization is the term used for nuclear spin polarizations that are increased drastically compared to the thermal equilibrium polarization. This is achieved by increasing the population of the lower energy eigenstate which results in a increased sample magnetization. This behavior is schematically illustrated in Fig. 2.21 [MS11]. Various tech-

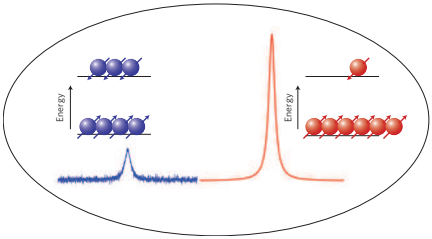

Figure 2.21.: Schematic illustration of the spin population in a hyperpolarized sample. Figure taken from [MS11].

niques to achieve hyperpolarization are reported in literature like spin exchange optical pumping of ^{3}He, ^{83}Kr and ^{129}Xe [ALFG^{+}03], metastability exchange optical pumping of ^{3}He [SCO^{+}05], dynamic nuclear polarization of ^{13}C, ^{15}N, ^{19}F or ^{31}P using the nuclear Overhauser effect [ZOM^{+}10] or parahydrogen induced polarization. This work only examines parahydrogen induced polarization (PHIP), especially the hyperpolarization scheme called signal amplification by reversible exchange (SABRE) [AAA^{+}09, HSL^{+}13, HKS^{+}14].

2.12. Signal amplification by reversible exchange

The SABRE hyperpolarization scheme was first suggested in 2009 by Adams et al. [AAA^{+}09]. The huge advantage of SABRE as compared to other PHIP schemes is that it leaves the spin-enhanced substance chemically changed (i.e. hydratized). It relies on pH_2 as a spin order supplier. A hydrogen molecule, which consists of two hydrogen atoms H_a and H_b, exists in two spin isomers. Orthohydrogen (oH_2) is the triplet spin state, where both nuclear spins are aligned parallel. oH_2 has a total nuclear spin $I = 1$. pH_2 is the singlet state spin isomer, where the two nuclear spins are aligned anti-parallel, yielding a NMR blind molecule with $I = 0$. In addition to pH_2, SABRE involves a transition metal (commonly iridium) based complex molecule with a ligand (IMes) acting as an electron donor, a target molecule that receives the spin order (e.g. pyridine) and a solvent to create a liquid solution. It takes place in magnetic fields $|\vec{B}_0|$ in the $2 - 10\,\mathrm{mT}$ range [HSL^{+}13, AAA^{+}09].

Schematically, the process of the magnetization transfer of SABRE is illustrated in Fig. 2.22. The initial condition is shown in Fig. 2.22 ***I***, where

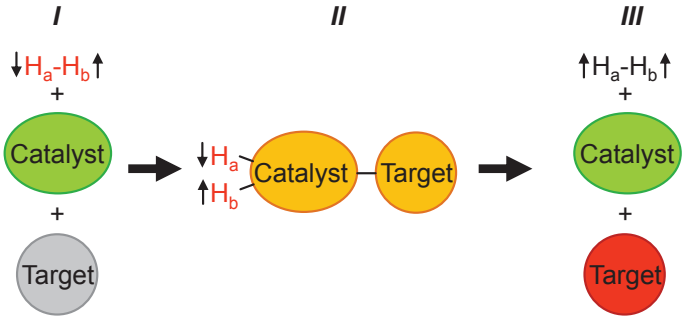

Figure 2.22.: Schematic illustration of the magnetization transfer process of SABRE.

the three involved components of the process are still separated. The unhyperpolarized target is indicated by the grey color. Two individual, transient processes will take place. First, the pH_2 can come into contact with the catalyst. In this case, the covalent bond of the pH_2-molecule is broken and both ^1H atoms bind to the metal center of the catalyst, forming two hydrides. This is a reversible reaction, i.e. the two hydrides can detach themselves from the metal center and reform to a oH_2 molecule [Hig13]. The second process that takes place involves the catalyst and the target. Target molecules bind to the metal center as ligands, interact with the catalyst for the time t_i and detach them self again. Both processes happen constantly. During the time both processes take place, the structure of the catalyst molecule is schematically illustrated in Fig. 2.23. Both hydride ligands on the catalyst and the nuclei on the target intended for hyperpolarization form a scalar coupled (J-coupling) network, i.e. two nuclear spins are coupled via electrons of chemical bonds (cf. 2.22 ***II***, coupling is indicated by the orange color of the resulting complex molecule) [LAB+14]. Thus, the purpose of the catalyst is to supply the chemical bonds that are used subsequently to mediate the nuclear spin coupling. After the spin order has been transferred and both the hydrogen atoms and the target have been detached from the catalyst, eventually an unmodified catalyst, a hyperpolarized target molecule (indicated by the red color) and a oH_2

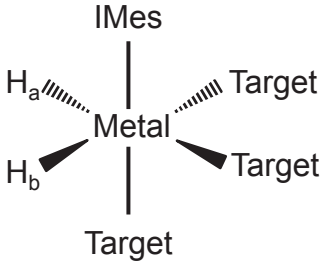

Figure 2.23.: Schematic illustration of the catalyst molecule during both reactions

molecule remain (cf. Fig. 2.22 ***III***). Since both processes repeat constantly, after depleting the hyperpolarization by means of a 90° excitation pulse, hyperpolarization on target molecules will be built up again immediately as long as long as pH_2 is supplied.
The theoretical description of SABRE and all relevant mechanisms involved are not understood completely. The following description is meant to give a brief introduction, detailed descriptions can be found in the literature [HKS+14, BFSM12, PYV+13, PIY+15]. SABRE employs level anti-crossing (LAC) between $\vec{B}_0$ independent J-coupling energy levels of both the $H_a + H_b$ pair (cf. A,A' in Fig. 2.24) as well as protons from the target molecule M + M' (cf. M,M' in Fig. 2.24) and the $\vec{B}_0$ dependent chemical shift of those two coupled spin systems. Such a system forms a so-called AA'MM' spin network [MMR55] For two given quantum states

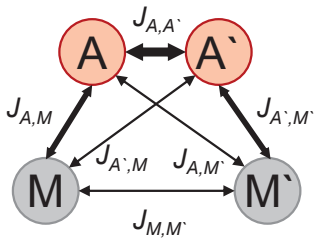

Figure 2.24.: Coupling network of a so-called AA'MM' spin network responsible for the polarization transfer [BFSM12, PYV+13].

$|m\rangle$ and $|n\rangle$, LAC occurs at magnetic field values where the energy levels of the two states would cross if there would be no coupling present between $|m\rangle$ and $|n\rangle$. At the LAC point, the system eigenstate is given by the product state $|m\rangle \otimes |n\rangle$ and a population exchange of $|m\rangle$ and $|n\rangle$ can occur. With respect to the SABRE framework, we can observe mixing between the states $|S, K\rangle$ and $|T_k, L\rangle$. S and T_k denote the singlet and triplet (T_+, T_0, T_-) of the pH_2 protons H_a and H_b while $|K\rangle$ and $|L\rangle$ describes the states of target molecule protons [PYV+13]. Since we supply H_a and H_b in the singlet state mixing the states will lead to transitions between $|K\rangle$ and $|L\rangle$. Spin polarization will be achieved by depleting the $|K\rangle$ and enriching the $|S, K\rangle$ and $|T_k, L\rangle$ state.

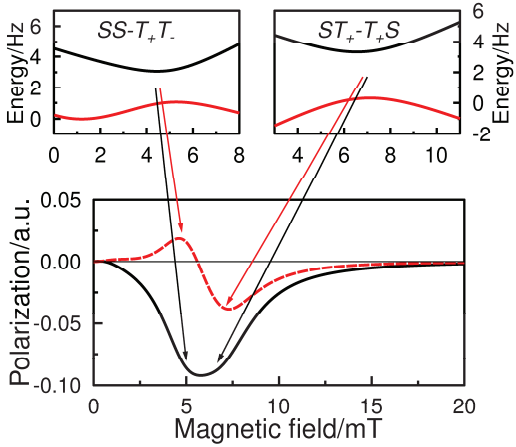

Figure 2.25.: Energy level scheme of SABRE applied to an AA'MM' spin network. Anti-crossing levels (top) and calculated field dependence (bottom). The solid line represents the net polarization ($I_{M_z} + I_{M'_z}$) while the dashed line shows multiplet polarization $I_{M_z} I_{M'_z}$. Calculation parameters: $(\omega_A - \omega_M) = -31$ ppm, $J_{AA'} = -7$ Hz, $J_{AM} = J_{A'M'} = 3$ Hz, $J_{A'M} = J_{AM'} = 0$ Hz, $J_{MM'} = 2$ Hz. The arrows assign LACs to features in the field dependence. Taken from [PYV+13].

The described model can now be applied to the AA'MM' spin network formed by former pH_2 protons and protons of the target molecule. Both sets of protons experience the same chemical shift $\delta_A = \delta_{A'}$ and $\delta_M = \delta_{M'}$

due to the fact that they are chemically equivalent. Due to the existing Cs symmetry of the system, it can be assumed that $J_{AM} = J_{A'M'}$ and $J_{A'M} = J_{AM'}$ respectively. LAC occurs at magnetic fields where the following energy matching conditions are fulfilled (cf. Fig. 2.25):

$$|ST_{\pm}\rangle \leftrightarrow |T_{\pm}S\rangle : \pm(\omega_A - \omega_M) = J_{AA'} - J_{MM'} \quad (2.50)$$

$$|SS\rangle \leftrightarrow |T_{\pm}T_{\mp}\rangle : \pm(\omega_A - \omega_M) = J_{AA'} - J_{MM'} - \frac{1}{2}(J_{AM} - J_{AM'}) \quad (2.51)$$

where ω_A and ω_M are the Larmor frequencies between AA' and MM' protons for a given $\vec{B}_0$ field.

3 Current sensor design and fabrication

This chapter will start with a detailed description of the fabrication process of superconductor-insulator-superconductor (SIS) based JJs. For this purpose, the fabrication procedures of the Physikalisch-Technische Bundesanstalt (PTB) in Braunschweig, which have been used for the sensors, are explained. Subsequently, required functional blocks that ensure an undisturbed operation of SQUID based current sensors, e.g. on-chip RF filter, will be worked out.

3.1. Sensor fabrication

Most of the SQUIDs have been fabricated in a SIS process based on Nb/Al-AlO_x/Nb trilayer junctions. The devices have been fabricated in the clean room center of the PTB in Braunschweig under the direction of O. Kieler. It is a fully equipped research facility specialized on high quality thin film production, metrology and superconducting devices. For the deposition and patterning of thin film structures, various technologies are available [DSZN05, Kie17, KMD+14].
The most superior feature of the fabrication capabilities of the PTB is the fact, that the pattern definition of parameter sensitive device structures is done completely using non-contact electron beam lithography (EBL). Commonly, superconducting devices like SQUIDs are fabricated using standard photolithographic processes. Here, the device structures are transferred from a photomask (which is in physical contact with the wafer) into a light-sensitive chemical (i.e. photoresist) by illuminating the complete

photomask with ultraviolet (UV) light. This limits the reproducibility and reliability of the fabrication of device structures to a feature size of commonly $1.5 - 3.5\,\mu$m [DAB$^+$05, Mec13, Sta17b]. EBL, in contrast, uses a tightly focused electron beam (minimum beam diameter $\approx 10\,$nm) to scan across the wafer and directly write structure patterns into an electron sensitive photoresist. This way, in an superconductor-normal conductor-superconductor (SNS) process the reliable fabrication of DC SQUIDs with JJ sizes down to 150 nm [MPGM$^+$16, BWW$^+$15, NBX$^+$13] or the fabrication of series arrays with up to 200, 000 working JJs has been demonstrated [Kie17, KKM07, KMK$^+$07]. Additionally no photomask is needed, which establishes EBL as a quite flexible patterning technique. A huge advantage of sub-μm sized JJs, compared to μm sized JJ, is the decreased JJ capacitance C_{JJ} which scales with the JJ area. Hence, the damping parameter $\beta_C \propto I_0 R^2 C_{JJ}$ is directly affected. For instance, if sub-μm sized JJs are employed for devices with a given β_C (I_0 usually is fixed due to a required/constricted β_L), the junction capacitance C_{JJ} is drastically reduced compared to μm sized JJs. Therefore the shunt resistor R can be increased while β_C can be kept the same. An increased shunt resistor R leads to a larger critical voltage $V_c = I_c \cdot R/2$ and thus to an increased transfer function V_Φ due to the larger V_c, respectively. In consequence, the SQUID sensitivity is improved. To achieve feasible critical currents I_c in the μA range when implementing sub-μm sized JJs, a large critical current density j_c is needed. A critical current I_c in the μA range is desirable to make the SQUID stable, e.g., against RF interference or current noise of the bias current source, respectively. While standard SIS fabrication processes use a current density $j_c \approx 100\,\mathrm{A/cm^2}$, the PTB has established a process with a current density $j_{c,\mathrm{PTB}} = 1000\,\mathrm{A/cm^2}$. This allows for sub-$\mu$m sized JJs and consequently large shunt resistors R while still achieving critical currents in the range of $10\,\mu$A. However, this fabrication process, although superior to photolithographic processes with respect to the achievable lateral structure dimensions, does not come without drawbacks. It is worth to mention that structure writing can consume an extraordinary amount of time. Since all structures have to be written by EBL successively, the complete patterning process of typically two wafers with complex device structures takes three to four weeks.

The main steps of the fabrication process can be seen in Fig. 3.1. It is a slightly altered version of the process presented by Dolata et al.

and Khabipov et al. [DSZN05, KMD+14], expanded by the steps necessary to integrate AuPd shunt resistors and vertical interconnect access (VIAs). The structures are patterned on a 3" silicon wafer with a thickness $d_{wafer} = 350\,\mu$m, whose surface has been thermally oxidized to obtain a 300 nm thick SiO_2 isolation layer that is additionally covered by a 30 nm thick etching stop layer consisting of Al_2O_3. In the schematic process sequence cross section (cf. Fig. 3.1), this stack is summarized as the substrate. The first step of the *in situ* fabrication of the Nb/Al-AlO_x/Nb trilayer is done by the deposition of the 30 nm thick Al_2O_3 etching stop layer. Subsequently, a 150 nm thick Nb base layer (i.e. bottom Nb layer) is deposited using DC magnetron sputtering. This Nb layer is covered by an Al layer with a thickness of 10 nm using DC magnetron sputtering. By oxidation with pure O_2 at 20 °C for 10 min at a pressure of 5 mbar (i.e. the so-called exposition, given by pressure × time), an AlO_x layer with a thickness $1 - 2$ nm is created, forming the barrier. Using DC magnetron sputtering, the second Nb layer (i.e. the top Nb layer) is deposited on top of the AlO_x barrier, having a thickness of 150 nm, which completes the trilayer deposition. An extra SiO_2 layer with a thickness of 100 nm is deposited atop the trilayer using plasma enhanced chemical vapor deposition (PECVD). It serves as a mask in the following anodization process step while also increasing the reproducibility of the first etching step. Using thermal evaporation, a 30 nm thick Al layer is deposited onto the SiO_2 layer. Subsequently, this Al layer is covered with a two-layer polymethylmethacrylate (PMMA) resist which is then structured using EBL. PMMA is a positive resist, meaning Al under the resist exposed by the electron beam remains after a liftoff process. This forms the mask for the first etching process, thus defining the JJs, cf. Fig. 3.1(a).
In the first etching process, the SiO_2 layer is patterned by RIE using CHF_3. In a consecutive etching step, the Nb layer is patterned by RIE using CF_4. Since CF_4 does not etch Al or AlO_x, it automatically stops at the barrier or at the Al mask, respectively. To remove the Al mask and to expose the bottom Nb, an Ar IBE process step is used, cf. Fig. 3.1(b).
After the IBE, the exposed Nb is oxidized using anodization, which is an electrochemical redox reaction. The substrate is immersed into an aqueous solution of ammonium pentaborate $(NH_4)B_5O_8$ and ethylene glycol $C_2H_6O_2$ at room temperature. By applying a voltage of $\cong 20$ V between the wafer (anode) and a cathode which is also immersed in the solution, the exposed Nb gets reduced and forms a Nb_2O_5 layer with a thickness

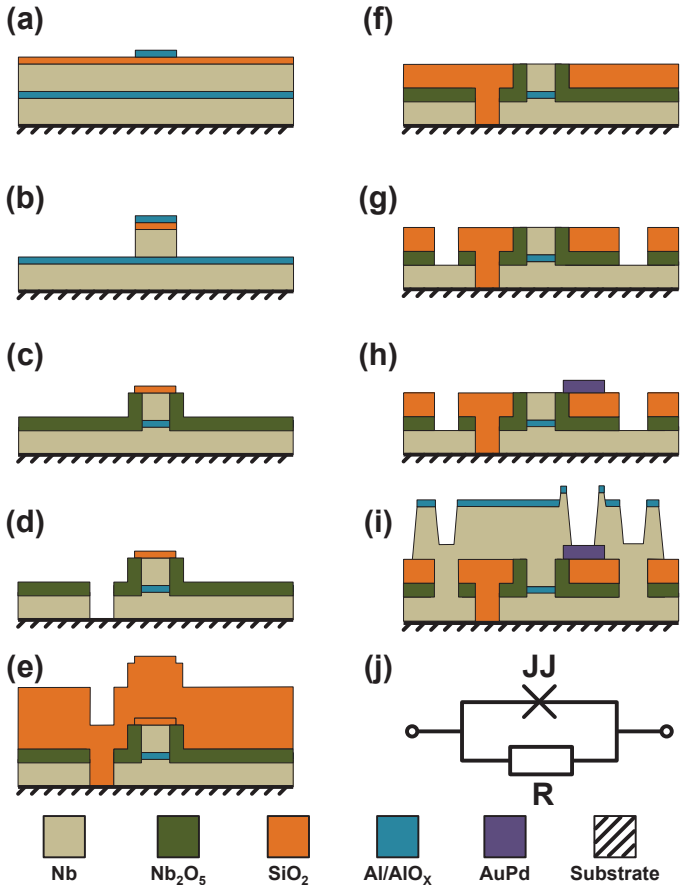

Figure 3.1.: Cross section of the SIS fabrication process. (a) Deposition of a SIS trilayer with SiO_2 cap layer and Al hard mask which defines the JJs. (b) Etching of SiO_2 and top Nb layer using RIE. (c) After removing the Al using Ar ion beam milling, the exposed bottom Nb is anodized. (d) Patterning of the bottom Nb layer by RIE using SF_6. (e) Deposition of a SiO_2 insulating layer. (f) Planarization and excavation of the top Nb layer using CMP. (g) Definition of VIAs using RIE. (h) Deposition and patterning of the AuPd shunt resistor using DC magnetron sputtering and EBL, respectively. (i) Implementation of the Nb wiring layer. (j) shows the equivalent circuit diagram of the resulting resistively shunted JJ.

of 45 nm. The effect of this anodization process is a significant reduction of subgap leakage currents, probably caused by damage of the junction perimeter or redeposition of conductive materials due to the etching process. Another advantage of the anodization step is that it counteracts an unwanted effect of the prior etching steps. Although huge effort has been put into parameter optimization to transfer the Al mask into the Nb and Al/AlO_x layer without any size deviations, usually a slight increase in the junction size can be observed. The anodization step, in contrast, decreases the junction size. By a carefully determined anodization voltage, both undesired effects cancel out each other, leading to practically no size deviation between Al mask and the actual JJ, cf. Fig. 3.1(c).
The bottom Nb layer can be patterned now. The required mask is defined by using EBL in combination with a negative tone resist. Subsequent etching, done by RIE using SF_6, removes both the Nb_2O_5 and the bottom Nb layer and finishes the bottom Nb layer definition, cf. Fig. 3.1(d).
In the following step, after removing the negative resist, a SiO_2 layer with a thickness of 600 nm is deposited onto the whole wafer by PECVD. To minimize the formation of pin holes within the SiO_2, which negatively affects the isolation between top and bottom Nb by creating superconducting shorts, after the deposition of 300 nm of SiO_2, the wafer is rotated by 90° before depositing the remaining 300 nm, cf. Fig. 3.1(e).
The deposition of the SiO_2 leaves a quite rugged wafer surface and a burried top Nb layer. A chemical-mechanical polishing (CMP) process is utilized to planarize the surface and excavating the top Nb layer, respectively. Here, the structured side of the wafer, which is rotating, is pushed against an also rotating polishing felt, moistened with a polishing chemical containing nanometer sized abrasive particles. Due to a careful determination of the endpoint of the CMP process, less than 50 nm of the top Nb layer are removed, cf. Fig. 3.1(f). Unfortunately, the optimum processing time of the CMP process is not constant but varies with JJ size and the pattern density of a given wafer section, respectively. To ensure the same polishing time for each section of the wafer, thus preventing JJs from getting damaged, CMP supporting structures are generously distributed around the important JJ and VIA areas. These supporting structures are formed by dummy structures in the Nb bottom and junction layer, respectively (e.g. see the many small square shaped structures in Fig. 4.36). With respect to the CMP process, the larger the supporting structures, the better. However, to maintain a high magnetic field compatibility of the devices precautions have been

taken to prevent the supporting structures from trapping magnetic flux. Thus, the lateral dimensions l_{CMP} of the implemented supporting structures where kept below $l_{CMP} \leq 2\,\mu$m, in most cases even $l_{CMP} = 500\,$nm [MC96]. To still ensure a supporting effect, many of these dummy structures where combined to larger square shaped formations (cf. Fig. 3.2). The whole CMP process is performed iteratively to prevent over-polishing.

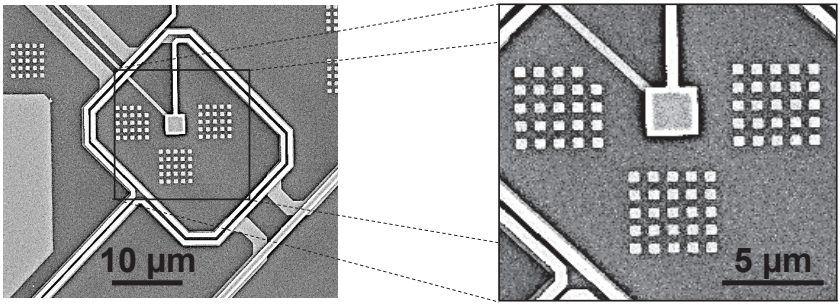

Figure 3.2.: CMP supporting structures, formed by dummy JJs, are generously placed around the SQUID structure to ensure homogeneous polishing time throughout the wafer. They are kept smaller than $2 \times 2\,\mu\text{m}^2$ to remain insusceptible for trapping magnetic flux in earth magnetic field during the cool down.

After each CMP iteration, the wafer is removed from the CMP machine, cleaned in a wafer-cleaner machine (Trystar) and inspected to determine the etching rate and to see if the endpoint is reached. Once the CMP process is completed, the wafer is carefully cleaned by an Ar plasma to remove CMP residues. Subsequently, the VIAs for interconnecting the top and bottom Nb layers as well as the VIAs to access the upcoming shunt resistors are being prepared, respectively. The VIAs are defined by EBL in combination with a positive resist. The etching of the SiO_2 and Nb_2O_5 is done by ICP-RIE using CHF_3, cf. Fig. 3.1(g).
At this point the AuPd shunt resistors are implemented. For their definition, a two-layer positive resist is being patterned by EBL. To ensure tight adhesion of the AuPd shunt resistors to the chip, a thin Al layer (about $2 - 3\,$nm) is deposited using DC magnetron sputtering which acts as a bonding agent. Subsequently, an AuPd layer with a thickness of 75 nm is being deposited using DC magnetron sputtering at $-10°$C and a pressure

of 0.1 mbar, respectively (see Fig. 3.1(h)). Subsequently, a lift off process in Acetone in an ultrasonic bath is performed. 75 nm of AuPd lead to a sheet resistance $\rho_{\square} = 5\,\Omega/\square$. Compared to the usually used $\rho_{\square} \approx 1\,\Omega/\square$ with an AuPd thickness of 300 nm, this is a quite high value. Due to the large shunt resistors required, such a large specific resistance per square is needed though, preventing laterally very narrow or very long resistor structures.
After the shunt resistor has been implemented, the Nb wiring layer with a thickness of 750 nm is deposited using DC magnetron sputtering. By using process steps explained above, a second Al mask (thickness 300 nm) is deposited and patterned. After the patterning process, the Al mask is not removed but stays on the wiring layer, cf. Fig. 3.1(i). Since no electrically active layer is integrated on top of the Al layer, it has no influence on the underlying devices. Fig. 3.1(j) shows the resulting equivalent circuit diagram of the fabricated resistively shunted JJ. Usually, the Nb wiring layer has a thickness of 150 nm. In this case, however, the Nb wiring has an extraordinary thickness of 750 nm. This is a result of the fact, that a wafer yields 20 separate $10 \times 10\,\mathrm{mm}^2$ chips which are commonly shared amongst various projects. Hence, various layout demands with respect to process parameters (e.g. layer thickness) arise. The extraordinary thickness of the Nb wiring layer is owed to two projects demanding on-chip trapping wires with high current carrying capacity.
In a final step (not shown in the fabrication process scheme in Fig. 3.1) the bond pads, that are currently covered by SiO_2, are exposed. Even though the bond pads have a lateral size of several hundreds μm, EBL is used for patterning a positive resist instead of optical lithography due to cost aspects. The etching of the SiO_2 is done in a wet chemical etching process using a ammonium fluoride etching solution based on hydrofluoric acid or by ICP-RIE in CHF_3.
Finally, it is worth mentioning that the given process description depicts the most important steps only. Various mandatory intermediate steps are omitted for clarity. In total all process steps add up to over 60, leading to clean room lead times of six working weeks for two wafers.

3.2. SNS process

Due to the fact that the designed SQUIDs were predominantly fabricated using the SIS process, the SNS process will only briefly described here. Details can be found in the doctoral thesis of O. Kieler [Kie17]. Most of the process steps of the SNS process are identical to the SIS process. The main difference is that the SNS process uses the normal conducting metallic compound HfTi as a barrier material. Additionally, no anodization step, no shunt resistors for the JJs and no VIAs are integrated in the process. VIAs are achieved by large JJs. In addition to the process described in [Kie17] an additional layer of AuPd on top of the Nb wiring layer (separated by PECVD deposited SiO_2 layer of 200 nm thickness) was integrated, which allows the implementation of on-chip heating structures that are overlapping the SQUID feed lines to achieve a more homogenous heat distribution across the chip.

3.3. Current sensor function blocks

The schematic configuration of an SCS has been presented in chapter 2.5. In this chapter, different designs will be worked out and layouts will be presented. To ensure a reliable and undisturbed sensor operation in a real NMR setup, some additional functional design elements have been implemented into the layouts. These function blocks will be explained and worked out, followed by a presentation of the actual implementation of SCS designs.

3.3.1. Input circuit current limiter: Q spoiler

When designing an SCS for pulsed magnetic field applications, like NMR, it is unavoidable to implement an input circuit current limiter into the input circuit. Even the smallest misalignment between the pickup loop and the excitation coil for the $\vec{B}_1$ field (they should be aligned perpendicular to each other) can lead to large induced currents in the input circuit once an excitation pulse is applied. This poses a variety of possible problems. Large induced currents can cause huge magnetic flux densities on the SQUID chip which can lead to trapped flux within the SQUID structure and consequently to a degradation of its characteristic curves [Rue08, HCSH85]. If

the induced current is larger than the critical current of the superconducting input circuit, flux jumps in the SQUID can occur leading to voltage jumps at the output of the SQUID electronics. In the worst case, this current can also destroy delicate parts of the input circuit like VIAs [Rue08]. There is a variety of technical approaches to realize input circuit current limiters. Probably the easiest way is to implement a thermal heat switch. It consists of a thin superconducting line in the close vicinity of a resistor. By applying a current to the resistor, the superconducting line becomes normal conducting due to the Joule heating of the resistor and thus leading to a fast decay of any induced currents. The switching between the superconducting and resistive state typically takes $5 - 10\,\mu$s [Supa]. A drawback of this approach is the possibility to heat up not just the desired superconducting line but the whole SQUID chip. Another simple approach is the implementation of a well defined constriction in the superconducting line. By knowing the film thickness d, the critical current density j_c of the thin film and the constriction width a_c, its critical current $I_{c,fd}$ can be calculated. This approach works quite well as long as all the relevant parameters are met sufficiently well during fabrication of the device. A more elegant way was introduced by Hilbert et al. by integrating a single or a series array of identical hysteretic JJs into the input circuit [HCSH85]. For signal currents smaller than the critical current $I_{c,JJ}$ of the JJs, the array has zero resistance. However large currents, e.g. induced by an RF pulse, can exceed $I_{c,JJ}$ and rapidly switch the array into the resistive state resulting in a large resistance. Due to the hysteretic behavior, the return current $I_{r,JJ}$ to the zero-voltage state will be smaller than $I_{c,JJ}$. Additionally, this approach theoretically offers the possibility to control $I_{c,JJ}$ by means of a magnetic field applied in-plane to the JJs, which however is quite impractical to implement in a shielded measurement environment. Hilbert et al. implemented the JJ array into a superconducting tank circuit with an extremely high quality factor (Q factor). Since the Q factor is heavily suppressed once the resistive state is reached, it is named Q spoiler, which is the commonly used name for this kind of circuitry nowadays. Drung et al. improved Hilbert's Q spoiler approach even further by replacing the JJs by a series array of identical unshunted SQUIDs [DAB+07]. By adding a flux modulation coil to each of the individual SQUIDs, their critical current I_c can be controlled comfortably by simply applying flux (cf. $I_c(\Phi_a)$ curve in 2.4). To be able to suppress the critical current to a maximum extent, each individual SQUID should preferably have a low β_L value (cf.

Fig. 3.3). Drung's Q spoiler approach has been adopted in our designs as schematically shown in Fig. 3.4. By using an SQUID array instead of a single SQUID, the normal conducting resistance is increased which leads to a faster input current decay.

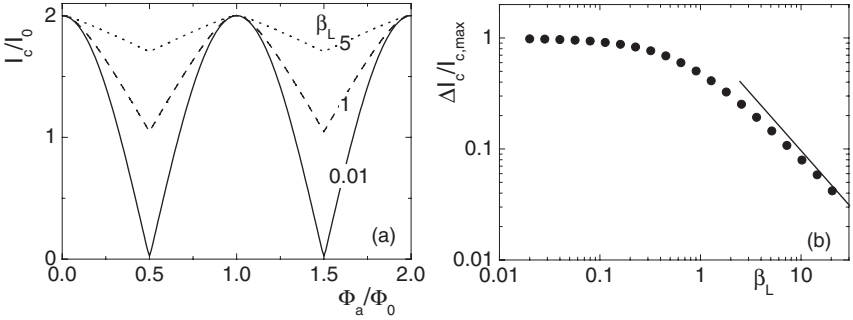

Figure 3.3.: (a) Simulation results showing the influence of β_L on $I_c(\Phi_a)$ characteristics (identical JJ parameters were used). (b) shows simulation results of the modulation depth $\Delta I_c/I_{c,max}$ for a wide variety of β_L. Adapted from [CB04].

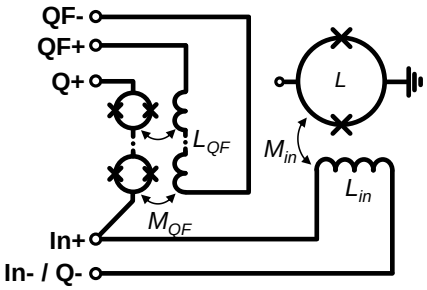

Figure 3.4.: Schematic illustration of the implementation of a Q spoiler into the input circuit. It consists of a series array of unshunted SQUIDs. Due to the flexible wiring scheme its use is optional (by connecting the pickup coil to the **Q+**/**Q-** labeled terminals).

Physical implementations of a Q spoiler can be seen in Fig. 4.6 for the SNS and in Fig. 4.18 for the SIS fabrication process.

3.3.2. On-chip RF filter

In appendix A.1 it is worked out that RF filtering of the feed lines is indispensable. However, to keep the amount of metal parts in the vicinity of the NMR/MRI sample, which could lead to magnetic field distortions (e.g. caused by eddy currents) to a minimum, the RF filters are implemented directly on-chip. Two different filter topologies have been implemented (cf. Fig. 3.5(a) for the SQUID feed lines and (b) for any on-chip modulation coil, respectively). Both topologies have a cutoff frequency $f_{-3dB} \approx 40\,\mathrm{MHz}$ and a slope of $-20\,\mathrm{dB/decade}$ in the stopband, i.e. the frequency range above f_{-3dB}. Figure 3.5(c) depicts the symbol for both filter implementations used in upcoming schematic diagrams. The feed lines for the SQUID [DS15] are filtered by a first-order T-filter topology. The filter capacitor suppresses low frequency noise arising from the current noise $S_{i,R_{\mathrm{TF}}}^{1/2}$ of the filter resistors, but comes at a cost of using more chip area. Additionally, it damps out signals at the Josephson frequency f_J originating from the JJs by the approximated wave impedance $Z = 24\Omega + 24\Omega \approx 50\Omega$, thus preventing line reflexions. The filters for the on-chip modulation coils are realized in a first-order X-filter topology using resistors and superconducting coils. Even though the resulting resistor current noise $S_{i,R_{\mathrm{XF}}}^{1/2}$ is increased compared to the T-filter, its influence is negligible for large current sensor SQUIDs. Since the reciprocal mutual inductance $1/M_{fb}$ between the SQUID loop and the modulation coil commonly is in the range of $50\mu\mathrm{A}/\Phi_0$, the resulting flux noise $S_{\Phi,R_{\mathrm{XF}}}^{1/2}$ due to $S_{i,R_{\mathrm{XF}}}^{1/2}$ in the worst case of the implemented filter resistors $39\,\Omega \,||\, 39\,\Omega = 18.5\,\Omega$ is approx.

$$\begin{aligned} S_{\Phi,R_{\mathrm{XF}}}^{1/2} &= S_{i,R_{\mathrm{XF}}}^{1/2} \cdot M_{fb} \\ &= \frac{\sqrt{4 \cdot k_B \cdot 4.2\,\mathrm{K}/18.5\,\Omega}}{\sqrt{\mathrm{Hz}}} \cdot \frac{\Phi_0}{50\mu\mathrm{A}} \\ &\approx 70\,\frac{\mathrm{n}\Phi_0}{\sqrt{\mathrm{Hz}}}, \end{aligned} \tag{3.1}$$

thus becoming noticeable only for SQUIDs that have an equivalent flux noise density $S_{\Phi}^{1/2} \approx 200\,\mathrm{n}\Phi_0/\sqrt{\mathrm{Hz}}$ or better. The corresponding frequency responses are shown in Fig. 3.5(d).

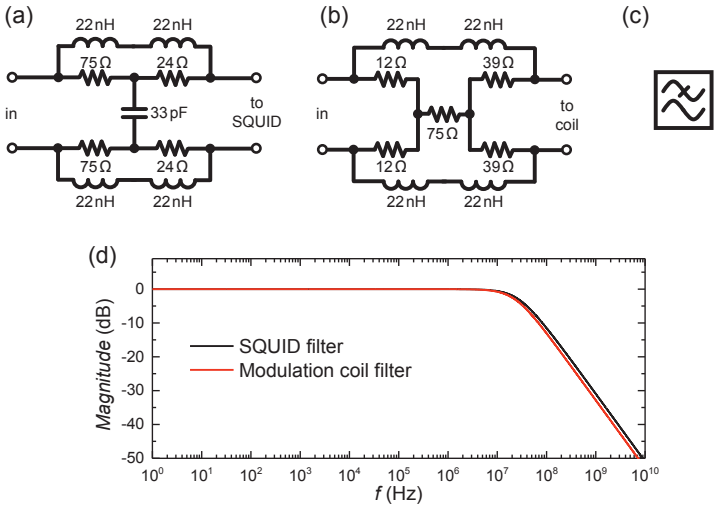

Figure 3.5.: RF filter design for the SQUID (a) and the modulation coils feed lines (b), respectively [DS15]. (c) depicts the symbol for both filter implementations used in schematic diagrams. (d) shows the simulated frequency response of both filter topologies using LTspiceIV [Lin]. Both filter topologies have a cutoff frequency f_{-3dB} of approx. 40 MHz. The SQUID filter was loaded with $R = 15\,\Omega$ for the simulation to account for the resistive loading caused by the SQUIDs dynamic resistance R_{dyn} at the working point.

3.3.3. Input coil and transformer damping

As discussed in chapter 2.5, by introducing a superconducting intermediate transformer circuit, parasitic resonances and transmission line resonances in the input circuitry can be minimized. To ensure proper sensor operation and to exclude the occurrence of resonances, they should be actively damped. A simple yet effective way to properly damp out those resonances is to shunt L_i by a RC element (cf. red colored components in Fig. 3.6) [SR87]. The resistor R_{RC} terminates the stripline and therefore suppresses or damps resonances, respectively. The shunt capacitor C_{RC} decreases $f_{p,i}$ into a region far below f_{wp}, usually to a frequency of around $10 - 100$ MHz [CB04]. Also, as for the RF input filters, C_{RC} successfully suppresses low frequency noise arising from the current noise $S^{1/2}_{R_{i,\mathrm{RC}}}$ of R_{RC}, leaving the

total noise performance almost unaffected. Typical resistor and capacitor values are of the order of a few ten Ohms and a couple hundred pF [CB04].

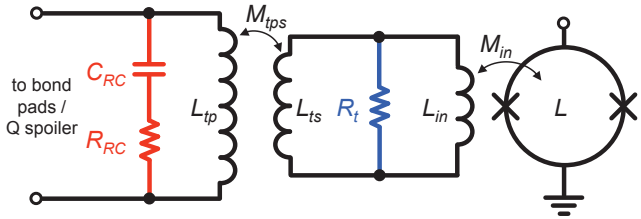

Figure 3.6.: Schematic arrangement of the input coil and intra-transformer damping scheme. The red colored components R_{RC} and C_{RC} form the RC shunt to suppress parasitic resonances in the input coil while blue colored resistor R_t damps parasitic intra-transformer resonances [CB04, HC85, KAT87, KKS+88].

The same argumentation also applies to the intermediate transformer, so in principle the same RC shunt circuitry could be applied to it, too. A capacitor, however, would introduce a large superconducting area in the close vicinity of the SQUID. It is prone to easily trap flux [DAB+07]. Thus, the microstrip transmission resonances are not moved into a frequency range below f_{wp}. Fortunately, due to the small line width of L_{in} and the relatively small washer of L_{ts}, the parasitic capacitance $C_{p,t}$ is small. Additionally, the inductance of L_{ts} is small compared to L_{tp}, leading to a parasitic frequency of the intermediate transformer $f_{p,t} \gg f_{wp}$. A drawback of the absence of the capacitor is, though, that the current noise $S_{i,R_t}^{1/2}$ of R_t is not damped, leading to a slightly increased overall noise of the SCS, yet the overall benefit due to smooth characteristic curves prevails [DS15, CRD+91].

3.4. Numerical methods

For the design of SQUIDs or to investigate SQUID parameters after characterization measurements, two different numerical methods have been used. For the design process, the software 3D-MLSI was used [Kha03]. In particular, it was used to simulate the inductance of superconducting loops of the mutual inductance of nearby superconducting structures. However, it also allows to simulate and visualize current and magnetic field distributions of

two-dimensional superconducting structures. Based on the Maxwell- and the London-equations, it calculates the current distribution within a structure which has been provided by the user in a text file. It relies on the finite-element-method and solves the resulting set of differential equations with a not specified numerical method. SQUID parameters are determined using a software written by R. Kleiner. It solves the Langevin equations (2.18) and the phase relation (2.19) using a 5^{th} order Runge-Kutta-Fehlberg method and is able to output every characteristic curve of a SQUID. All SQUID parameters, the externally applied flux Φ_a and the temperature (in form of the noise parameter Γ) can be set.

4 | SQUID based current sensor

In this chapter, two SQUID based current sensor designs will be presented: one that endeavors a new approach (chapter 4.1) and a more common design (chapter 4.4). The design specifications are aimed to be optimized for the different tasks that the ULF-MRI system is used for. After presenting different implementation techniques for SCS, the complete design and fabrication process of the two different layouts will be shown. Finally, characterization measurements of the developed SCS are presented.

4.1. Multi-SQUID based current sensor

To obtain high-quality high-resolution spectra of hyperpolarized chemicals, averaging of acquired voltage-vs-time traces is mandatory. This is no problem when performing characterization measurements of the chemical solution. Here the only limiting factor is the holding time of the chemical solution inside of the sample reactor due to evaporation of the solvent. Furthermore, the solvent can be refilled, rendering solvent evaporation to be no problem. However, in the scope of *in vivo* measurements, the limiting factor is the endurance of the specimen under test. Therefore, the goal is to minimize physical stress acting on the specimen, which requires data acquisition times as short as possible. To minimize the required time for high quality spectra acquisition one approach is trying to take full advantage of the existing SQUID electronics. It allows the readout of three independent SQUID channels, i.e. three separate SQUIDs. Thus a layout is developed containing three as far as possible identical, independent SQUIDs on a single chip, all sharing the same input coil (cf. Fig. 4.1). In principle, this way all three SQUIDs simultaneously detect the same input signal sensed

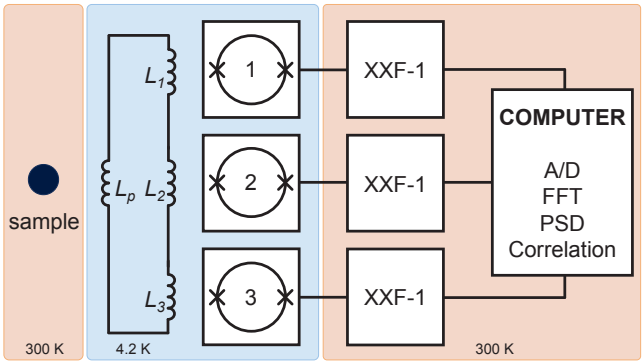

Figure 4.1.: Schematic diagram of the multi-SQUID measurement scheme.

by the pickup coil L_p simultaneously. In data post-processing, the so acquired three voltage-vs-time traces or their FFT can easily be processed in real-time. Moreover, cross-correlation processing of the acquired data is possible. Each SQUID has an intrinsic equivalent flux noise density $S_\Phi^{1/2}$ which is independent of the other SQUIDs. In principle, the only correlated signal each SQUID detects is the signal detected by the pickup coil (and any offset magnetic field coupling to the pickup coil). It has been shown, that this way for somewhat similar setups, environmental noise can be suppressed to a great extent [RRFE13, KRE+14, KE16, Fin59].

4.2. First generation of Multi-SQUIDs: SNS based devices

The first generation of the multi-SQUID design was planned and laid out for the PTB SNS process described in 3.2. Due to the normal conducting barrier material HfTi, the SNS process yields an extremely large critical current density $j_{\mathrm{SNS}} \approx 300\,\mathrm{kA/cm^2}$. Additionally, the shunting of the JJ is done intrinsically by the barrier layer and yields small resistance values of $R_\mathrm{n} < 1\,\Omega$. However, unfortunately both conditions are undesirable for the design of SCS. On the one hand, due to the small intrinsic shunts R_n the resulting critical voltage $V_c = I_0 \cdot R_n$ is quite small and actually demands large critical currents I_0. On the other hand, obtaining $\beta_L \approx 1$ with the

huge j_{SNS} is impeded. It requires either ultra small JJs (e.g. $j_{SNS} \approx 300\,\mathrm{A/cm^2}$ yields $I_0 = 30\,\mu\mathrm{A}$ for a square shaped JJ with $d_{JJ} = 100\,\mathrm{nm}$), extremely small SQUID inductances L, or both in combination. At first sight, small L values seem favorable by means of low flux noise values $S_\Phi^{1/2}$. However, coupling a signal to the SQUID becomes more and more difficult, the smaller L becomes [MPGM+16, NBX+13]. Additionally, the smaller the JJ, the more it is susceptible to failure during production.
The drawbacks of the SNS process have lead to a SCS layout employing a mixture between the double-transformer layout (see chapter 4.4) and directly coupled SCS (see Fig. 4.2). In this directly coupled SCS layout, the input coil L_i is directly patterned on top of the secondary side of the input transformer (implemented as a large washer with the inductance L_W). The washer L_W is galvanically coupled to the SQUID inductance L. Hence, the screening current of the secondary side of the input transformer coil becomes the input signal for the SCS, leading to a relatively tight coupling even for small SQUID inductances L [BRD+15, KML+93].

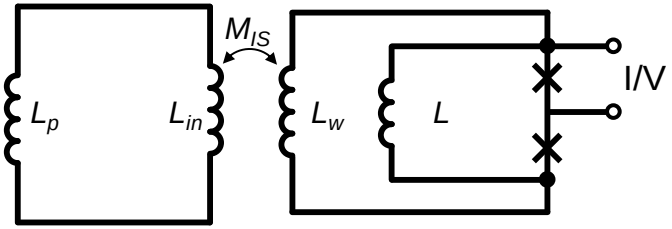

Figure 4.2.: Schematic layout of a directly coupled SNS based magnetic field sensor. The coil representing the secondary side of the input transformer is galvanically coupled to the SQUID inductance. This way, the screening current of the input transformer's secondary side becomes the input signal for the SQUID. Thus, good coupling between the pickup coil L_p and the SQUID is achieved.

A schematic overview of the complete SCS layout and the physical implementation can be seen in Fig. 4.3(a) and (b), respectively. The chip is square shaped with a lateral length $l_{w,chip} = 3.2\,\mathrm{mm}$. All the additionally needed and discussed features, except the washer damping resistor, have been implemented and will be explained in detail. The pickup coil L_p is either connected to the pads **In+**/**In-** (no Q spoiler) or to **Q+**/**Q-**, which

uses the optional Q spoiler. Any induced current in L_p then couples to the individual SQUIDs via the respective input transformer and the mutual inductance M_{ISn} ($n \in [1,3]$). The Q spoiler can be flux biased by connecting a current to **QF+**/**QF-**. Each individual SQUID is flux biased by a current connected to **nF+**/**nF-** ($n \in [1,3]$), which allows standard FLL operation.

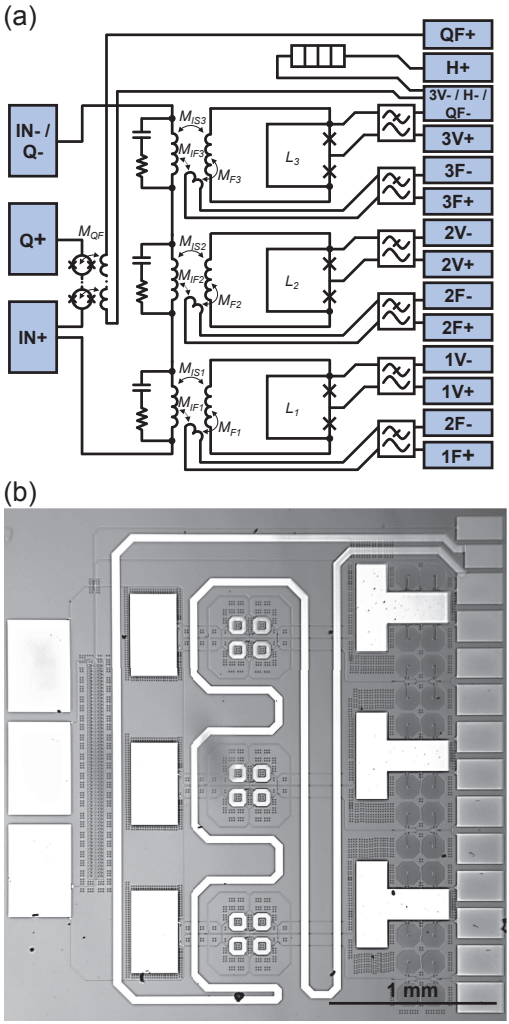

Figure 4.3.: (a) Schematic multi-SQUID current sensor layout. (b) Micrograph of the implemented chip.

The individual SQUIDs have been implemented as first-order series gradiometers (see the zoomed section in Fig. 4.4). The JJs are square shaped and have a lateral dimension $l_{JJ} = 150\,\mathrm{nm}$, which in combination with $j_{\mathrm{SNS}} = 300\,\mathrm{kA/cm^2}$ leads to the critical current $I_0 = 67.5\,\mu\mathrm{A}$. Three different SQUID inductance values $L = 12.3\,\mathrm{pH}, 15.5\,\mathrm{pH}, 20.0\,\mathrm{pH}$ were chosen to counterbalance any possible deviations of j_{SNS} and lead to $\beta_L = 0.8, 1.0, 1.3$.

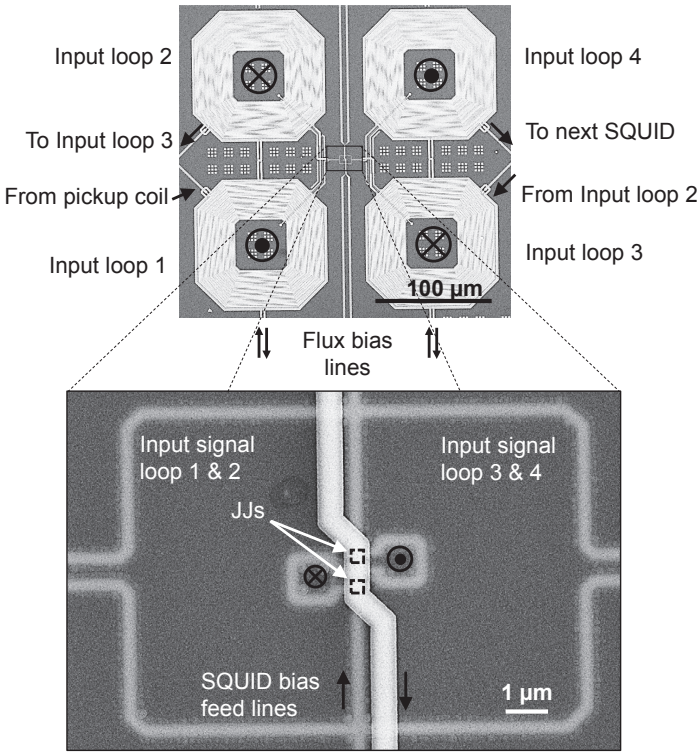

Figure 4.4.: SEM image of the SNS multi-SQUID input circuitry and a zoomed section of the SQUID cell. In the zoomed section, the bottom layer is blurry because it is buried under an insulating SiO_2 layer.

The biasing lines of the SQUID are asymmetrically connected to minimize crossing between feed lines and the SQUID structures (cf. zoomed section in Fig. 4.4). Due to the resulting asymmetry α_L in the inductance of the SQUID, tilted $I_c(\Phi)$-curves can be expected.

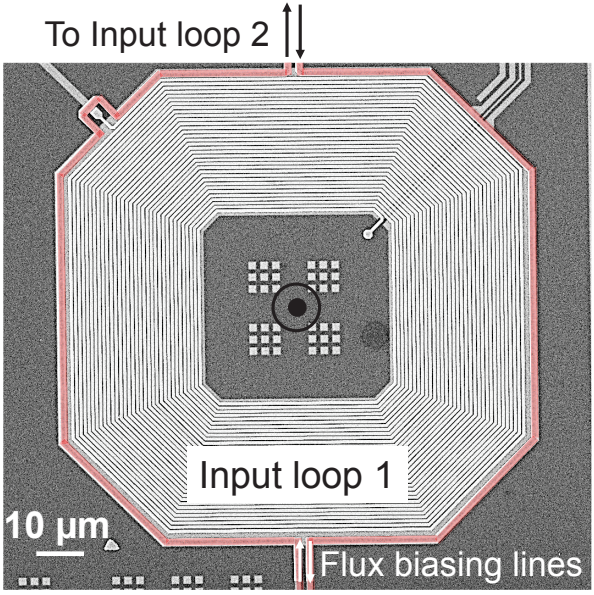

Figure 4.5.: Single input loop of the SNS based SCS surrounded by a single turn flux biasing coil (highlighted in red). The single turn feedback coil is patterned directly on top of the input washer inductance L_w.

The estimate of β_C is quite hard for this process. This is caused by the normal conducting barrier layer. β_C relies both on R and C of a junction. The peculiarity of the SNS process is that it couples R and C. On the one hand, by decreasing the junction area, the capacitance decreases, since $C \propto A_{\mathrm{JJ}}$. On the other hand, in the same turn R increases because $R \propto 1/A_{\mathrm{JJ}}$. Experience with the SNS process teaches, that the fabricated devices often show $\beta_C \approx 0.5 - 1$ as it is only affected by the critical current density [NBX$^+$13, MPGM$^+$16]. Care was taken to implement a very symmetrical

SQUID layout to achieve a highly balanced design, minimizing coupling from parasitic magnetic fields originating from bias currents or currents in the input circuitry [DAB+07]. The input transformer is implemented in a second-order series gradiometer configuration surrounding the SQUID cell. The input coil is patterned directly on top of the washer L_w with a line width $l_{w,in} = 500\,\text{nm}$. The input circuitry of every individual SQUID is shunted by an RC shunt (cf. Fig. 4.38). To vary the input coil inductance L_{in} the number of coil turns is altered while the inductance L_{PTS} of the secondary side of the primary transformer is kept almost constant. To cover the inductance ranges of typical pickup coils L_p (as experience teaches $L_p \approx 400 - 1600\,\text{nH}$, depending on the gradiometer order and the loop diameter), three different total input coil inductance values $L_{in,tot}$ have been realized: $L_{in,tot} \approx 900\,\text{nH}, 1200\,\text{nH}, 1680\,\text{nH}$, achieved by 26, 31 and 36 turns per transformer primary. Flux biasing is achieved by a feedback coil patterned on top of the washer inductance L_w (cf. Fig. 4.5).

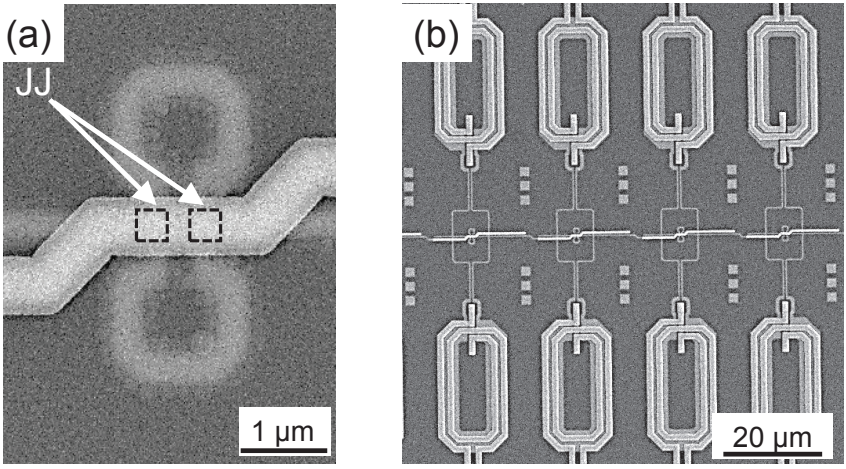

Figure 4.6.: (a) SEM image of a single Q spoiler SQUID which is implemented as a first-order parallel gradiometer. (b) Four Q spoiler SQUIDs and their individual gradiometric flux bias coils which are coupled directly to the individual SQUIDs.

The Q spoiler was realized by a series array of 64 first-order parallel gradiometric SQUIDs (cf. Fig. 4.6(a)). Each individual SQUID is directly

coupled to two washers. On top of the washers, an input coil is patterned for flux biasing and therefore to control its maximum critical current before becoming resistive (cf. Fig. 4.6(b)). Each JJ has a lateral dimension $l_{JJ} = 100\,\text{nm}$, resulting in a maximum critical current of $30\,\mu\text{A}$. The parallel gradiometric approach results from the large value of j_{SNS} and is needed to achieve small inductance values $L_{QS} \approx 10\,\text{pH}$ which yields $\beta_L \approx 0.3$. This allows for a critical current modulation $(I_{c,max} - I_{c,min})/I_{c,max} = \Delta I_c/I_{c,max} \approx 0.78$ (cf. Fig. 3.3), resulting in a minimum critical current $I_{c,QS}(\text{on}) = 13.5\,\mu\text{A}$ once the Q spoiler is activated (i.e. applied flux $\Phi_a \approx 0.5\Phi_0$). Figure 4.7 shows scanning electron microscope (SEM) images of the realized filter implementation.

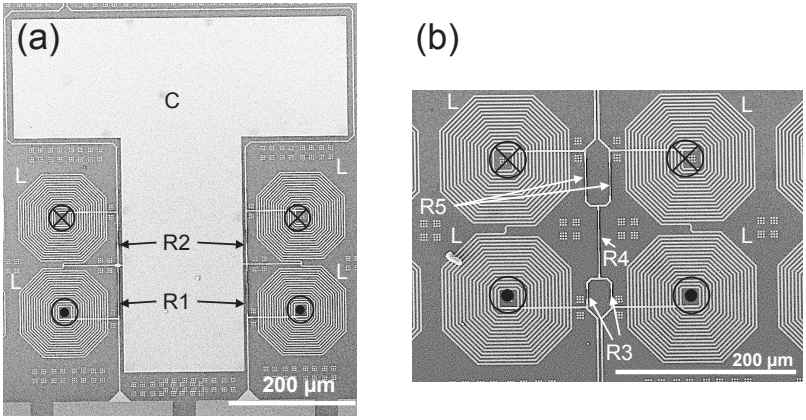

Figure 4.7.: (a) On-chip filter for the SQUID feed lines while (b) Filter for the flux bias lines.

The SQUID feed line filter can be seen in (a) while the modulation coil feed line filter is shown in (b). Each filter inductor is realized by a coil consisting of 16.5 windings with a line width of $2\,\mu\text{m}$, leading to $L \approx 22\,\text{nH}$. The filter resistors $R1-R5$ are realized by $1\,\mu\text{m}$ wide AuPd lines. The series connected pair of inductors of one filter branch are wound in an opposite manner to make them insusceptible to homogeneous magnetic offset fields yet sustaining the filter effect. An additional heating resistor, implemented by

an on-chip meander shaped AuPd structure, with a resistance $R_H = 700\,\Omega$ (cf. Fig. 4.35), allows for convenient expelling of trapped flux. The employed Magnicon XXF-1 readout electronics offers a maximum heater voltage $V_H = 13\,\mathrm{V}$, resulting in a maximum heating power $P_{H,max} = 0.24\,\mathrm{W}$ and a heating power density $\rho_{P,H} = 0.24\,\mathrm{W}/(l^2_{w,chip}) = 0.024\,\mathrm{W/mm^2}$. According to Drung *et al.*, $\rho_{P,H} = 0.01\,\mathrm{W/mm^2}$ is sufficient to heat up the SQUID chip immersed in liquid helium [DAB+07]. Due to the on-chip heater, no additional resistor on the sample holder is needed, reducing its size and complexity. Although the heater is not necessary when operating the SQUID using the Magnicon XXF-1 (since it offers direct JJs heating [Mag13a]), it maintains the heating capability if a different readout electronic might be used.

4.2.1. Transport measurements

Using the measurement setup described in the appendix A.1, the characterization of the transport characteristics of the SQUIDs has been performed at $T = 4.2\,\mathrm{K}$. In total, 20 current sensor SQUIDs have been characterized. Representative for all measured SQUIDs, the characteristics of the SQUID A1_B2_L[1] will be presented since the observed features are similar for all devices. Figure 4.8 shows the $I(V)$ characteristics for $\Phi_a = n\Phi_0$ (black) and $\Phi_a = (n + 1/2)\Phi_0$ (red).

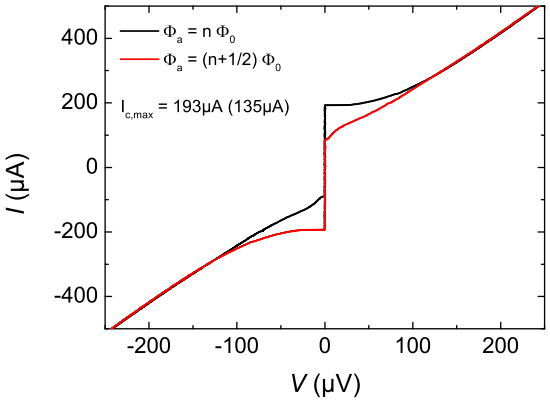

Figure 4.8.: $I(V)$ characteristics of the device A1_B2_L for $\Phi_a = n\Phi_0$ (black) and $\Phi_a = (n + 1/2)\Phi_0$ (red).

The maximum critical current $I_{c,max} = 193\,\mu\mathrm{A}$ is approximately 40% larger than the design value of $135\,\mu\mathrm{A}$. Throughout the wafer, the average current density j_{SNS} of all measured devices is $j_{SNS} = (377.7 \pm 35.5)\,\mathrm{kA/cm^2}$, which is 26% larger than the design value $j = 300\mathrm{kA/cm^2}$. This can be attributed to a slightly too thin barrier layer d_{HfTi}. Figure

[1] A1 denotes the chip position on the wafer. On each wafer the chips are arranged in a 4x5 matrix. A1 is the top left chip while D5 would be the lower right chip. B denotes the position of the SQUID-triple on each chip. On each chip, 6 SQUID-triples are arranged in a 2x3 matrix. A is the top left SQUID-triple while F would be the lower triple. 2 indicated the SQUID in the middle of each triple. L indicates the inductance of the input coil and is assigned to $L_{in,tot} = 1200\,\mathrm{nH}$.

4.9 shows the extracted critical current density dependency $j_c(d_{\mathrm{HfTi}})$ at $T = 4.2\,\mathrm{K}$ which indicates that d_{HfTi} is only $\approx 0.5\,\mathrm{nm}$ too thin [Kie17]. Using the slope of the $I(V)$-curve, the normal conducting resistance can be determined to be $R_n = 0.5\,\Omega$. The black curve is on the verge of showing a hysteretic behavior, numerical simulations of the RCSJ model yields $\beta_C = 0.89$. This leads to a junction capacitance $C_{JJ} = 3.06\,\mathrm{pF}$. Both curves show a small step-like feature at $V = \pm 73\,\mu\mathrm{V}$ (red curve/black curve). The feature can be attributed to LC-resonances, which should theoretically appear at $V \approx \pm 76\,\mu\mathrm{V}$. The red curve shows an additional feature close to the critical current I_c. At low voltages the differential resistance decreases in a narrow voltage range. This feature does not appear in numerical simulations based on the RCSJ model. Similar features have been observed in other JJs and were attributed to Andreev reflections [Kie17, Tin96].

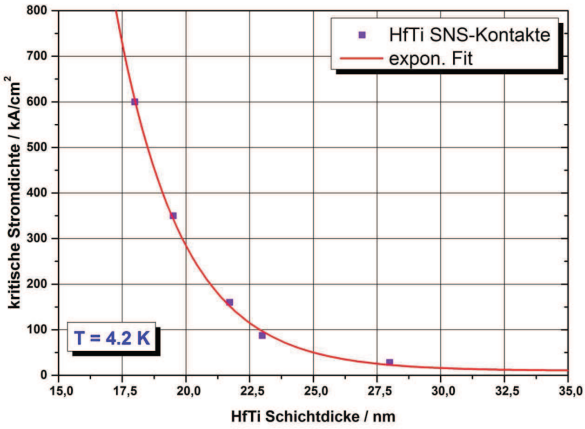

Figure 4.9.: Dependency of the critical current density j_c on the HfTi barrier thickness d_{HfTi} of the SNS fabrication process at the PTB. Taken from [Kie17].

Figure 4.10 shows the $I_c(\Phi_a)$ characteristics, normalized to Φ_0. The reciprocal mutual inductance $1/M_F = 268.8\,\mu\mathrm{A}/\Phi_0$ is quite large, although the feedback signal is fed into the input transformer.

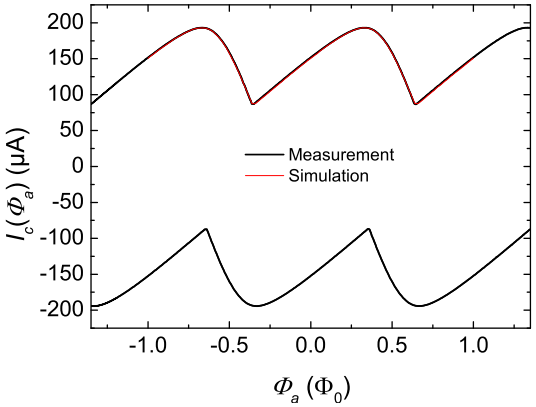

Figure 4.10.: $I_c(\Phi_a)$ characteristics of the device A1_B2_L. The flux axis is normalized to Φ_0. The black curves show the measurement while the red curve is a simulation.

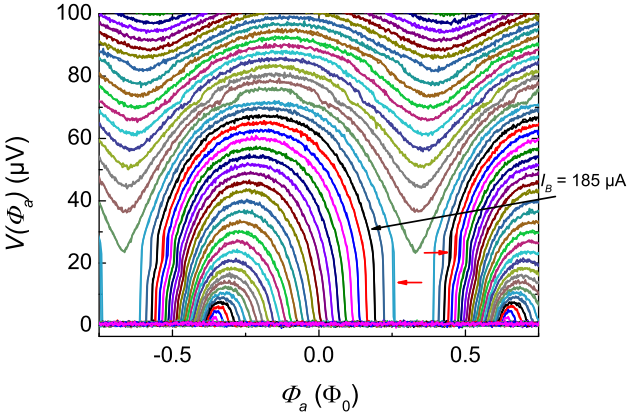

Figure 4.11.: $V(\Phi_a)$ characteristics of SNS based SQUIDs for bias currents ranging from $I_B = +5... + 350\,\mu$A in $\approx 5\,\mu$A steps. The maximum transfer function $V_\Phi = 740\,\mu\text{A}/\Phi_0$ was found for $I_B = 185\,\mu$A (black arrow).

Using the observed modulation depth $\Delta I_c/I_{c,max} = 0.56$ and Fig. 3.3(b), the screening parameter can be estimated to the value $\beta_L = 0.75$, which matches very well with numerical simulations of the measured curves. However, the extracted SQUID inductance is only $L_{\mathrm{meas}} = 8.0\,\mathrm{pH}$, which is almost only half of the design value $L_{\mathrm{dsg}} = 15.5\,\mathrm{pH}$. This indicates a very tight coupling between the input transformer and the SQUID inductance and a resulting screening of the SQUID inductance by the input transformer.
As already mentioned in chapter 4.2, due to the asymmetric biasing, the $I_c(\Phi_a)$ curve is tilted. The asymmetry parameter α_L was extracted using numerical simulations, yielding $\alpha_L = 0.88$.
Fig. 4.11 shows the $V(\Phi_a)$ characteristics for various bias currents. It can be seen that some curves show a slightly hysteretic behavior, owed to β_C close to unity (red arrows). The maximum transfer function $V_\Phi = 740\,\mu\mathrm{V}/\Phi_0$ was found for $I_B = 185\,\mu\mathrm{A}$. In the voltage range between $V = 10 - 30\,\mu\mathrm{V}$ and $\Phi_a \approx \pm 0.5\,\Phi_0$ fine-structures can be observed.

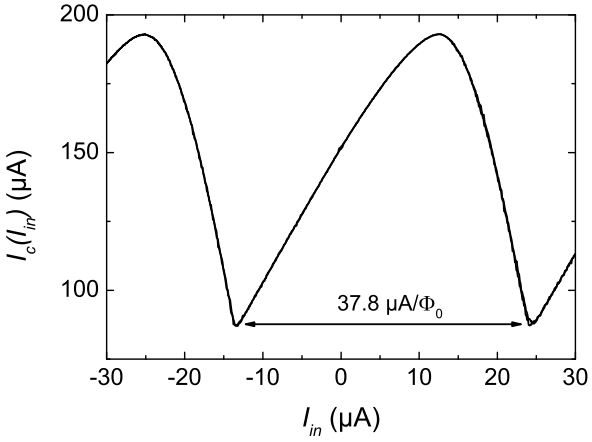

Figure 4.12.: I_c vs. I_{in} shows the input sensitivity $1/M_{in} = 37.8\,\mu\mathrm{A}$ of the SNS based device L_A1_B2.

This behavior was reported in literature [Rue08, KAT87]. They can be attributed to resonances in the input coils and could be suppressed by *RC*-

shunts across the input coil. Since RC-shunts are already implemented, the resonance is most probably caused by the lack of a washer shunt resistor R_W. It has been omitted since it was presumed that $S_\Phi^{1/2}$ would deteriorate due to the resistor current noise $S_{i,R_W}^{1/2}$ in combination with the direct coupling approach. Fig. 4.12 shows the $I_c(I_{\mathrm{in}})$ of the SCS. It is, among the $S_\Phi^{1/2}$ spectra, the most important curve for a current sensor since it allows to determine the input sensitivity $1/M_{in}$. For the period of oscillation the input sensitivity was found to be $1/M_{in} = 37.8\,\mu\mathrm{A}/\Phi_0$.

4.2.2. Noise characteristics

The SQUID was not biased at its optimum working point with the bias current $I_B = 185\,\mu\mathrm{A}$ because the Magnicon XXF-1 electronics can only supply $180\,\mu\mathrm{A}$ without modifications. Therefore, $I_B = 180\,\mu\mathrm{A}$ was chosen. As a result, the transfer function was slightly reduced to $V_\Phi \approx 725\,\mu\mathrm{V}/\Phi_0$ (compared to $V_\Phi = 740\,\mu\mathrm{V}/\Phi_0$) at $\Phi_B = 0.18\,\Phi_0$. The presented $S_\Phi^{1/2}$ has a frequency resolution $\Delta f = 1\,\mathrm{Hz}$ and was averaged for $n_{\mathrm{avg}} = 100$ times. The

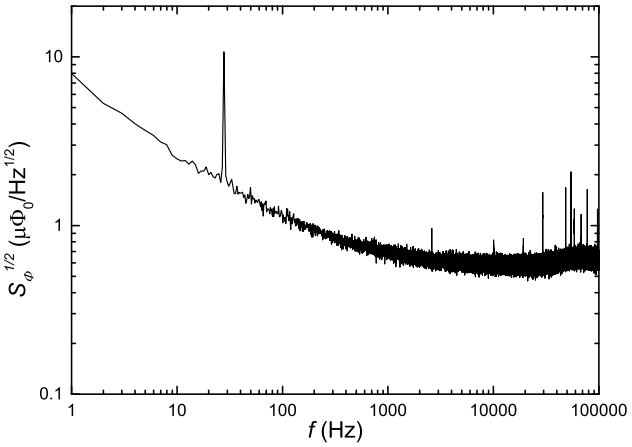

Figure 4.13.: Noise spectra of the current sensor SNS based SCS.

spectrum shows a $1/f$ corner frequency of $\approx 400\,\mathrm{Hz}$, which is quite common for SNS based devices [NBX$^+$13, BRD$^+$15, MPGM$^+$16]. The white noise level is $S_\Phi^{1/2} = 590\,\mathrm{n}\Phi_0/\mathrm{Hz}^{1/2}$. Even though the inductance of the SQUID is quite small and lower $S_\Phi^{1/2}$ values could be expected [BRD$^+$15], probably resonances and hysteresis are present but are not visible in the characteristic curves due to thermal noise. This can lead to an increased spectral density of voltage noise, leading to an increased equivalent density of flux noise. In combination with the input sensitivity $1/M_\mathrm{in} = 37.8\,\mu\mathrm{A}/\Phi_0$, an input noise current $S_i^{1/2} = 21.9\,\mathrm{pA}/\mathrm{Hz}^{1/2}$ is found. At $\approx 70\,\mathrm{kHz}$, a slight increase in the flux noise spectrum can be seen. This feature was present for all investigated devices at approximately the same frequency. Its origin is unclear, but most likely caused by a washer resonance due to the lack of a washer damping resistor.

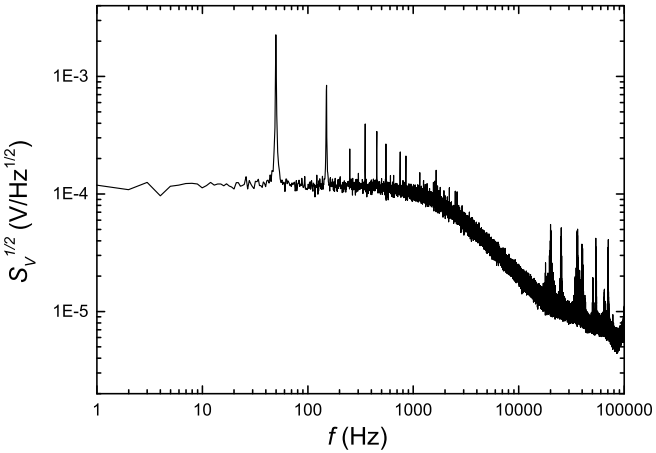

Figure 4.14.: Voltage noise spectrum used to determine L_in.

To determine the input inductance, the input coil was shorted using a bond wire with the length $l_\mathrm{bond} \approx 1.25\,\mathrm{mm}$ (determined after the measurement using a calibrated microscope). Using the bond wire diameter $d_\mathrm{bond} =$

25 μm and the specific resistance of aluminium $\rho_{\mathrm{Al}} = 2.65 \cdot 10^{-2}\,\Omega\,\mathrm{mm}^2/\mathrm{m}$, this leads to a resistance $R_{\mathrm{bond}} = 16.8\,\mathrm{m}\Omega$. Using the cut-off frequency $f_{-3\mathrm{dB}} = 1800\,\mathrm{Hz}$ of the resulted voltage noise spectrum (cf. Fig. 4.14) and taking into account the inductance of the bond wire of $L_{\mathrm{short}} = 10\,\mathrm{nH}$, for $L_{\mathrm{in}} = 1.49\,\mu\mathrm{H}$ was found which is $\approx 12\,\%$ smaller than the design value of $L_{\mathrm{in,design}} = 1.68\,\mu\mathrm{H}$.

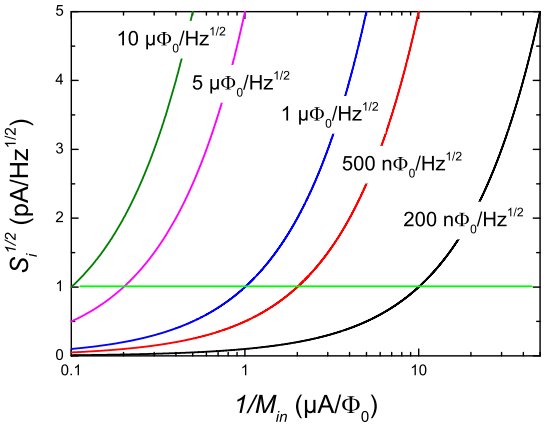

Figure 4.15.: Current noise density $S_i^{1/2}$ vs. input sensitivity $1/M_{in}$ for various equivalent flux noise densities $S_\Phi^{1/2}$. To achieve a desired current noise density $S_i^{1/2}$, e.g. $S_i^{1/2} = 1\,\mathrm{pA}/\sqrt{\mathrm{Hz}}$ (indicated by the green horizontal line), either a SQUID with very low flux noise and moderate input coupling (black curve) or a SQUID with high flux noise in combination with a very high input coupling could be used (green curve), respectively.

Nano-sized SQUIDs usually achieve very low $S_\Phi^{1/2}$, however tight input coupling is hard to achieve, as can be seen in Fig. 4.12. Although for nano-sized SQUID based current sensors, $1/M_{\mathrm{in}} = 37.8\,\mu\mathrm{A}/\Phi_0$ is a quite impressive value [BRD+15], it renders this current sensor approach as unfeasible and illustrates the drawbacks of the high critical current density $j_{\mathrm{c,SNS}}$. Commercially available micro-sized current sensors based on a SIS fabrication process with a critical current density $j_c \approx 100\,\mathrm{A}/\mathrm{cm}^2$ allow much larger SQUID inductances, thus exhibiting much tighter input cou-

pling which results in input sensitivities on the order of $1/M_{in} = 0.1 - 5\,\mu\text{A}$ [Mag13b, Sta17a, Supb, Qua]. Hence, they can show equivalent current noise values $S_i^{1/2}$ as nano-sized SQUIDs, however with much less restrictions on the equivalent flux noise density $S_\Phi^{1/2}$. Those devices show equivalent flux noise densities $S_\Phi^{1/2} = 1 - 5\,\mu\Phi_0/\sqrt{\text{Hz}}$, therefore a micro-sized SQUID approach is more favorable. Fig. 4.15 illustrates this situation. It shows the current noise density $S_i^{1/2}$ vs. input sensitivity $1/M_{in}$ for various equivalent flux noise densities $S_\Phi^{1/2}$.

To summarize, a low yield rate was received, i.e. no fully functioning SQUID-triple was found among all tested chips. Thus crosstalk between the individual SQUIDs could not be evaluated. Additionally not a single Q spoiler passed current. This is an intelligible behaviour. Due to the fact, that the resistance of each individual Q spoiler SQUID is usually below $1\,\Omega$, a large array (here: 64 SQUIDs in series) is necessary to damp out the induced current. Since the Q spoiler approach relied on laterally very small junctions $d_{\text{JJ}} = 100\,\text{nm}$, it renders them very susceptible to defects. Therefore the probability to have a functioning Q spoiler is reduced drastically. Since the Q spoiler is essential for the operation of the SCS, the devices can not be used in a real NMR setup.
The PTB also has the capability to fabricate devices in a SIS process. The devices discussed in the subsequent chapter are based on this process.

4.3. Second Generation of Multi-SQUIDs: SIS based devices

4.3.1. First SIS fabrication run

The second generation of the multi-SQUID design was planned and laid out for PTB's SIS process described in 3.1, with a critical current density $j_{c,SIS} = 1000\,A/cm^2$. Fig. 4.16 shows the schematic diagram of the layout

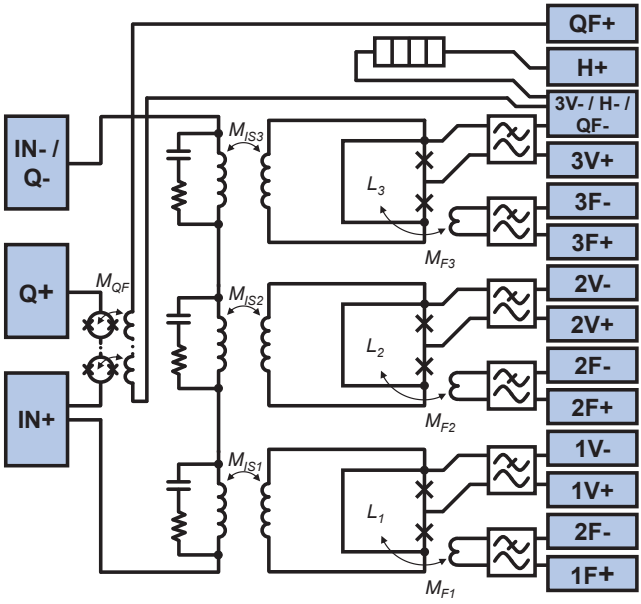

Figure 4.16.: Schematic multi-SQUID current sensor layout for SIS based devices.

Apart from small layout improvements the principal design is, for the SIS process, an adapted version of the one presented in chapter 4.2. The most prominent change is the reworked SQUID cell. Again, the SQUID was designed in a first-order series gradiometric layout with a line width $l_{SQ} = 2\,\mu m$. The SQUID inductance has been enlarged quite drastically compared to the SNS approach. The SQUIDs now have the inductances

$L = 80\,\mathrm{pH}, 105\,\mathrm{pH}, 140\,\mathrm{pH}$. With a lateral JJ size of $d_{\mathrm{JJ}} = 1.1\,\mu\mathrm{m}$ the critical current of a single JJ is $I_0 = 12.1\,\mu\mathrm{A}$. This yields screening parameters $\beta_L = 0.85, 1.25, 1.65$. Each JJ is resistively shunted with $R_{\mathrm{JJ}} = 18\,\Omega$ which yields $\beta_C = 0.7$ and $R_n = 9\,\Omega$.

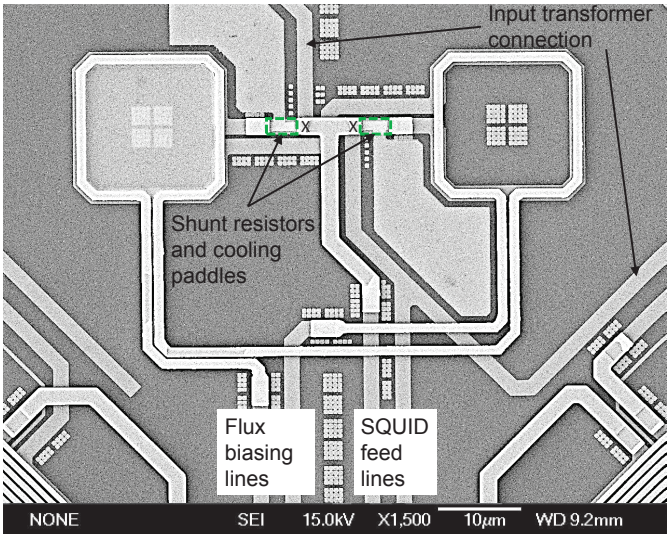

Figure 4.17.: SQUID cell of the 1. SIS run. The JJs are indicated by the ×-symbol while the shunt resistors are indicated by the dashed green lines, respectively. Additionally, the left SQUID loop and parts of the feedback coils lines are covered with a AuPd layer because the lift-off process was not completely successful across the wafer.

The flux biasing of the individual SQUIDs is now achieved by a coil coupling flux directly to the SQUID inductance (cf. Fig. 4.17). On the one hand, this improves $1/M_F$. Depending on L, the expected values are $1/M_F = 34\,\mu\mathrm{A}/\Phi_0, 23.5\,\mu\mathrm{A}/\Phi_0, 18\,\mu\mathrm{A}/\Phi_0$ for $L = 80\,\mathrm{pH}, 105\,\mathrm{pH}, 140\,\mathrm{pH}$, respectively. On the other hand, possible crosstalk between the individual SQUIDs is minimized since feedback signals are no longer coupled into the flux transformer directly. The next design change worth mentioning is that only two different input inductances have been implemented. Total input inductances $L_{\mathrm{in}} \approx 900\,\mathrm{nH}$ (26 turns/transformer washer) and $L_{\mathrm{in}} \approx 1500\,\mathrm{nH}$ (35 turns/transformer washer) where chosen since such in-

ductance values allowing for good matching of L_{in} to the various different pickup coils that have been wound for testing purposes. The washer inductance $L_W \approx 100\,\text{pH}$ was kept approximately the same for both L_{in}. Fig. 4.17 shows the SQUID cell. The JJs are indicated by the $\times$-symbol. The AuPd shunt resistors are patterned directly on top of the bottom Nb layer (separated by a SiO_2 layer) to minimize the influence of the shunt inductances affecting the SQUID dynamics [Rud12]. Additionally, the shunt resistors are equipped with cooling paddles. This feature was implemented precautionary, just in case the sensors will be used in different projects subjected to milli Kelvin (mK) temperatures.

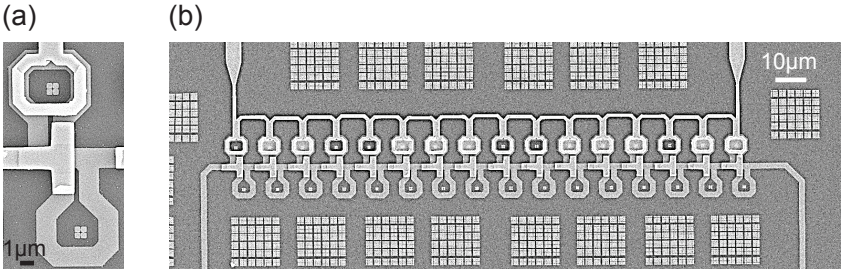

Figure 4.18.: (a) Close-up SEM image of one single Q spoiler SQUID. It can be seen that the feedback coil of the Q spoiler is shorted. (b) Overview SEM image of the complete Q spoiler. The blocks surrounding the Q spoiler are CMP support structures mandatory for the fabrication process (cf. chapter 3.1).

The new Q spoiler implementation is depicted in Fig. 4.18. Figure 4.18(a) shows a close-up of a single SQUID, while Fig. 4.18(b) shows the whole array forming the Q spoiler, respectively. It has been realized by means of a series array of 16 identical unshunted SQUIDs in series to the input coil. The individual SQUIDs are layed out in a series gradiometric configuration to make them insensitive to homogeneous magnetic offset fields. Each SQUID has an inductance $L_{QSS} = 18\,\text{pH}$ and a critical current $I_c = 72\,\mu\text{A}$, yielding $\beta_L = 0.63$. This allows for a critical current modulation $\Delta I_c / I_{c,max} \approx 0.6$ (cf. Fig. 3.3), resulting in a minimum critical current $I_{c,QS}(\text{on}) = 28.5\,\mu\text{A}$ once the Q spoiler is turned on (i.e. applied flux $\Phi_a \approx 0.5\Phi_0$). To simplify the Q spoiler layout the flux modulation coil is placed only on one of the two SQUID loops. Due to the unshunted

Table 4.1.: Summary of the designed Q spoiler parameters

Number of SQUIDs	16
L (pH)	18
I_0 (μA)	36
β_L	0.63
$I_{c,QS}$(off/on) (μA)	72/28.5
I_r (μA)	≈ 1

design, the Q spoiler is highly hysteretic and exhibits a very low return current $I_r \approx 1\,\mu$A when returning to the zero voltage state after it was transitioned into the resistive state by a RF pulse. This is advantageous because this ensures that after a NMR pulse the parasitically induced current has to decay to I_r first before the desired signal is passed to the input coil. Table 4.1 summarizes the Q spoiler parameters.

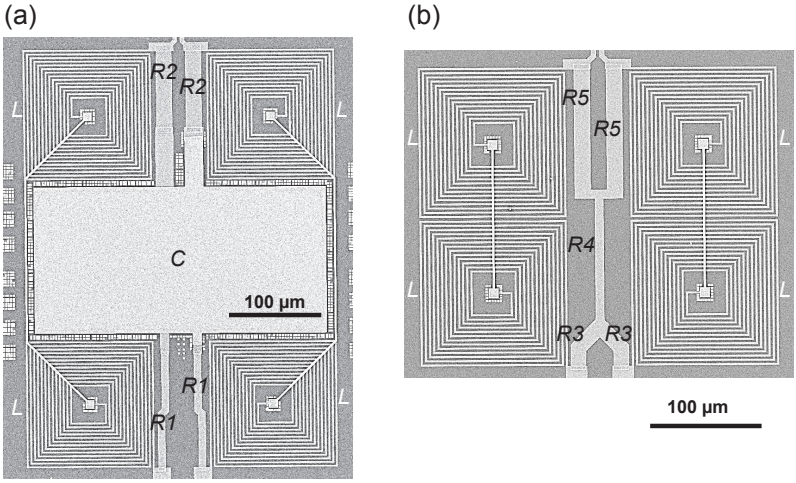

Figure 4.19.: (a) SEM image of the on-chip RF filter for the SQUID and (b) for the modulation coil feed lines, respectively.

Figure 4.19 shows SEM images of the filter implementation. The SQUID feed line filter can be seen in (a) while the modulation coil feed line filter

is shown in (b), respectively. Compared to the implementation in the SNS process, their layout has been changed to demand less chip area. Additionally the resistor lines have been widened to min. 8 μm so that possible edge defects of the deposited resistors don't affect the resistor values and thus the filter performance.

Table 4.2 summarizes the SQUID parameters.

Table 4.2.: Summary of the designed SQUID parameters

L (pH)	80/105/140
I_0 (μA)	12.1
R_{JJ} (Ω)	18
β_L	0.85/1.25/1.65
β_C	0.7
L_{in} (nH)	900/1500
R_H (Ω)	300
Feedback scheme	FLL

4.3.2. Transport measurements

Already during the first characterization measurements various problems of the fabrication run could be identified (e.g. see Fig. 4.20). By measuring 20 devices that were homogeneously spread among the wafer the following parameters have been obtained. Representative for all SQUIDs of this fabrication run, the SQUID C4_E2 will be presented (design values: $\beta_L = 1.25$, $1/M_{FB} = 23.5\,\mu\mathrm{A}/\Phi_0$). Fig. 4.20 shows the corresponding $I(V)$ curve and it reveals three problems which will be explained subsequently.

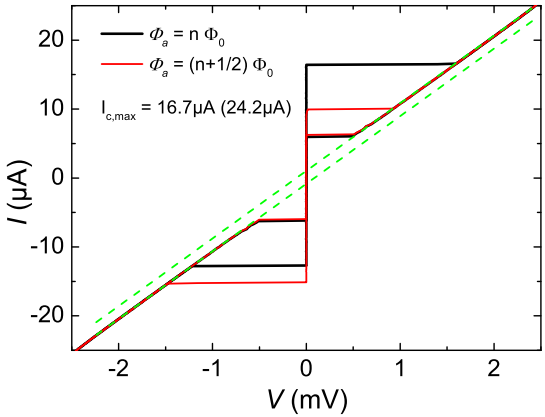

Figure 4.20.: $I(V)$ curve of the device C4_E2, exemplarily for the 1. SIS fabrication run. The device shows a large hysteresis caused by a erroneous shunt resistor layout. Additionally, the run suffers from a too low critical current density

The first problem is, that the SQUID shows a large hysteresis and the damping parameter is $\beta_C \approx 12$, while the design value is $\beta_{C,\mathrm{design}} = 0.7$. This is caused by drastically too large shunt resistors. While $R_{n,\mathrm{design}} = 9\,\Omega$, the values of R_n for all measured devices vary between $R_n = 32.5 - 99.8\,\Omega$ ($R_{n,\mathrm{C4\_E2}} = 99.8\,\Omega$). It is not caused by a fabrication problem, but it can be attributed to a design error and, thus, is caused by the layout of the SQUID cell. Due to the attempt of implementing the shunt resistors with the lowest possible parasitic inductance, they where patterned directly

on top of the top and bottom Nb layer, respectively. However, since the top Nb layer was implemented with an extraordinary large thickness of $h_{\mathrm{Nb,top}} = 750\,\mathrm{nm}$ (cf. chapter 3.1), a large step is introduced into the shunt resistor layout. The deposition of the shunt resistors therefore is very inhomogeneous at the steep step and even holes in the layer can be observed (cf. Fig. 4.21). Hence, a consistent layer thickness is not guaranteed which leads to the observed variations.

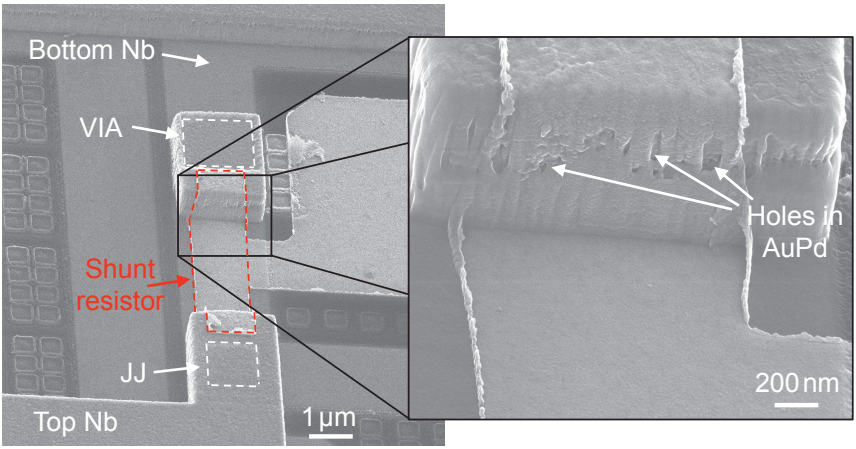

Figure 4.21.: SEM image of a shunt resistor. Clearly the large step due to the thick top Nb layer and the undefined width of the shunt resistor layer at the steep can be seen. The zoomed section on the right shows a detailed view of the holes in the vertical part of the shunt resistor.

The second problem relates to the critical current $I_{c,max}$ of the device. The obtained $I_{c,max} = 16.7\,\mu\mathrm{A}$ is 30% smaller than the design value of $I_{c,\mathrm{design}} = 24.4\,\mu\mathrm{A}$ and corresponds to a critical current density $j_c = 690\,\mathrm{A/cm^2}$. The current density throughout the wafer varied between $j_c = 260 - 713\,\mathrm{A/cm^2}$ (design value: $j_c = 1000\,\mathrm{A/cm^2}$). The reason for this is not caused by a layout flaw but has to be attributed to the fabrication process, maybe caused by a parameter drift of the Al deposition or the barrier oxidation. The yielded feedback sensitivity $1/M_{FB} = 26.6\,\mu\mathrm{A}$ is close to the design value of $1/M_{FB,\mathrm{design}} = 23.5\,\mu\mathrm{A}$. The third problem is

indicated by the two dashed green lines in Fig. 4.20. For a fully operable device, there should be no offset between the two lines and they should coincide perfectly. The observed offset, however, is reported in literature to be caused by superconducting micro-shorts between the top and the bottom Nb layers [RKLG92].

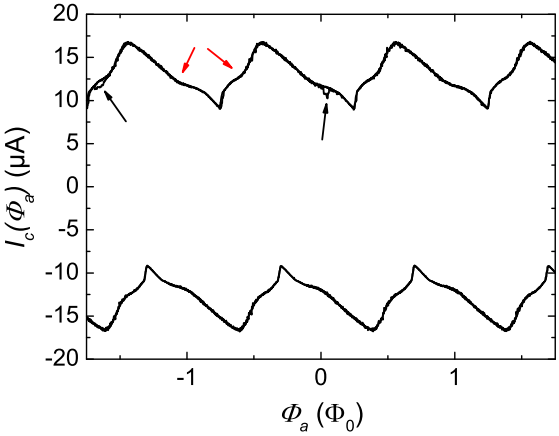

Figure 4.22.: $I_c(\Phi_a)$ of the SCS showing noisy features, which are most likely related to the layer insulation problem (black arrows). Additionally, indentations can be seen which could not be reproduced by numerical simulations (red arrows).

Noisy features in the $I_c(\Phi_a)$ and $I_c(I_{\text{in}})$ curve seem to support the micro-short assumption because their appearance seems to correlate with the overlapping area of top and bottom Nb layers. On the $I_c(\Phi_a)$ curve (cf. Fig. 4.22), where there is only a small overlap of top and bottom Nb due to the feedback coil (top Nb) patterned directly on top of the SQUID loops (bottom Nb), there are only a few noisy features. Additionally, the shape of the $I_c(\Phi_a)$ exhibits an indentation at $\approx \pm 0.5\,\Phi_0$. Its origin is most likely related to a combination of asymmetries in current α_I between the two JJs and in the inductance between the loops α_L since in the static, voltage free case only those two asymmetries show an effect. However it was not possible to reproduce the shape of the curves using numerical simulations. To obtain the $I_c(I_{\text{in}})$ curve, the whole input circuit, consisting of large

top/bottom Nb overlaps due to the input coils, is involved. The resulting curve is extremely noisy (cf. Fig. 4.23). The same effect was observed for all other investigated devices.

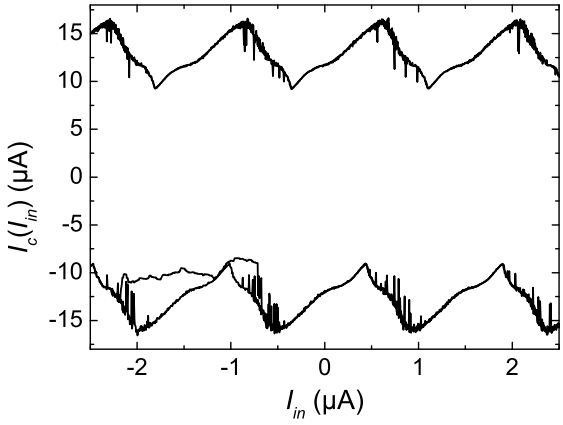

Figure 4.23.: Critical current vs. input current of the sensor C4_E2.

Furthermore, both the $I_c(\Phi_a)$- and $I_c(I_{\mathrm{in}})$ curves exhibit indentations the origin of which is unclear (marked by black arrows). The feature could not be reproduced by numerical simulations, however since several problems have been identified, a detailed analysis is not possible at this point. It is worth mentioning though, that the input sensitivity $1/M_{in}$ is drastically improved, an average value of $1/M_{in} = 1.46\,\mu\mathrm{A}/\Phi_0$ was obtained, which is an improvement of $1/M_{in}$ by a factor 25 as compared to the SNS process. This value is competitive to $1/M_{in}$ of commercial SCSs and is justifying the decision of changing the fabrication technology.

Fig 4.24 shows the corresponding $V(\Phi_a)$ curves of the device. Due to the strongly hysteretic behavior no possible working point for the characterization of $S_\Phi^{1/2}$ could be found, the device is switching digitally between the superconducting state and the overcritical voltage state only.

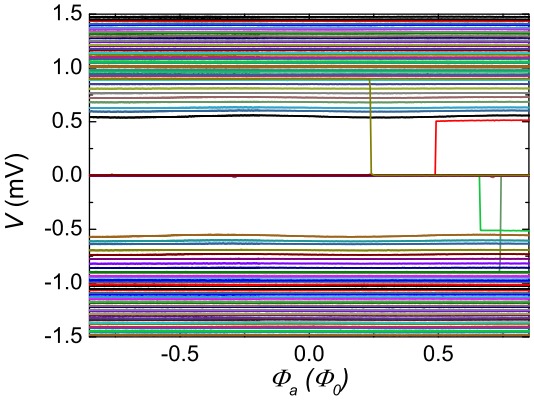

Figure 4.24.: $V(\Phi_a)$ of the device C4_E2 for bias currents ranging from $I_B = -15... + 15\,\mu$A in $0.5\,\mu$A steps. The device switches only digitally between the superconducting state and the overcritical voltage state.

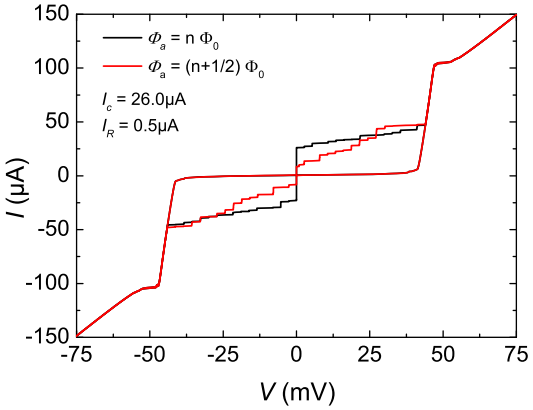

Figure 4.25.: $I(V)$ curve of a Q spoiler exhibits the intended hysteretic behavior with a very low return current $I_r = 0.50\,\mu$A, but also a step-like behavior caused by different critical currents of the individual SQUIDs.

The Q spoilers show the same problems as described above for the SQUIDs. Figure 4.25 shows the $I(V)$ curve of one device. The curve exhibits exactly 16 steps which coincides with the number of SQUIDs in the array, indicating that the individual array SQUIDs all have different critical currents. For $\Phi_a = n\,\Phi_0$, the first SQUID of the array that becomes resistive has a critical current $I_{c,\mathrm{first}} = 26\,\mu\mathrm{A}$, while the last step (thus the last of the 16 SQUIDs becomes resistive) occurs at $I_{c,\mathrm{last}} = 48\,\mu\mathrm{A}$. Once completely resistive, the array shows a very high resistance $R_n = 505\,\Omega$ while the sub-gap resistance $R_{sg} = 23.25\,\mathrm{k}\Omega$. To return from the resistive state back to the zero-voltage state, the current in the Q spoiler has to drop below the very low return current $I_r = 0.50\,\mu\mathrm{A}$.

The $I_c(\Phi_a)$ curve (cf. Fig. 4.26) shows a very large $1/M_\mathrm{F} \approx 10\,\mathrm{mA}/\Phi_0$ which is caused by the shorted feedback coil (cf. Fig. 4.18). Additionally the curve is extremely noisy and the Q spoiler jumps randomly between the resistive and zero-voltage state which is most likely also caused by the insulation problem.

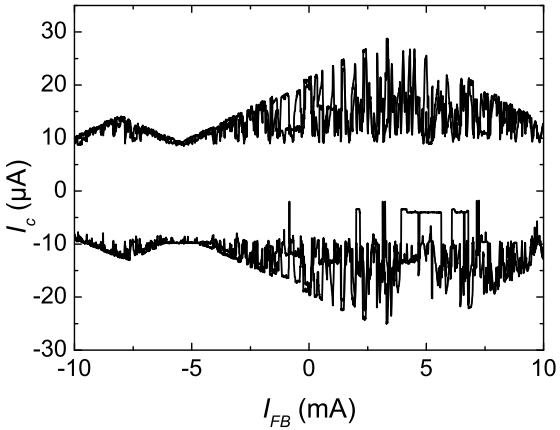

Figure 4.26.: Corresponding $I_c(\Phi_a)$ curve of the same Q spoiler device.

In conclusion, moving away from the SNS to the SIS process seem to be a successful step towards useful SCSs. Even though the noise performance could not be evaluated due to the hysteresis in the $I(V)$ curves of all devices,

the other important quantity, i.e. input coupling $1/M_{\mathrm{in}}$, could be improved by a factor $\approx$ 25. Also, the feedback coupling $1/M_{\mathrm{F}}$ was improved by a factor $\approx$ 10 which allows for convenient operation of the devices employing the Magnicon XXF-1 electronics.

4.3.3. Second SIS fabrication run

For the design of the second run the findings of the first SIS run where taken into account. The first change addresses the shunt resistor layout, which has been reworked. The resistor is now placed next to the bottom Nb layer (cf. Fig. 4.27). A VIA connects the top Nb layer with a small Nb isle in the bottom layer. The shunt resistor now can easily be implemented on the level of the bottom Nb layer, hence getting rid of the huge step. The shunt resistor is connected to both the Nb isle and the bottom Nb layer by VIAs to ensure good electrical connection.

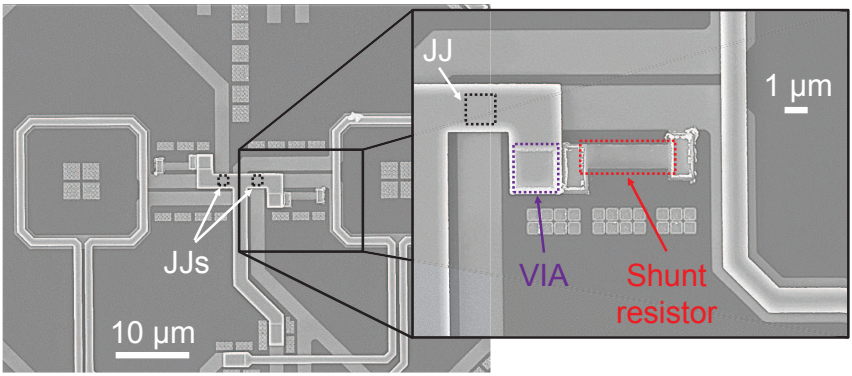

Figure 4.27.: Shunt resistor fix of the second SIS run. The resistor is placed next to the bottom Nb layer and is connected to the top layer via a VIA.

The second change addresses the variation of the critical current density j_c. To be able to compensate for j_c variations, SQUIDs with both smaller ($l_{\mathrm{JJ}} = 0.95\,\mu\mathrm{m}$) and larger JJs ($l_{\mathrm{JJ}} = 1.25\,\mu\mathrm{m}$), compared to the already used $l_{\mathrm{JJ}} = 1.1\,\mu\mathrm{m}$, have been implemented (these junctions are referred to as backup junctions). As a consequence, variations in the SQUID inductance and thus β_L had to be dropped due to limited wafer area. Only one

SQUID inductance $L = 80\,\mathrm{pH}$ was implemented, leading to $\beta_L = 0.85$. The last modification addresses the Q spoiler. Here the layout of the feedback coil was reworked to minimize the parasitic inductance. Additionally, the line width of the feedback coil w_{FB} was reduced to $w_{FB} = 500\,\mathrm{nm}$.

4.3.4. Transport measurements

Due to the fact, that all investigated devices exhibit the same behavior qualitatively, again only one device will be presented. The device B1_5_2 features JJs with $l_{\mathrm{JJ}} = 1.25\,\mu\mathrm{m}$, which yields, in combination with the designed critical current density $j_c = 1000\,\mathrm{A/cm^2}$, $I_0 = 15.6\,\mu\mathrm{A}$ and $I_c \approx 31\,\mu\mathrm{A}$. Figure 4.28 shows the $I(V)$ curve of B1_5_2.

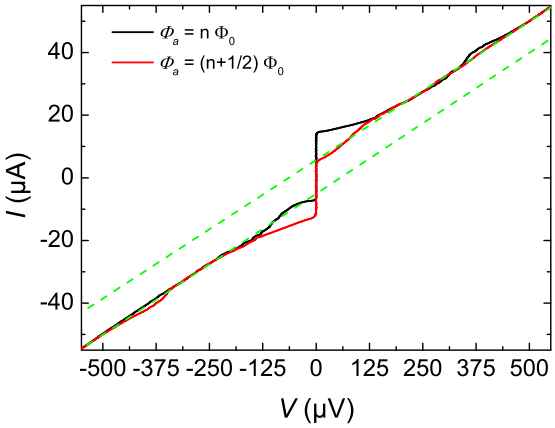

Figure 4.28.: $I(V)$ curve of the second SIS run (sample B1_5_2). Compared to the first current sensor SIS run, the layer insulation problem has become even more severe as can be seen by the increased offset between the two dashed green lines.

As can be seen by the offset of the two dashed green lines, the micro-short problem is still present. In this run, its effect is even more pronounced. Additionally, the critical current $I_c = 14.7\,\mu\mathrm{A}$ is not even half of the design value and corresponds to $j_c = 458\,\mathrm{A/cm^2}$ (throughout the wafer it was

found that $j_c = (636 \pm 146)\,\mathrm{A/cm^2}$). If, however, j_c is not determined from $I(V)$ or $I_c(\Phi_a)$ curves but by measuring dedicated test structures (i.e. single unshunted JJs, where the overlap between top and bottom Nb is given by the JJ area only), $j_c = 980 - 1050\,\mathrm{A/cm^2}$ is found. This is practically the desired j_c value. Hence, the drastic deviations of j_c in complex circuits can be attributed to a severe isolation problem of the two Nb layers. Fig. 4.29 shows an optical interference contrast micrograph of the CMP processed SiO_2 layer of test structures without the Nb deposited atop to investigate the isolation problem. Clearly visible are black dots on the white background. Each black dot refers to a pinhole in the SiO_2 layer. After deposition of the top Nb layer, those pinholes form the micro-shorts mentioned above. Each pinhole has a typical diameter of $\leq 1\,\mu$m. To make them visible on a micrograph, they have been widened artificially to a diameter of $\approx 10\,\mu$m by means of intensive overetching and anodization.

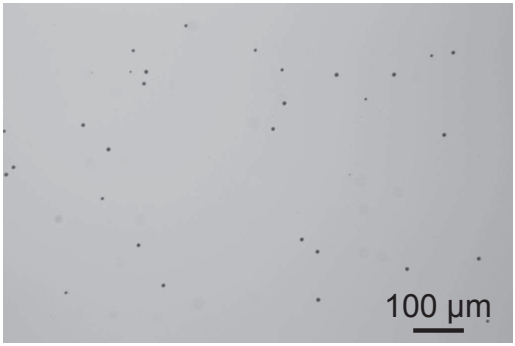

Figure 4.29.: Micrograph of the SiO_2 insulation layer of fabricated test structures. Each black dot refers to a pinhole in the SiO_2 layer. They have a typical diameter of $\leq 1\,\mu$m (widened to $\approx 10\,\mu$m to become clearly visible on the micrograph.

O. Kieler was able to track down the origin of the pinholes to a contaminated CMP process. During the CMP process, contaminant particles are getting pressed and rubbed into the SiO_2 insulation layer. After the successive Ar plasma cleaning treatment the contaminants are removed and pinholes in the insulation barrier remain.

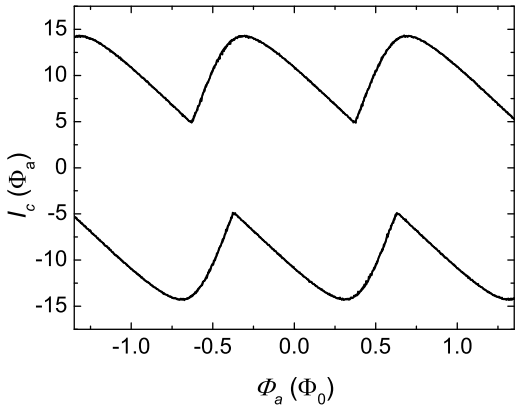

Figure 4.30.: The $I_c(\Phi_a)$ curves of the second SIS run shows a very smooth behavior. The asymmetry of the curves with respect to the flux axis is caused by an inductance asymmetry.

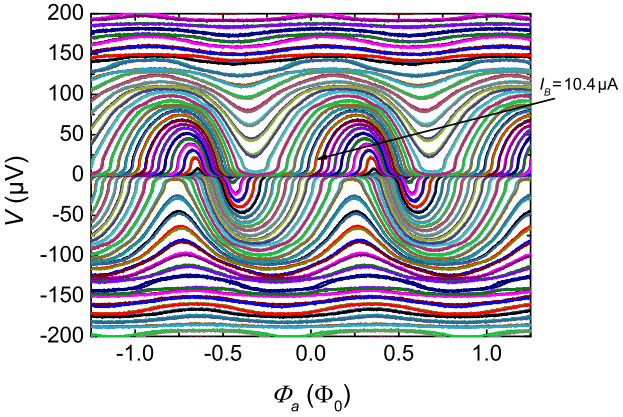

Figure 4.31.: $V(\Phi_a)$ characteristics of the device B1_5_2 for bias currents ranging from $I_B = -25... + 25\,\mu$A in $\approx 0.5\,\mu$A steps. The maximum transfer coefficient V_Φ was found to be $V_\Phi = 780\,\mu\text{V}/\Phi_0$ at $I_B = 10.4\,\mu$A.

The $I_c(\Phi_a)$ curve (cf. Fig. 4.30) in this run, in contrast to $I_c(\Phi_a)$ curves of the first run, don't show the indentations but perfectly smooth behavior. The feedback coupling $1/M_{FB} = 37.0\,\mu\mathrm{A}/\Phi_0$ is close to the expected value of $34.0\,\mu\mathrm{A}/\Phi_0$. Due to the asymmetric bias feed lines, an inductance asymmetry parameter $\alpha_L = 0.55$ was found. Fig. 4.31 shows the $V(\Phi_a)$ characteristics. For all used bias currents I_B, the SQUID shows smooth curves. The maximum transfer coefficient V_Φ was found to be $V_\Phi = 780\,\mu\mathrm{V}/\Phi_0$ at $I_B = 10.4\,\mu\mathrm{A}$.

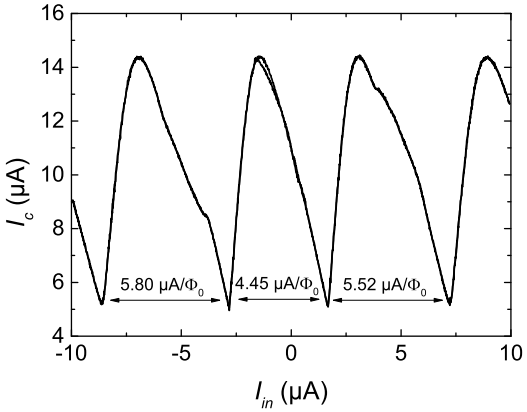

Figure 4.32.: The $I_c(I_{\mathrm{in}})$ curve of the second SIS run based SCS shows variable values for $1/M_{\mathrm{in}}$, which varies between $1/M_{\mathrm{in}} = 4.45 - 5.80\,\mu\mathrm{A}$ in the presented section of the $I_c(I_{\mathrm{in}})$ curve.

The $I_c(I_{\mathrm{in}})$, in contrast to the $I_c(\Phi_a)$ curve, again shows the indentations of the curves (cf. Fig. 4.32). In addition, $1/M_{\mathrm{in}}$ is not a constant value. The minimum value for the device B1_5_2 is $1/M_{\mathrm{in}} \approx 4.45\,\mu\mathrm{A}$ and it increases for increasing I_{in}. The values for the other measured devices varied between $1/M_{\mathrm{in}} = 2.5{-}9\,\mu\mathrm{A}$. Again, there was no systematic behavior in the yielded values, e.g. devices with input inductances $L_{\mathrm{in}} = 1500\,\mathrm{nH}$ showed larger $1/M_{\mathrm{in}}$ values than devices with $L_{\mathrm{in}} = 900\,\mathrm{nH}$. The reason for the input current dependent $1/M_{\mathrm{in}}$ is not clear. A possible explanation is based on the micro-shorts between the top and bottom Nb electrodes. Presumably, direct current channels between both electrodes branch off

current which is intended to flow through the input coil, effectively forming a current devider.

4.3.5. Noise characteristics

The noise of the device has been determined by the methods explained in chapter A.2. The SQUID was biased at its optimum working point $I_B = 10.4\,\mu\text{A}$ and $\Phi_B = 0.06\,\Phi_0$. The $S_\Phi^{1/2}$ spectrum has a frequency resolution $\Delta f = 0.1\,\text{Hz}$ and was averaged for $n_{\text{avg}} = 100$ times.

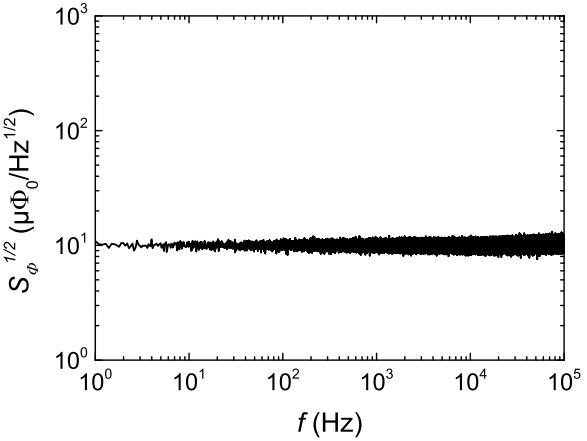

Figure 4.33.: Equivalent flux noise density spectrum of device B1_5_2.

The shape of the spectrum is quite uncommon, e.g. there are no indications for low frequency $1/f$ noise at all. This was observed for most of the measured devices of this run (SQUIDs for a different project but from the same wafer showed a $1/f$ corner frequency between $10 - 20\,\text{Hz}$). The level of the white noise is $S_\Phi^{1/2} = 10\,\mu\Phi_0/\text{Hz}^{1/2}$. Biasing the SQUIDs at various different bias currents and flux points showed the same spectral shape. Using the minimum value for $1/M_{\text{in}} \approx 4.5\,\mu\text{A}$ and the yielded $S_\Phi^{1/2} = 10\,\mu\Phi_0/\text{Hz}^{1/2}$, one finds an input noise current $S_i^{1/2} = 45\,\text{pA}/\text{Hz}^{1/2}$ however this estimate is quite meaningless given the described problems of the devices.

4.4. Single SQUID current sensor

The single SCS was introduced in the second SIS fabrication run and is designed to be fully compatible to the existing Magnicon XXF-1 SQUID electronics. It was designed with the idea to have the possibility to increase the field of view of the sensor for possible MRI, fMRI or MEG applications, where the common approach is to implement a multi-channel setup. By placing a number of pickup coils next to each other, spatial information of a larger area can be acquired. Each pickup coil belongs to an individual readout channel, i.e. one pickup coil and one readout SQUID. The common FLL feedback circuit cannot be applied to the SQUIDs in this case. Due to the mutual inductance between the pickup coil L_p and the SQUID, flux feedback to the SQUID would also affect the screening current in L_p.

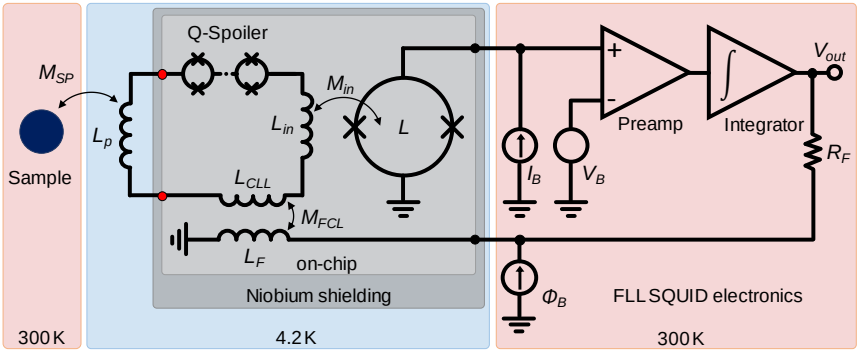

Figure 4.34.: Measurement and feedback scheme of one channel in a single stage CLL configuration. Other channels are omitted for clarity. The flux biasing of the SQUID as well as the CLL feedback are accomplished by the input circuit feedback transformer, consisting of L_F and L_{CLL}. The components inside the blue box are at cryogenic temperatures. Some of them are magnetically shielded by a superconducting niobium shield (grey box). The red dots indicate the superconducting screw terminal to connect L_p to the SCS. The readout electronics (Magnicon XXF-1 [CB04, DHB06, Mag13a]) is at $T = 300\,\mathrm{K}$ and connected to the SQUID via normal conducting copper wires.

This current would create a magnetic field which would be detected by nearby pickup coils from other channels. This signal can not be sep-

arated from signals originating from the NMR experiment. Thus the channel-corresponding electronics would try to feedback the detected signal, which leads to the same effect on the residual channels and induces severe crosstalk and oscillations between all channels. However, this problem can easily be solved by a feedback scheme which keeps the current in the input circuit of one distinct channel constant. Any deviation from the adjusted working point of the SQUID leads to a feedback current, which is fed to a feedback transformer in the input circuit which 'locks' the current in the input circuit to a fixed value (cf. Fig. 4.34, the feedback transformer is formed by L_F and L_{CLL}). Therefore, this feedback scheme is called current locked loop (CLL). Since, in the ideal case, there are no varying currents in the pickup coils and the only magnetic field variation originates from the NMR sample, crosstalk between the channels is suppressed to the greatest possible extent. A schematic overview of the SCS and the physical implementation can be seen in Fig. 4.35(a). The chip is square shaped with a lateral length $l_{w,chip} = 3.2\,\text{mm}$. All the discussed features mentioned above have been implemented and will be explained in detail. The pickup coil L_p is either connected to the pads **In+**/**In-** (no Q spoiler) or to **Q+**/**Q-**, which uses the optional Q spoiler. Any induced current in L_p then couples to the input transformer primary via the mutual inductance M_{TP}, which then couples the signal to the SQUID via M_{TS}. The Q spoiler can be flux biased by a current connected to **QF+**/**QF-**. The SQUID can either be flux biased by a current connected to **F+**/**F-** (for standard FLL operation) or **FCL+**/**FCL-** (for CLL operation).[2]

[2]Flux biasing via **FCL+**/**FCL-** is possible only, if the input circuitry is superconductively shorted via niobium wire-bonding or if a superconducting pickup coil is connected.

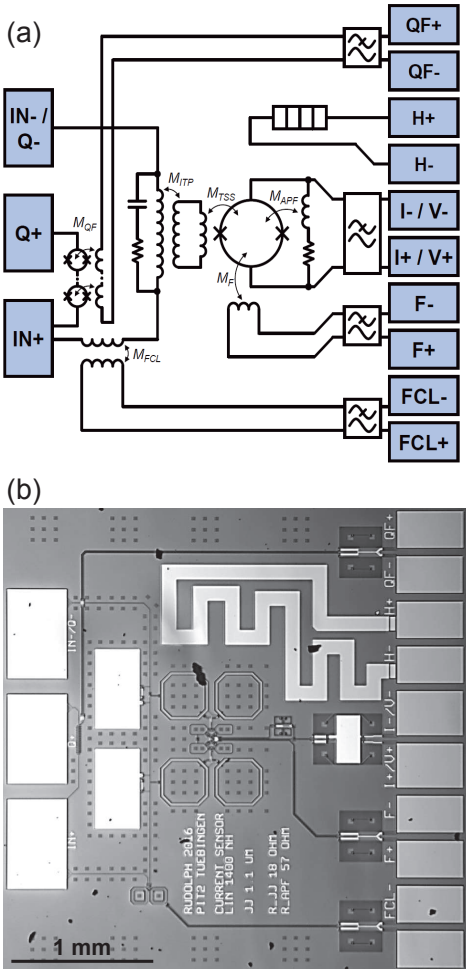

Figure 4.35.: (a) Schematic layout of the current sensor including all implemented features. (b) Micrograph image showing fabricated sensor.

The SQUID has been realized as a second-order parallel gradiometer, consisting of four identical loops (in Fig. 4.36 one SQUID loop is surrounded by a dashed black line), each with a inductance $L_{SQ/4} \approx 300\,\mathrm{pH}$

(resulting in a total geometrical SQUID inductance $\approx 75\,\mathrm{pH}$) and a line width $l_{w,SQ} = 2\,\mu\mathrm{m}$. To increase the transfer function V_Φ for convenient direct readout, additional positive feedback (APF) has been implemented [CB04, Dru16]. The biasing lines of the SQUID are asymmetrically connected to maintain an overall symmetrical layout (cf. Fig. 4.36: one line runs directly towards the JJs, while the second line is connected to the smaller section of input loop 2). This only leads to a small asymmetry α_L in the inductance of the SQUID and therefore to slightly tilted $I_c(\Phi)$ characteristics.

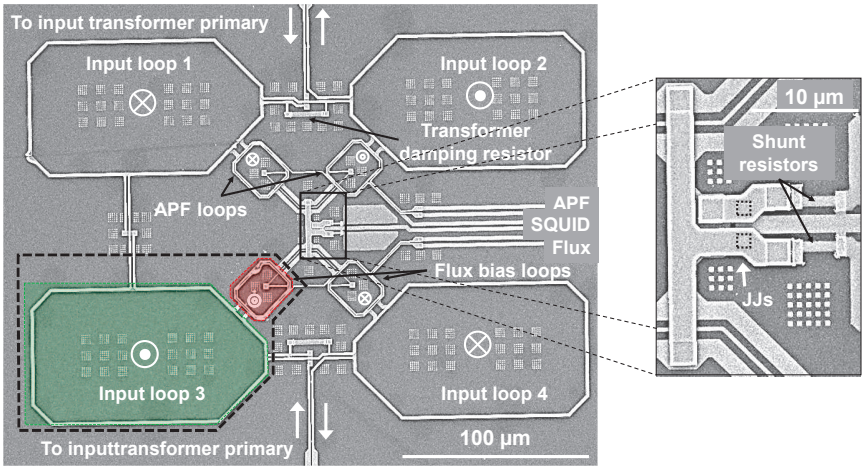

Figure 4.36.: SEM image of the SQUID cell. The SQUID is realized as a second-order parallel gradiometer, consisting of four SQUID loops. The black dashed line highlights one of the four SQUID loops. Each loop is separated into a smaller (red shaded area) and a larger (greed shaded area) section. Two of the small loop sections are used for APF feedback and flux biasing, respectively. All four larger sections are designated for the input signal. The zoomed section gives a detailed view of the JJs and the shunt resistors. Also, the CMP supporting structures (cf. chapter 3.1) can be seen.

The zoomed section in Fig. 4.36 shows the JJs and the shunt resistors as well as the shunt resistor cooling paddles. The JJs are square shaped and have a lateral length $l_{\mathrm{JJ}} = 1.1\,\mu\mathrm{m}$, which, with the given current density $j = 1000\,\mathrm{A/cm^2}$, leads to $I_0 = 12.1\,\mu\mathrm{A}$. Each JJ is shunted with a

resistor $R_{JJ} = 18\,\Omega$. This results in a screening parameter $\beta_L = 0.96$ and, with a junction capacitance $C_{\mathrm{JJ}} \approx 45\,\mathrm{fF}/\mu\mathrm{m}^2$, to a Stewart-McCumber parameter $\beta_C = 0.7$. As in chapter 4.3.3, JJs with both $l_{\mathrm{JJ}} = 1.25\,\mu\mathrm{m}$ and $l_{\mathrm{JJ}} = 0.95\,\mu\mathrm{m}$ have been implemented to compensate for j_c variations.

To minimize the parasitic SQUID area, a very symmetric implementation of the layout was of great importance. Each of the four SQUID loops is separated into a larger and smaller section. The larger section (cf. green shaded area in Fig. 4.36) is dedicated for input coupling and is therefore called input loop. The small section (e.g. red shaded area in Fig. 4.36) is intended for the flux biasing or the APF coil, respectively. This way, the mutual inductance between the flux bias/APF coils and the input coils is low, hence minimizing parasitic coupling [CB04, DAB+07]. The orientation how flux is coupled into each loop, either by the flux biasing/APF coils or the input coils, is indicated by the white circles inside the loops (cf. Fig 4.36).

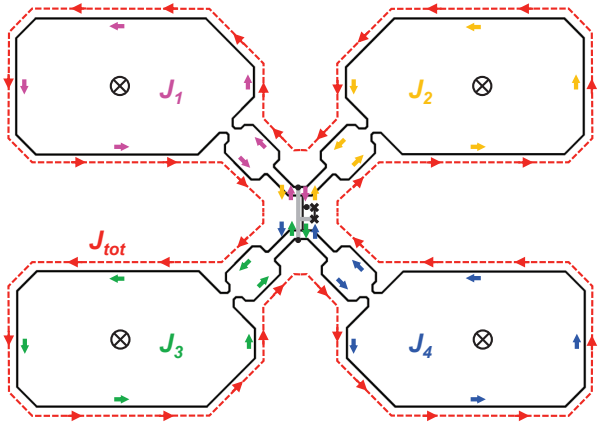

Figure 4.37.: A common mode magnetic field leads to the screening currents $J_1 - J_4$ in the individual four SQUID loops and a resulting screening current J_{tot} of a parallel gradiometer.

A circle with a dot inside couples flux out of the plane of projection while a circle with a cross inside couples flux into the plane of projection. The input coupling transformer's secondary coil is patterned directly on top of the input loops of the SQUID, having a line width $l_{w,TS} = 1\,\mu\mathrm{m}$. The flux bias-

ing is achieved by a coil patterned on top of two of the small sections loop. This coil consists of two windings with a line width $l_{w,FB} = 500\,\text{nm}$ per section. APF is achieved by equally dimensioned coils on the residual small section loops. A drawback of any parallel gradiometer SQUID implementation independent of its gradiometric order, however, is a resulting screening current arising from the flux quantization of each loop. If, for example, the SQUID is exposed to a common mode magnetic field during cool-down (i.e. a magnetic field penetrating each loop equally), which is a valid first approximation for a homogeneous field like the earth magnetic field, each loop will create a circulating current J_n ($n \in [2 \cdot \text{gradiometer order}]$) to obey the flux quantization. No net current is flowing across the JJs since all n currents will cancel out each other. This cancellation however is given only in the region of the JJs, but not in the residual parts of the loops, leading to a large closed superconducting loop . This resulting total shielding current J_{tot} (cf. Fig. 4.37, red dashed line) can, on the one hand, lead to offsets in the characteristic curves of the device due to an imbalance of the gradiometer and therefore an effective parasitic input signal. On the other hand, J_{tot} can become so large, that it creates flux vortices inside of the SQUID structures [Rue08]. Therefore, after the SQUID is cooled down and its niobium shielding has become superconducting, it is advisable to heat the SQUID once above T_c to expel possibly trapped flux and to minimize J_{tot} (cf. 4.37).
Figure 4.38 shows the complete double transformer configuration of the input circuitry. The primary transformer is implemented in a second-order series gradiometer configuration. The input coil is patterned directly on top of the secondary side of the primary transformer with a line width $l_{w,in} = 500\,\text{nm}$. The secondary side of the first transformer is realized by four large washers surrounding the SQUID cell. The first two and the last two of the in series connected input coils share one individual RC shunt (the dashed box in Fig. 4.38 indicates two associated input coils). This is necessary to maintain the damping effect, if low valued source impedances, i.e. low-inductance pickup coils, are connected. For a single RC shunt connected across all four input coils, the damping effect would decrease with the source impedance and even vanish for a shorted input coil [DAB$^+$07, CRD$^+$91].

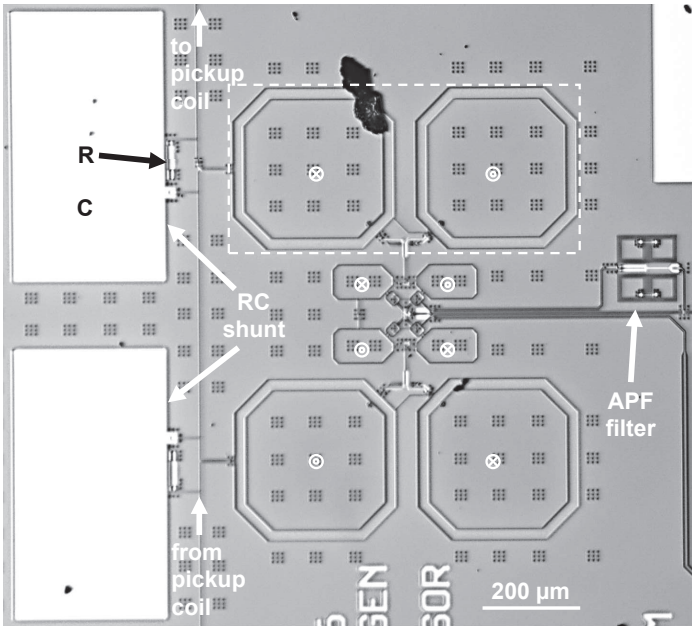

Figure 4.38.: Micrograph of the complete double transformer setup. On the left, the two RC shunts for the input coil are shown. The upper RC shunt is assigned to the two input coils enclosed by the dashed black frame. In the center, the SQUID cell, surrounded by the four input coils connected in a second-order series gradiometric configuration, can be seen. On the right the APF filter is located limiting the feedback bandwidth.

To vary the input coil inductance L_{in} the number of coil turns is altered while the inductance L_{PTS} of the secondary side of the primary transformer is kept almost constant. To cover the inductance ranges of typical pickup coils L_p (as experience teaches $L_p \approx 400 - 1600\,\mathrm{nH}$), two different input coil inductance values L_{in} have been realized: $L_{\mathrm{in}} \approx 700\,\mathrm{nH}$ (15 turns/transformer washer) and $L_{\mathrm{in}} \approx 1400\,\mathrm{nH}$ (22 turns/transformer washer). Figure 4.38 also shows a low pass filter for the APF circuitry. Its purpose is to limit the APF feedback bandwidth, with respect to the characteristic frequency $f_C = V_c/\Phi_0$, to DC frequencies of $\approx 100\,\mathrm{MHz}$. It is also implemented in a X-filter topology however the filter coils have a lower

inductance of $L_{X,AFP} \approx 10\,\mathrm{nH}$ compared to the RF filter coils introduced above.

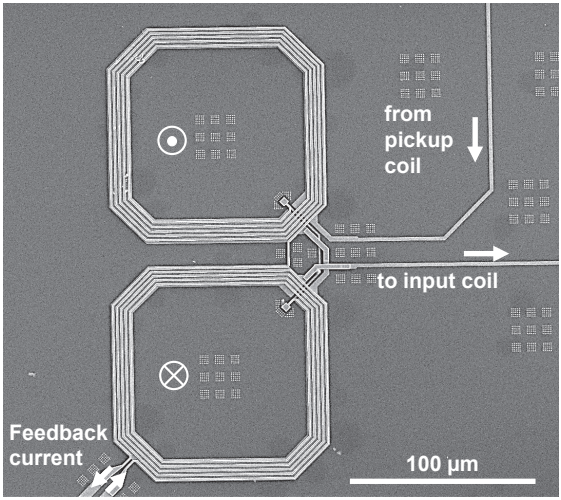

Figure 4.39.: Feedback transformer in series with the pickup and input coils, used to establish a CLL feedback scheme.

The transformer for the CLL feedback scheme is shown in Fig. 4.39. It is implemented in a first-order series washer configuration with the feedback coil patterned directly on top of the two washers which are part of the input circuit.

The Q spoiler as well as the on-chip RF filters are identical to the ones presented in chapter 4.3.3. Also, a heater is implemented as a meander shaped resistor directly on-chip. It has a resistance $R_H = 300\,\Omega$ (cf. Fig. 4.35). With the maximum heater voltage $V_H = 13\,\mathrm{V}$ of the Magnicon XXF-1 readout electronics, this results in a maximum heating power $P_{H,max} = 0.56\,\mathrm{W}$ and a heating power density $\rho_{P,H} = 0.56\,\mathrm{W}/(l^2_{w,chip}) = 0.055\,\mathrm{W/mm^2}$. Table 4.3 summarizes all design parameters of the single SQUID based current sensor.

Table 4.3.: Summary of the designed SQUID parameters

L_{SQUID} (pH)	80
I_0 (μA)	12.1
R_{JJ} (Ω)	18
β_L	0.96
β_C	0.7
L_{in} (nH)	700/1400
R_H (Ω)	300
Feedback scheme	FLL/CLL

4.4.1. Transport measurements

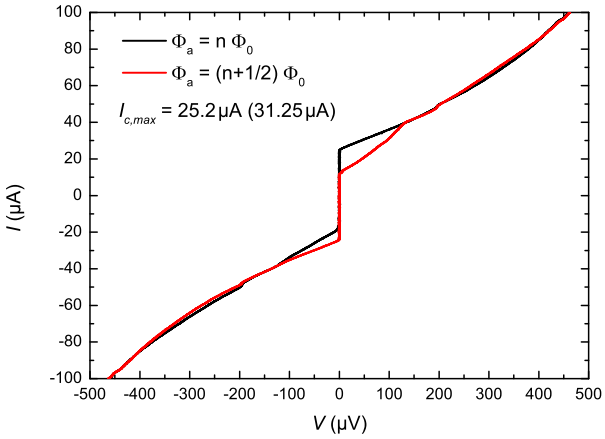

Figure 4.40.: $I(V)$ curve of the single SQUID.

Figure 4.40 shows the $I(V)$ curve of the single SQUID current sensor C2_1. It is equipped with JJs of the size $l_{\text{JJ}} = 1.25\,\mu$m (design critical current $I_{c,\text{design}} = 31.25\,\mu$A). The device shows a measured critical current $I_{c,\text{meas}} = 23.8\,\mu$A, yielding $j_c = 761\,\text{A/cm}^2$. Due to the use of SQUIDs em-

ploying the larger backup JJs and the resulting $I_{c,\mathrm{meas}} \approx I_{c,\mathrm{design}}$, the device should show quite representative results (besides the fact, that β_C is slightly larger than intended due to the larger JJs). The normal conducting resistance $R_n = 8.0\,\Omega$ deviates from the design value $R_{n,\mathrm{design}} = 7.8\,\Omega$ by 2.5 % (given by the parallel connection of R_{SQ} and R_{APF}: $R_{n,\mathrm{design}} = R_{\mathrm{SQ}} \,||\, R_{\mathrm{APF}} = 9\,\Omega \,||\, 59\,\Omega = 7.8\,\Omega$). The slope of the $I(V)$ curve directly after entering the voltage state is decreased compared to SQUIDs seen in chapter 4.3.4 which is caused by the resistive loading of the APF circuitry.

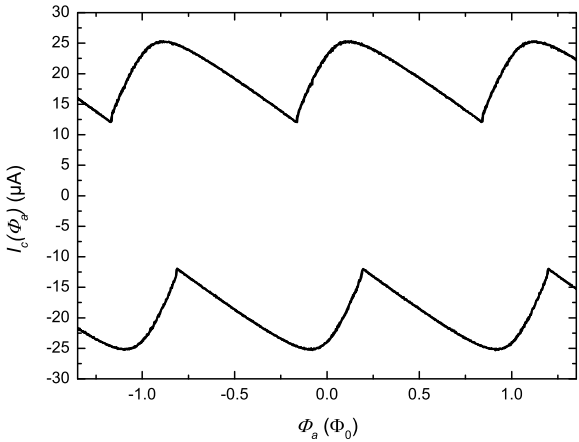

Figure 4.41.: $I_c(\Phi_a)$ of the single SQUID.

Fig. 4.41 shows the corresponding $I_c(\Phi_a)$ curve which has a feedback sensitivity $1/M_F = 55.48\,\mu\mathrm{A}/\Phi_0$ ($51.75\,\mu\mathrm{A}/\Phi_0$) . Besides the asymmetry of the curve caused by the asymmetric biasing scheme no peculiarities like noisy features (due to the layer insulation problem) can be observed. β_L was found to be $\beta_L = 0.82$ (0.85). Fig. 4.42 shows the $V(\Phi_a)$ curves of C2_1. Immediately, a strong tilt in the acquired curves can be observed. It is the result of the APF circuitry. The maximum transfer coefficient V_Φ was found to be $V_\Phi = 805\,\mu\mathrm{V}/\Phi_0$ at $I_B = 13.2\,\mu\mathrm{A}$ ($V_\Phi = 420\,\mu\mathrm{V}/\Phi_0$ on the shallow slope). V_Φ for bias currents $I_B = 10 - 20\,\mu\mathrm{A}$ is almost constant

and permanently above $V_\Phi = 750\,\mu\mathrm{V}/\Phi_0$. This is advantageous because a working point can be chosen such that its linear region is maximized, which lowers the demands for the readout electronics or it increases the feedback stability, respectively.

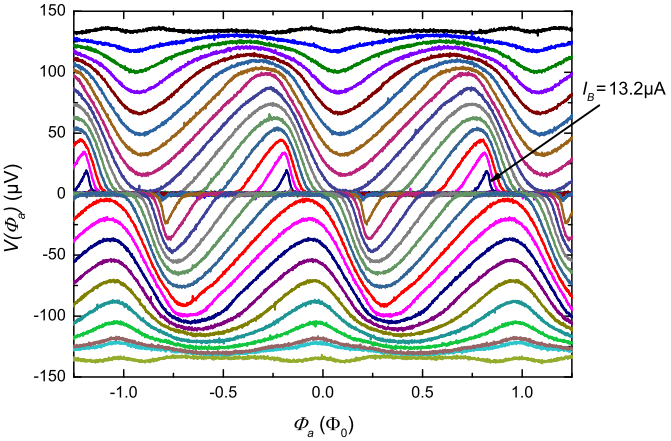

Figure 4.42.: $V(\Phi_a)$ curve of the single SQUID SCS for bias currents ranging from $I_B = -40... + 40\,\mu\mathrm{A}$ in $\approx 1\,\mu\mathrm{A}$ steps. The tilt of the $V(\Phi_a)$ is caused by the APF feedback scheme.

Additionally, no resonance structures can be seen which would deteriorate the performance of the device. This is a clear indication that the employed damping scheme (cf. chapter 3.3.3) to suppress possible resonances works quite well. The $I_c(I_\mathrm{in})$ curve (cf. Fig. 4.43) shows the input coupling performance of the device. The resulting input sensitivity was found to be $1/M_\mathrm{in} = 0.555\,\mu\mathrm{A}/\Phi_0$ (the average value of six measured devices $1/M_\mathrm{in,avg} = (0.579 \pm 0.023)\,\mu\mathrm{A}/\Phi_0$). Fig. 4.44 shows the $I(V)$ curve of the improved implementation of the Q spoiler. As can be seen, most of the array SQUIDs switch to the resistive state at $I_c(\Phi_a = n\Phi_0) \approx 45\,\mu\mathrm{A}$. Once the Q spoiler is activated (i.e. $\Phi_a = n\Phi_0/2$), the critical current is lowered to $I_c(\Phi_a = n\Phi_0) \approx 9\,\mu\mathrm{A}$, which yields $\beta_L = 0.27$.

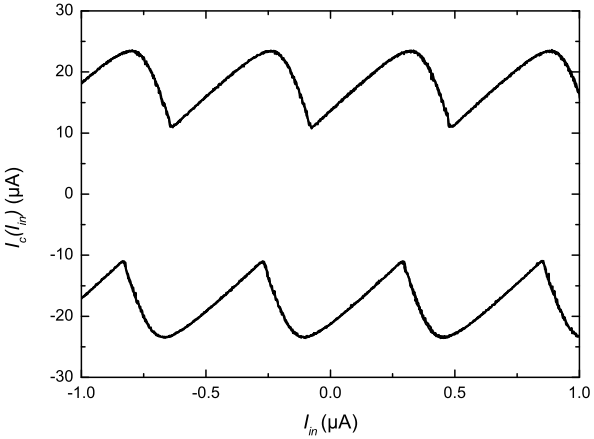

Figure 4.43.: $I_c(I_{\mathrm{in}})$ of the single SQUID SCS.

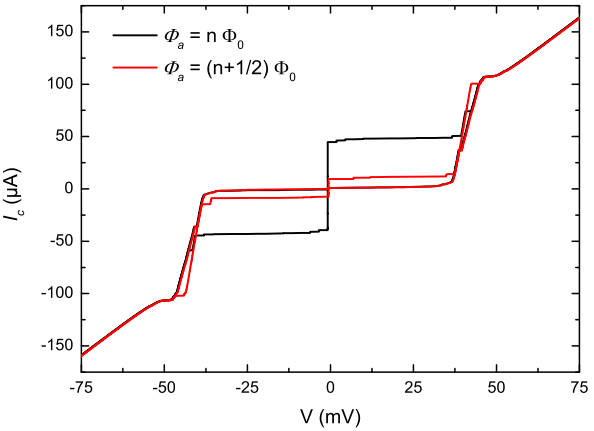

Figure 4.44.: $I(V)$ of the improved Q spoiler implementation.

Its normal conducting state resistance is $R_n = 440\,\Omega$, the sub-gap resistance $R_{\mathrm{sg}} = 21.15\,\mathrm{k}\Omega$ and it exhibits a return current $I_r = 0.7\,\mu\mathrm{A}$. Fig. 4.45 shows the $I_c(\Phi_a)$ characteristics of the Q spoiler.

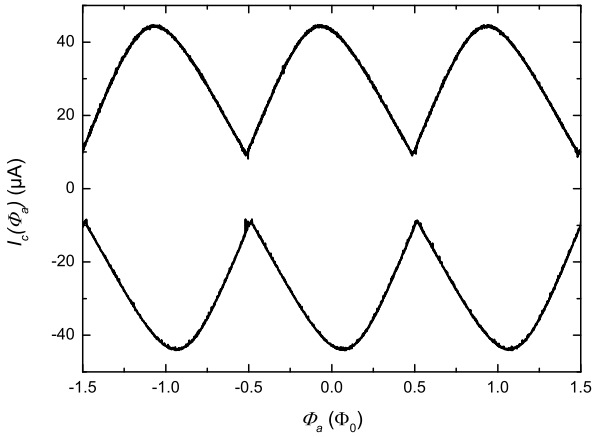

Figure 4.45.: $I_c(\Phi_a)$ of the improved Q spoiler implementation.

The feedback coupling was found to be $1/M_{\mathrm{F,QS}} = 426.4\,\mu\mathrm{A}/\Phi_0$. Additionally, a slight tilt and shift between both curves can be seen. It is caused by the feedback coil of the Q spoiler. Since the coil is only patterned on top of one loop of the Q spoiler, this loop has a slightly smaller inductance due to the screening effect caused by the mutual inductance between the SQUID loop and the feedback coil.

4.4.2. Noise characteristics

Even though the dc characteristics look promising, the noise performance is still quite bad (cf. Fig. 4.46). The SQUID was biased at its optimum working point $I_B = 13.2\,\mu\text{A}$ and $\Phi_B = 0.16\,\Phi_0$. The $S_\Phi^{1/2}$ spectrum of device C2_1 has a frequency resolution $\Delta f = 1\,\text{Hz}$ and was averaged for $n_{\text{avg}} = 100$ times.

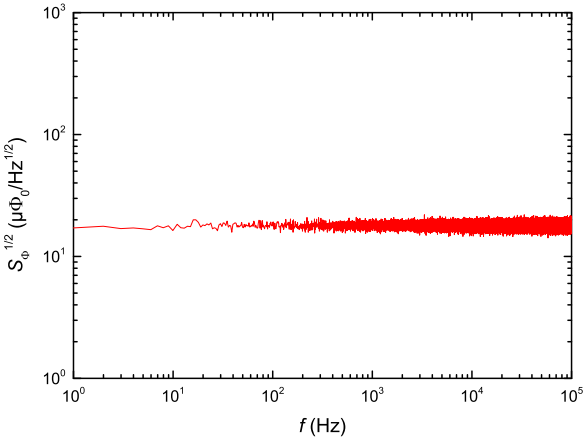

Figure 4.46.: $S_\Phi^{1/2}$ of the single SQUID SCS. As for the other SCS devices based on the SIS process, the noise spectrum does not show any indication of $1/f$ noise and the overall noise level is very high.

As for the device presented in chapter 4.3.4, there are no indications for low frequency $1/f$ noise at all. The level of the white noise is $S_\Phi^{1/2} = 18.3\,\mu\Phi_0/\text{Hz}^{1/2}$. The other investigated single SQUID based current sensors show noise values $S_\Phi^{1/2} = 8 - 40\,\mu\Phi_0/\text{Hz}^{1/2}$. Using $1/M_{\text{in}} \approx 0.555\,\mu\text{A}$ and $S_\Phi^{1/2} = 18.3\,\mu\Phi_0/\text{Hz}^{1/2}$, one finds $S_i^{1/2} = 10.2\,\text{pA}/\text{Hz}^{1/2}$.

Further investigation of the device was not possible. During the cool down in the MPI setup with an input coil connected to the input circuitry to evaluate the feedback coupling of the CLL feedback transformer, the top Nb layer delaminated (the delamination occured on two of three tested

devices). Fig.4.47 shows optical micrographs of the delaminated Q spoiler (a) and the SQUID cell (b).

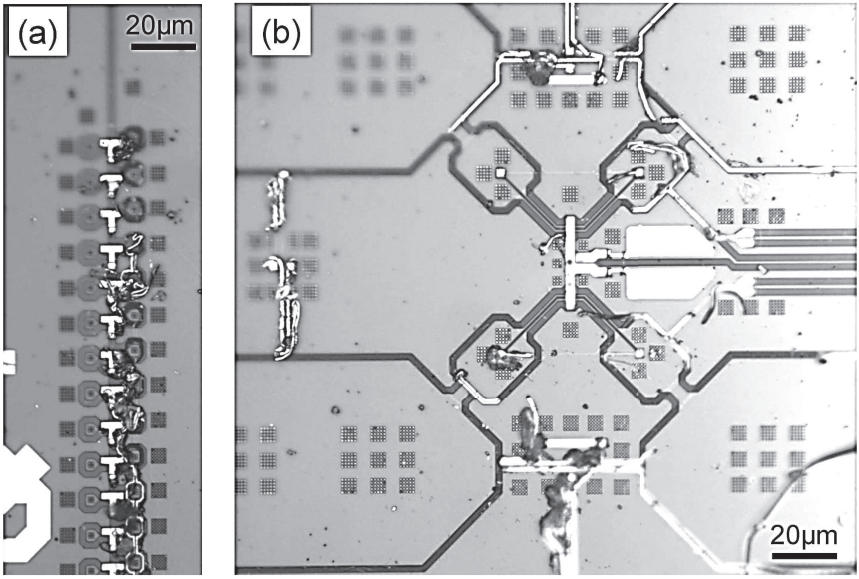

Figure 4.47.: Delamination of the top Nb layer of the Q spoiler (a) and the SQUID cell (b).

4.5. Summary

After the device fabrication process has been described in detail, the SCS designs, that have been realized using two different trilayer approaches, have been presented and where characterized. Unfortunately, both design approaches suffered from a very low yield, which made the evaluation of the design approaches impossible. For the SNS devices, principle drawbacks of the high current density for SCS designs could be shown. The SIS junctions suffered from fabrication-related layer-insulation problems that rendered all devices practically inoperable. Consequently, no optimization of the fabricated devices was possible.

5 | ULF NMR/MRI setup

This section starts with a brief summary of components needed to build a high performance, low noise ULF NMR/MRI setup. After presenting the installed analog-to-digital conversion (ADC)/digital-to-analog conversion (DAC) system, an overview of the employed voltage controlled current sources (VCCSs) will be given. Noise reduction methods like disconnecting the VCCS during measurements, the corresponding relay implementation and feed through filters will be presented. After the coil system has been described in detail, a numerical evaluation of it will be presented. Once the sample container, that houses the sample fluids, is described, the focus is shifted towards the cryogenic components of the system. Starting with the low noise helium dewar, the SQUID based magnetic field sensor followed by the magnetic shielding will be presented and explained. After presenting the magnetic noise floor of the setup, the pH_2 generator is shown. The chapter closes with an overview of the first detection of thermally polarized NMR signals, followed by experiments using hyperpolarization. Except for the design and the implementation of the pH_2 generator as well as the design and built of the current source used for the z-gradient magnetic field, the author was responsible for the design, the realization and the their evaluation/characterization of the needed system components (e.g. the coil system) as well as their acquisition (e.g. the remaining current sources). Figure 5.1 shows a schematic overview that contains all components necessary to perform ULF NMR/MRI experiments. The whole experiment is controlled by the control PC. A variety of self written LabVIEW control software is used to program the NMR/MRI sequences and to manage the data acquisition. The software gives the user extensive freedom by making all relevant parameters like pulse duration, pulse frequency, pulse repetition rate, sampling rate etc. accessible. The employed SQUID electronics

(Magnicon XXF-1, 3 channels), which ultimately controls the SQUIDs, is set up and controlled by the proprietary software SQUID-Viewer (v. 3.3.11) from Magnicon [Mag13a, Mag13b]. Additionally, the SQUID electronics offers the possibility to control, amongst other parameters, for instance the activation of the FLL mode externally by means of transistor-transistor logic (TTL) signals.

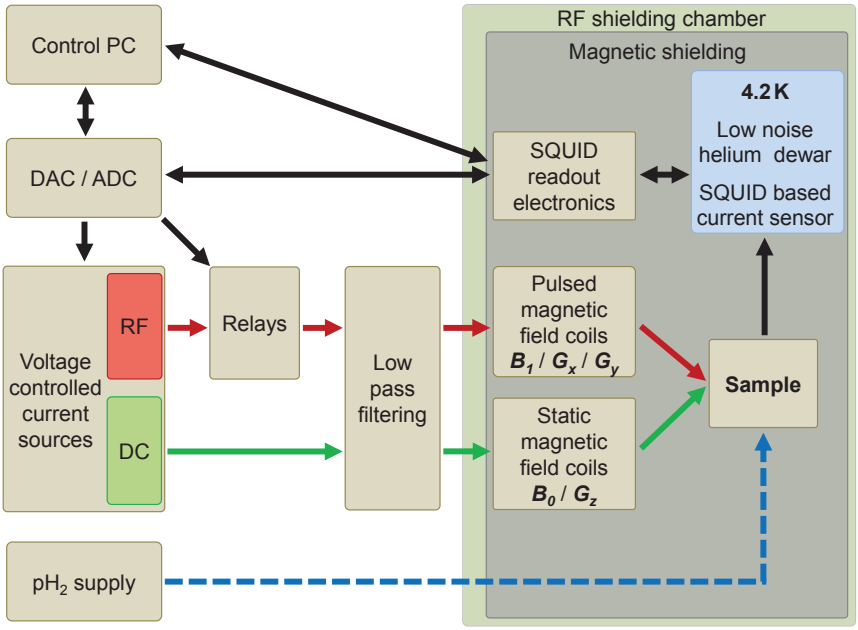

Figure 5.1.: Schematic overview flow chart of the ULF NMR/MRI system. All needed components are shown. The way the individual components interact with each other is indicated by the arrows.

An ADC/DAC system is used to control the VCCSs, the mechanical relays and the SQUID electronics according to the programmed sequence. The produced currents are fed into the RF shielding chamber via screwable low pass filters, where they are connected to the coils. The whole coil system, the sample and the SQUID are additionally magnetically shielded. The pH_2 is produced on demand on-site by an in-house developed pH_2

generator and fed into the chamber by silicone and PE hoses. The sample is contained in a sample container that allows the pH_2 to bubble through the liquid sample to achieve hyperpolarization. After the excitation pulses, a NMR signal arises from the sample and is subsequently detected by the SCS and read out by the ADC system, which eventually sends the data to the computer. Here the acquired data will be processed further.

5.1. DAC/ADC system and current sources

5.1.1. DAC/ADC system

For generating analog/digital output signals and acquiring analog input data, a National Instruments DAC/ADC system is used. For data acquisition and outputting generated NMR pulses, a NI PXIe-6363 module is used [Nat17a]. It has 4 analog outputs, each can deliver ± 10V at 16bit resolution and 2.86 MS/s. It also offers 32 analog input channels capable of ± 10V at 16bit resolution, the sample rate, however, varies depending on the usage (2.00 MS/s if one channel is read out, 1 MS/s for multi channel applications). Due to the huge amount of control signals needed, e.g. for opening/closing the relays, a second PXI analog output module is required. A NI PXI-6723 module has been chosen [Nat17b]. It offers 32 analog outputs that are capable of ± 10V at 13bit resolution and 0.80 MS/s (one channel)/0.045 MS/s (32 channels). Table 5.1 summarizes the DAC/ADC system specifications.

5.1.2. Voltage controlled current sources

The ULF NMR/MRI system needs a variety of different current sources to drive the different coils. Voltage sources are not feasible for this task (unless they are individually optimized for one very coil) for two reasons. The first problem addresses the AC currents used for exitation pulses. An AC control signal applied to a voltage source only ensures that the output clamps are at a given voltage. However, since coils not only have an ohmic impedance but also a reactive impedance (which is increasing with frequency ω and inductance L: $Z_{\text{coil}} = R_{\text{DC}} + i\omega L$), a phase shift between applied voltage and the current flowing appears. For fast changing voltages, this leads to heavily distorted current waveforms flowing through the coil, resulting in undefined magnetic fields. The second problem addresses DC currents. If

Table 5.1.: ULF NMR/MRI DAC/ADC system specifications.

	PXIe-6363	PXI-6723
Analog input channels	32	-
Analog input sample rate (MS/s)	2/1 (see text)	-
Analog input resolution (Bit)	16	-
Maximum input voltage (V)	± 10	-
Analog output channels	4	32
Analog output sample rate (MS/s)	2.86	0.80/0.045 (see text)
Analog output resolution (Bit)	16	13
Maximum output voltage (V)	± 10	± 10

a constant voltage is applied to a coil which is tightly wrapped and/or has a high DC resistance, the current through the coil will change over time due to Joule heating of the wire and a resulting resistance change. Both problems can be solved by employing current sources, where the internal circuitry is controlling a current instead of a voltage. Additionally, all current sources have to be controllable by a control voltage coming from the DAC to act as a voltage-to-current transducer. One important note: current sources have to be connected to a load at any time while operating. Trying to operate current sources without a load or disconnecting the load (especially inductive loads) during operation can lead to permanent damage since the current sources will do whatever it takes to achieve the current set value. Practically, the output stage transistors are exposed to the power rail voltages which in almost all cases would damage them permanently.
For DC magnetic fields, on the one hand, ultra-low noise current sources are required to drive the coils producing magnetic fields that are either always on during the sequence (e.g. the $\vec{B}_0$ field) or getting ramped quickly to a DC current value which has to be constant for a given time (e.g. the z-gradient $\vec{G}_z$ in case of phase encoding). Current noise of the $\vec{B}_0$ VCCS, for instance, directly affects the noise floor of the total setup. Since it is practically impossible to align $\vec{B}_0$ perfectly orthogonally to the pickup loop, a small parasitic area is present at any time. Thus, current noise of the VCCS is directly converted into $\vec{B}_0$ noise, which then couples into the sensor and

raises the noise floor. On the other hand, for the excitation pulses, VCCSs are needed that are able to drive rapidly changing signals through rather large coils (e.g. $L_{\vec{B}_1} = 32.5\,\mu$H, cf. chapter 5.2). The current noise of the AC VCCSs is not critical since they are only galvanically coupled to the system during the pulses.

5.1.3. DC current sources

To drive the $\vec{B}_0$ coil, the linear regulated bipolar current source BCS 5/75 (custom product) from HighFinesse is employed [Hig17]. The device is optimized for driving ultra-low noise DC currents through highly inductive loads. It can deliver up to ± 5 A and ± 75 V. It is powered by three phase mains voltage. The output current drift is guaranteed to be <5 ppm/K. The device is water cooled, which guaranties both a secure temperature range for the bipolar output stage and practically no temperature change induced current drift.
The $\vec{G}_z$ gradient coil (cf. 5.2) is driven by a replica of the current source presented in [ZA14], however heavy improvements have been implemented by the MPI's electronical engineer T. Steffen. It is a linear regulated bipolar current source with a sample-and-hold circuitry involving a voltage source mode. The amplifier can deliver up to ± 10 A and ± 100 V and has a current slew rate $\mathrm{SR}_I = 0.1\,\mathrm{A}/\mu\mathrm{s}$ for an inductive load of $L_{\vec{G}_z} = 2.78$ mH. During operation, the amplifier receives a desired set current value from the DAC and it operates as a high power current source, i.e. its internal control loop controls the output current by measuring the voltage drop across a low-ohmic shunt resistor in series to the coil. As soon as the output current has settled to the steady state (i.e. the set current value), the amplifier changes the internal control loop to a voltage controlled sample-and-hold control loop. Therefore, the voltage drop across the coil for the steady state set current is measured (sampled) by the integrated sample-and-hold solution LF398 of the company Texas Instruments and is stored in a polypropylene type low leakage capacitor (hold) [Tex]. Due to the low charge leakage of the capacitor and the high input impedance of the LF398 $Z_{\mathrm{in}} > 10\,\mathrm{G}\Omega$, holding times of the stored voltage of > 10 s can be achieved. The result is an ultra-low noise current flowing through the coil. The current noise in the sample-and-hold mode is given by the voltage noise of the sample-and-hold circuit divided by the impedance of the coil and the shunt resistor: $S_{i,SH}^{1/2} = S_{v,SH}^{1/2}/(R_{\mathrm{shunt}} + R_{\mathrm{DC,coil}} + i\omega L_{\mathrm{coil}})$. The holding time of this ultra-

low noise mode, however, is practically limited to two to three seconds and duty cycles <50%. The reason for this limitation is the Joule heating of the coil windings and the resulting resistance change. This leads to a DC offset of the set current that increases with increasing holding time and current since the voltage across the coil is kept constant.

5.1.4. AC current sources

The $\vec{B}_1$ coil is driven by a modified stereo audio amplifier. The audio amplifier (60-120D DOLIFET SE by ABACUS) is a voltage source that was optimized by the manufacturer specifically for the $\vec{B}_1$ coil [ABA17]. To deliver enough voltage to drive the coil, both individual output channels were connected in series to double the possible voltage output. This way, the amplifier has a RMS output power of 220 W and a power bandwidth of $f_{\mathrm{PB}} = 150\,\mathrm{kHz}$.
A Kepco BOP 100-4 ML linear regulated bipolar voltage/current source is used to drive the prepolarization coil [Kep17]. It is especially designed to drive heavy inductive loads and can deliver up to $\pm 4\,\mathrm{A}$ and $\pm 100\,\mathrm{V}$. This amplifier can either be operated as a voltage or a current source, respectively, and offers a bandwidth of $f_{-3\mathrm{dB}} = 1.7\,\mathrm{kHz}$. The $\vec{G}_{x,y}$ gradient coils are powered by A1110-16-QE precision power amplifiers by the company Dr. Hubert [Dr.17]. It has an output capability of up to $\pm 28\,\mathrm{A}$ and $\pm 75\,\mathrm{V}$. It has a power bandwidth of $f_{\mathrm{PB}} = 200\,\mathrm{kHz}$, a bandwidth $f_{-3\mathrm{dB}} = 1\,\mathrm{MHz}$ and a slew rate $\mathrm{SR} = 100\,\mathrm{V}/\mu\mathrm{s}$. The A1110-16-QE can be operated as a voltage or current source, too. It can be controlled either by analog control signals or by the supplied software package.

5.1.5. Relay switches

The AC current sources that drive the coils for pulsed magnetic fields are optimized for high output power to precisely produce the desired waveform. This comes at the price of increased current and voltage noise densities of the amplifier output stage. Due to the high sensitivity of a SQUID, especially in combination with a connected pickup coil, and in combination with a conceptual misalignment of the coil setup, the increased output noise has a striking influence on the noise performance of the whole setup. Even when the output current of the AC VCCS is set to 0 A when no pulse sequence is running, the output noise current/voltage is large enough to completely

overload the SQUID. A simple yet effective way to get completely rid of this problem is to simply disconnect the noisy amplifiers from the coil system when they are not needed. This can be achieved by mechanical relays or semiconductor based relays of circuits. Using MOSFETs, a transmission gate circuit (i.e. a solid state switch allowing current transport in both directions) was realized which achieved turn on/off times $t_{\mathrm{on,off}} = 200\,\mathrm{ns}$. However, the achieved insulation resistance $R \approx 10\,\mathrm{G\Omega}$ was not sufficient, resulting in a huge increase of the white noise level in the noise spectra and the occurrence of spikes resulting from the internal circuitry of the current sources. Thus, the final implementation is accomplished using mechanical relays. Fig. 5.2(a) shows a schematic of the relay implementation. Each

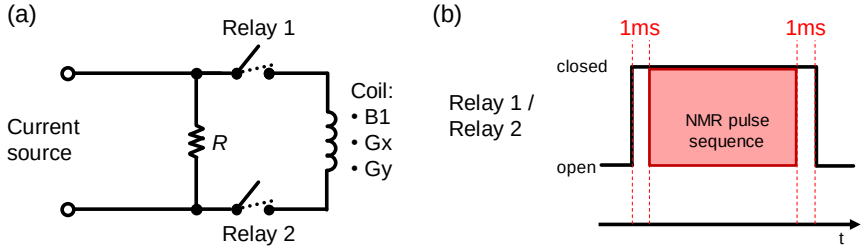

Figure 5.2.: Schematic illustration of the relay setup for AC current sources. This relay arrangement ensures that there is a possible current path at any time. (b) shows the timing sequence of the relay control.

relay has a control input designed for voltage levels of TTL pulses (omitted for clarity in Fig. 5.2(a)). The whole circuit consists of two relays which are closed/opened 1 ms before the NMR pulse sequence starts or 1 ms after the sequence is over, respectively (cf. Fig. 5.2(b)). For safety reasons a resistor $R = 500\,\Omega$ is implemented. The relays connect and disconnect the coils from the VCCS. Relays don't close or open instantly once the TTL control signal is applied. Thus, when the NMR sequence timings for the TTL pulses are set incorrectly, it could happen (and has happened in the past) that the current source tries to sent current even though the relays are still open which can potentially damaging the current source. Therefore the resistor can supply a (high ohmic) current path until the relays are closed. For low current applications (e.g. $\vec{B}_1$ pulses) Gigavac GR3BJA335 relays [Gig17] are used. They are rated for $V_{\mathrm{max}} = 160\,\mathrm{V}$ and $I_{\mathrm{max}} = 3\,\mathrm{A}$

and offer short closing (100 μs) and release times (200 μs). For the high current gradients $\vec{G}_{x,y}$, the automotive relays TE Connectivity 2-1904058-5 are used [TE 17]. They are rated for $V_{\max} = 400\,\mathrm{V}$ and $I_{\max} = 20\,\mathrm{A}$. Due to the huge current carrying capability, high mass contacts are used which drastically increases the switching times (closing: 2.5 ms, release: ≈ 1 ms.).

5.1.6. Low pass feed-through filters

The shielded cables connecting the VCCSs and the coils have to be fed into the RF shielding chamber without deteriorating the shielding effect. This is achieved by using feedthrough low pass filters which are designed to be screwed to the shielding chamber walls. Tesch 02000203 feedthrough filters are used for all DC lines like the $\vec{B}_0$ coil [tes17a]. They have a Π filter topology consisting of two capacitors $C_\Pi = 250\,\mathrm{nF}$ and one inductance $L_\Pi = 1.5\,\mu\mathrm{H}$, a cutoff frequency $f_{-3dB} = 180\,\mathrm{kHz}$ and are rated for 16 A and 250 V.
For all other cables ($\vec{G}_x$,$\vec{G}_y$,$\vec{G}_z$) Tesch 02000207 filters are employed [tes17b]. They are also realized by a Π filter topology consisting of two capacitors $C_\Pi = 5\,\mathrm{nF}$ and one inductance $L_\Pi = 0.4\,\mu\mathrm{H}$. They have a cutoff frequency $f_{-3dB} = 2.5\,\mathrm{MHz}$ and are rated for 30 A and 600 V. The increased bandwidth of $f_{-3dB} = 2.5\,\mathrm{MHz}$ is of importance. Since the gradient current profiles ideally are of trapezoidal shape, high frequency components have to be present to achieve the sharp transitions needed from the linearly rising/falling current to the steady state constant current.

5.2. Coil system

The coil system consists of coils for the homogenous measuring field $\vec{B}_0$, the pulsed excitation field $\vec{B}_1$, the prepolarizing field $\vec{B}_P$ and for all the gradients $\vec{G}_x$, $\vec{G}_y$ and $\vec{G}_z$ needed for MRI experiments. Each of the itemized coils will be explained now.

5.2.1. $\vec{B}_0$: Tetracoil

The coil of the measuring field $\vec{B}_0$ has to meet various requirements. The coil has to produce a magnetic field that is highly uniform over the whole sample space. The ratio between overall dimension of the coil and the

region of uniform magnetic field should be as small as possible to relieve the demands of the current source. Additionally, the sample, which will be placed in the center of the coil, has to be easily accessible. A coil implementation which fulfills all the requirements was presented by Gottardi et al. [GMA+03]. This coil approach involves four coils which are geometrically constrained on a sphere. It was shown by Smythe [Smy67], that a uniform spherical current shell produces a completely uniform magnetic field in the confined volume. To achieve good accessibility the spherical current shell is approximated by four coaxial coils (cf. fig 5.3). Coil 1 and 4 as well as coil 2 and 3 forming a corresponding coil couple which share the same parameter set. a_1 and a_2 are the radii of each couple of coils, respectively (cf. Fig. 5.3). b_1 and b_2 are the distances of each couple of coils to the origin (center of the enclosing sphere, cf. Fig. 5.3).

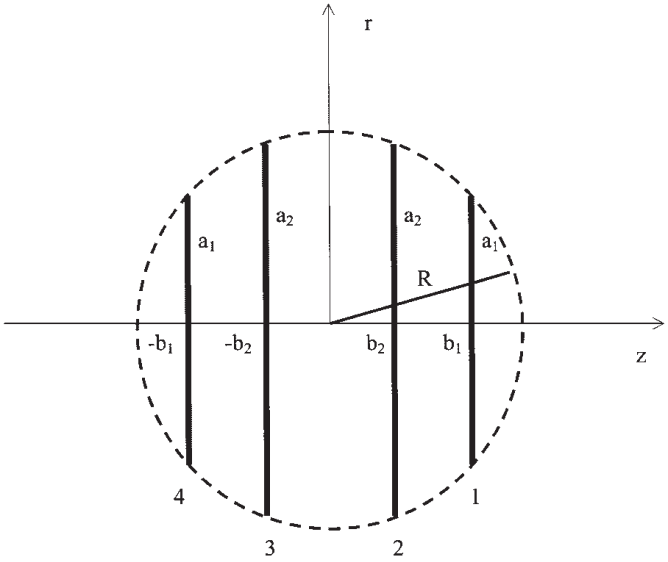

Figure 5.3.: Schematic arrangement of the four coils of a tetracoil. The resulting magnetic field is aligned along the z-axis. Taken from [GMA+03].

From Fig. 5.3 a set of parameters can be defined:

$$\begin{aligned} i &= IN_1/IN_2 \overset{I_1=I_2}{=} N_1/N_2 && (5.1)\\ q &= a_1/a_2 && (5.2)\\ \beta_1 &= |b_1|/a_1 && (5.3)\\ \beta_2 &= |b_2|/a_2, && (5.4) \end{aligned}$$

where IN_1 and IN_2 are the products current $\times$ turns of each couple of coils. If $I_1 = I_2$ (as its the case for a series connection of all coils), i is given by the ratio of the coil turns N_1 and N_2). It can be shown analytically, that the parameter set

$$\begin{aligned} i &= 0.6822\\ q &= 0.6718\\ \beta_1 &= 1.1880\\ \beta_2 &= 0.2975 \end{aligned}$$

maximizes the magnetically uniform space and the first six spatial derivatives of the produced magnetic field vanish [GMA+03]. Various parameter sets have been presented by Gottardi et al. where the magnetically uniform space is only reduced by maximum 5% compared to the ideal parameter set but allows for better accessibility to the coil center due to improved coil spacings. The final coil implementation uses one of the pre-calculated parameter sets of Gottardi et al. [GMA+03]:

$$\begin{aligned} a_1 &= 0.6216 \times R = 161.62\,\text{mm}\\ b_1 &= 0.7833 \times R = 203.66\,\text{mm}\\ a_2 &= 0.9556 \times R = 248.46\,\text{mm}\\ b_2 &= 0.2955 \times R = 76.83\,\text{mm}\\ N_1/N_2 &= 80/121 \end{aligned} \qquad (5.5)$$

where $R = 260\,\text{mm}$ is the radius of the enclosing sphere. The manufactured and assembled coil can be seen in fig 5.4. The coil bodies are made of PVC and are connected to a PVC made supporting frame by screws made of RENY (glass-fiber-reinforced polyamide, S.A.R.L. TSF) [S.A]. Even

though PEEK or GFRP offers higher glass transition temperatures and are more rigid, PVC was chosen for cost efficiency. The coils have been wound using enameled copper wire of $\varnothing = 1\,\mathrm{mm}$. The two small coils have inductances $L_{\mathrm{small}} = 4.93/4.94\,\mathrm{mH}$ while the two bigger coils have inductances $L_{\mathrm{big}} = 18.34/18.26\,\mathrm{mH}$, respectively. The complete tetracoil has an inductance $L_{\vec{B}_0,\mathrm{meas}} = 65.1\,\mathrm{mH}$ and a DC resistance $R_{\mathrm{DC}} = 12.2\,\Omega$. A slight deviation from $L_{\vec{B}_0,\mathrm{sim}} = 61.5\,\mathrm{mH}$ can be observed. The deviation is present most probably for two reasons. First, the measurement included $\approx 4\,\mathrm{m}$ of twisted feed lines however this contribution should be rather small due to the small inductance of mutually twisted wires carrying currents of opposite direction. Second, during the design process the coil was simulated using single turn coils which carried the current according to the particular current $\times$ turn rating (80 A or 121 A, respectively). Due to the physical size of the wires placed next to each other in the real implementation, however, the individual coils are closer to each other compared to the simulation which leads to an increased mutual inductance between the loops and thus to an overall increase of inductance. The current-to-field transfer coefficient was measured to be $k_{\vec{B}_0} = 660\,\mu\mathrm{T/A}$.

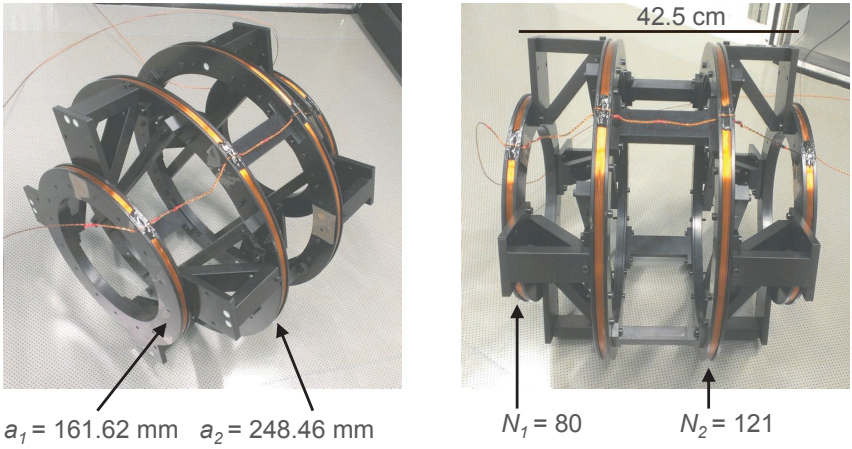

Figure 5.4.: Photographs of the assembled and wound tetracoil.

5.2.2. $\vec{B}_1$: Helmholtz coil

The NMR excitation pulses are created by a Helmholtz coil. A Helmholtz coil consists of two identical coils of the radius R, which is also their separation distance. A Helmholtz coil has a drastically smaller region of uniform magnetic field compared to a tetracoil. However, its field homogeneity is sufficient for the excitation of spins. The excitation waveform usually is prepared such that it offers a certain excitation bandwidth of $200 - 400\,\mathrm{Hz}$ around the center frequency f_0, therefore small $\vec{B}_1$ field inhomogeneities are negligible. The coil bodies are made of PVC. Each of the two coils consist of 4 windings of $\varnothing = 1.25\,\mathrm{mm}$ thick enameled copper wire and has an effective radius $r_{\vec{B}_1} = 18.65\,\mathrm{cm}$. The complete coil has an inductance $L_{\vec{B}_1} = 32.5\,\mu\mathrm{H}$ and a DC resistance $R_{\vec{B}_1} = 0.25\,\Omega$ (including $\approx 4\,\mathrm{m}$ twisted feed lines). The received value is close to the simulated value of $L_{\vec{B}_1,\mathrm{sim}} = 26.5\,\mu\mathrm{H}$. The deviation can be attributed to the $\approx 4\,\mathrm{m}$ of twisted feed lines. The coil is oriented such, that its magnetic field is oriented perpendicular to the $\vec{B}_0$ field.

5.2.3. $\vec{B}_P$: Prepolarization coil

Two different prepolarization coils have been realized. The first one is a small solenoid coil while the second one is realized as a large Helmholtz coil.

The solenoid coil has a height of $h_{\vec{B}_{P,1}} = 5\,\mathrm{mm}$ and an effective diameter $\varnothing_{\vec{B}_{P,1}} = 35\,\mathrm{mm}$ such that the sample container (cf. chapter 5.3) perfectly fits into the bore. The coil has 131 windings of enameled copper wire of $\varnothing = 190\,\mu\mathrm{m}$. The coil has an inductance $L_{\vec{B}_{P,1}} = 16.6\,\mathrm{mH}$ and a DC resistance $R_{\vec{B}_{P,1}} = 2.9\,\Omega$. Due to the large DC resistance $R_{\vec{B}_{P,1}}$ and relatively large currents of up to $I_{\vec{B}_{P,1}} = 2.5\,\mathrm{A}$ a large amount of heat will be dissipated during operation. Therefore, the coil body is made of PEEK which provides a high glass-transition temperature of $143\,^\circ\mathrm{C}$ compared to $81\,^\circ\mathrm{C}$ of PVC. Additionally, to prevent the sample container and thus the sample from unnecessary heating, a flow of compressed air surrounding the coil was installed providing sufficient cooling power. It is mounted such that the coil center coincides with the one of the tetracoil. The coil is oriented such, that its magnetic field is oriented perpendicular to both the $\vec{B}_0$ and $\vec{B}_1$ fields. The current-to-field transfer coefficient is $k_{\vec{B}_{P,1}} = 3.85\,\mathrm{mT/A}$.

The Helmholtz coil is dimensioned such, that a sample placed at the bottom

of the dewar is right in the center of the coil. The coil is also oriented such, that its magnetic field is oriented perpendicular to both the $\vec{B}_0$ and $\vec{B}_1$ fields. That implies, that the tail of the dewar has to fit through the upper one of the two coils. As a result of this large Helmholtz coil implementation, the $\vec{B}_P$ field is much more homogenous than that of the solenoid coil. Each of the coils has an effective diameter of $\varnothing_{\vec{B}_{P,2}} = 166\,\mathrm{mm}$ and holds 256 windings of enameled copper wire of $\varnothing = 1.25\,\mathrm{mm}$. The assembled coil has an inductance $L_{\vec{B}_{P,2}} = 41\,\mathrm{mH}$ and a DC resistance $R_{\vec{B}_{P,2}} = 4.1\,\Omega$. Due to the larger size, the current-to-field transfer coefficient $k_{\vec{B}_{P,2}} = 2.58\,\mathrm{mT/A}$ is smaller than for the solenoid coil. However, since thicker wire was used, the coil can carry way more current which compensates for the smaller $k_{\vec{B}_{P,2}}$.

5.2.4. $\vec{G}_z$: Maxwell coil

The gradient magnetic field $\vec{G}_z = \partial\vec{B}_z/\partial z$ that superimposes the $\vec{B}_0$ magnetic field originating from the tetracoil, is created by a round Maxwell coil. A Maxwell coil is closely related to the Helmholtz coil arrangement used for the $\vec{B}_1$ field. The two individual coils are arranged in a coaxial manner, too, yet there are two differences. First, the current in the respective coils flows in opposite directions. This leads to a perfect (in the ideal case of identical coils) cancellation of the $\vec{B}_z$ component of the gradient magnetic field right in the middle between the two coils. Second, it can be shown analytically that if the distance of the two coils is increased from $r_{\vec{G}_z}$ to $d = \sqrt{3} \times r_{\vec{G}_z}$, the second and third derivatives of $\vec{B}_z$ vanish: $\frac{\partial^2\vec{B}}{\partial z^2} = \frac{\partial^3\vec{B}}{\partial z^3} = 0$. The gradient along the z axis can be calculated using the formula

$$\frac{\mathrm{d}\,\vec{B}_z}{\mathrm{dz}} = 3\mu_0 I N R^2 \frac{d}{(r^2_{\vec{G}_z} + d^2)^{5/2}}, \tag{5.6}$$

where I is the applied current and N the number of coil turns per coil. The $\vec{G}_z$ coil bodies are made of PVC. Each of the two coils has a radius $r_{\vec{G}_z} = 23.1\,\mathrm{cm}$ and consist of 30 windings of $\varnothing = 0.315\,\mathrm{mm}$ thick enameled copper wire which leads to $\vec{G}_{z,\mathrm{calc}} \approx 0.45\,\mathrm{mT/Am}$. The assembled coil has an inductance $L_{\vec{G}_z} = 2.78\,\mathrm{mH}$ and a DC resistance $R_{\vec{G}_z} = 12.75\,\Omega$ (including $\approx 4\,\mathrm{m}$ twisted feed lines).

5.2.5. $\vec{G}_x$ and $\vec{G}_y$: Concave coils

To apply gradients in the x or y direction, various coil arrangements that approximate a linear magnetic field gradient are possible [Jin98, KEMV14]. The most common approach is done by using a set of 4 rectangular coils per spatial dimension [ZMV+07, HDC+13] (cf. Fig. 5.5(a)). An improved version of the rectangular coils was presented by Mößle et al., where the coil shape was numerically optimized to yield a gradient more linear as the rectangular coil shape. The result is a coil where the wire next to the principal magnetic field axis (i.e. the z axis) is of a slightly concave shape (cf. Fig. 5.5(b)) [MHM+06]. The concave gradient coil approach has been adopted for our setup, however the coil shape was numerically optimized specifically for the employed tetracoil used for the $\vec{B}_0$ field.

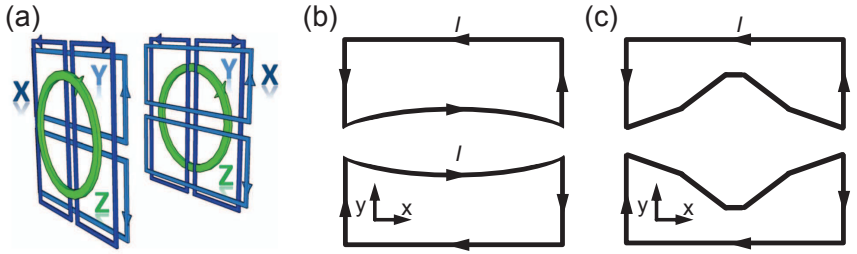

Figure 5.5.: (a) Rectangular gradient coil sets for x (dark blue) and y gradients (light blue), also the Maxwell coil for the z gradient can be seen. Taken from [HDC+13]. Adapted from [MHM+06]. (b) Schematic layout of a concave gradient coil (here: y gradient). (c) Shape of the gradient coils that have been implemented after their linearity was optimized using Matlab.

The ansatz of the coil shape optimization can be seen in Fig. 5.6. The coil shape was modeled by six two dimensional vectors $\vec{P}_i = (x_i, y_i)$. Two of those vectors ($\vec{P}_0$ and $\vec{P}_1$) have fixed coordinates and identical y coordinates $y_0 = y_1$. $\vec{P}_0$ defines the symmetry axis of the coil, while $\vec{P}_1$ defines the maximum dimensions of the coil by its x_1 value and was defined by the dimensions of the $\vec{B}_0$ coil. Point $\vec{P}_2$ had its x value fixed with the condition $x_2 = x_1$ while y_2 is a optimization parameter. The x and y components of $\vec{P}_3$ and $\vec{P}_4$ were not fixed and accessible to the optimization algorithm. $\vec{P}_5$ had its x value fixed to $x_5 = x_0 = 0$ while y_5 also is a optimization

parameter. The six point were mirrored along the x-axis and the y-axis.

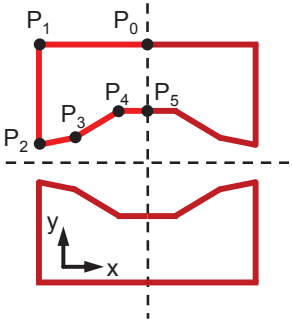

Figure 5.6.: Schematic illustration of the optimization ansatz to yield a maximum linear gradient of the concave gradient coils in combination with the tetra-coil.

Corresponding points were connected by vectors which defined the current path which results in two complete coils integrated into Matlab.

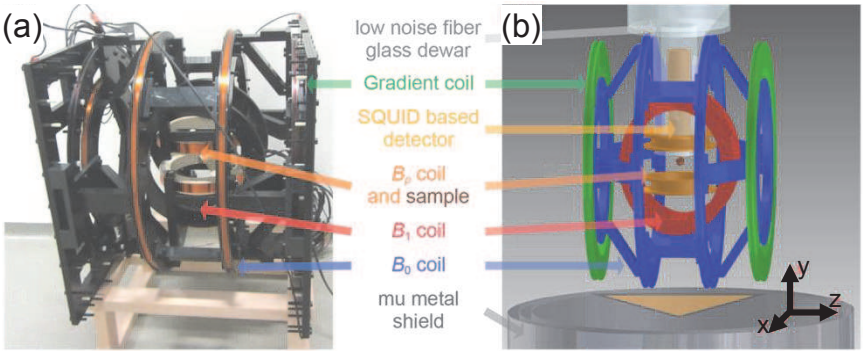

Figure 5.7.: (a) shows the assembled coil system ($\vec{G}_y$-coil not installed). (b) Colored computer aided design (CAD) drawings of the coils to easily identify the coils in (a).

Subsequently, Matlab iteratively varied y_2, y_5, $\vec{P}_3$ and $\vec{P}_4$ in order to maximize the linearity of the resulting gradient. The resulting shape is de-

picted in Fig. 5.5(c). The coils are would using 20 windings of $\varnothing = 1.25\,\mathrm{mm}$ thick enameled copper wire. This leads to $L_{\vec{G}_x} = 1.43\,\mathrm{mH}/L_{\vec{G}_y} = 1.53\,\mathrm{mH}$ and $R_{\vec{G}_x} = 1.80\,\Omega/R_{\vec{G}_y} = 1.90\,\Omega$. For $\vec{G}_x$ and $\vec{G}_y$ Matlab simulations yield $\vec{G}_{x,\mathrm{sim}} \approx 0.183\,\mathrm{mT/Am}$ and $\vec{G}_{y,\mathrm{sim}} \approx 0.171\,\mathrm{mT/Am}$, respectively. Table 5.2 summarizes the parameters of the coil system. The assembled coil system can be seen in Fig. 5.7. The picture lacks the $\vec{G}_y$-coil since it was not yet fabricated while this thesis has been written. The sample position is schematically indicated by the brown sphere in Fig. 5.7(b).

Table 5.2.: Parameters of the complete coil system

	$\vec{B}_0$	$\vec{B}_1$	$\vec{B}_p$, old	$\vec{B}_p$, new	$\vec{G}_x$	$\vec{G}_y$	$\vec{G}_z$
R_{dc} (Ω)	12.20	0.25	2.90	4.10	1.80	1.90	12.75
L (mH)	65.12	0.0325	16.60	41.00	1.43	1.53	2.78
Wire $\varnothing$ (mm)	1	1.25	0.19	1.25	1.25	1.25	0.315
Radius (mm)	161.6/ 248.5	186.5	17.5	83.0	-	-	231.0
Windings	80/ 121	4	131	256	20	20	30
k (mT/A)	0.660	0.025	3.85	2.58	-	-	-
$\vec{G}$ (mT/Am)	-	-	-	-	0.183	0.171	0.45

5.2.6. Numerical evaluation of the completed coil system

Finite elements simulations of all DC coils of the coil system (i.e. all coils except $\vec{B}_P$ and $\vec{B}_1$) have been performed using Comsol 5.0 [COM17]. The presented simulation results are restricted to a spatial region of $\pm 5\,\mathrm{cm}$ in every direction around the center of the tetracoil where the sample will be located during experiments. The simulations of the tetracoil confirm the high uniformity of the resulting magnetic field and they predict a current-to-field conversion factor $k_{\vec{B}_0,\mathrm{sim}} = 668.87\,\mu\mathrm{T/A}$. Once the tetracoil is suspended into the μ-metal shielding, the current-to-field conversion factor increases to $k_{\vec{B}_0,\mathrm{sim}} = 764.83\,\mu\mathrm{T/A}$. The current-to-field conversion factors of the actually implemented coil where determined by NMR measurements. By feeding a precise current $I = 1.000\,\mathrm{A}$ through the coil, the position of the

NMR peak of purified water (i.e. a proton peak) was determined. By using the relation $|\vec{B}_0| = f_{\mathrm{NMR}}/\gamma_n$ the exact field value can be calculated. The NMR peaks were located at $f_{I=1A} = 28.100\,\mathrm{kHz}$ without μ-metal shielding and $f_{I=1A,\mu} = 32.358\,\mathrm{kHz}$ inside the μ-metal shielding. This translates to $k_{\vec{B}_0} = 660\,\mu\mathrm{T}$ without and $k_{\vec{B}_{0,\mu}} = 760\,\mu\mathrm{T}$ with μ-metal shielding, which matches the simulated values to 1.32% without and 0.63% with μ-metal shielding, respectively.

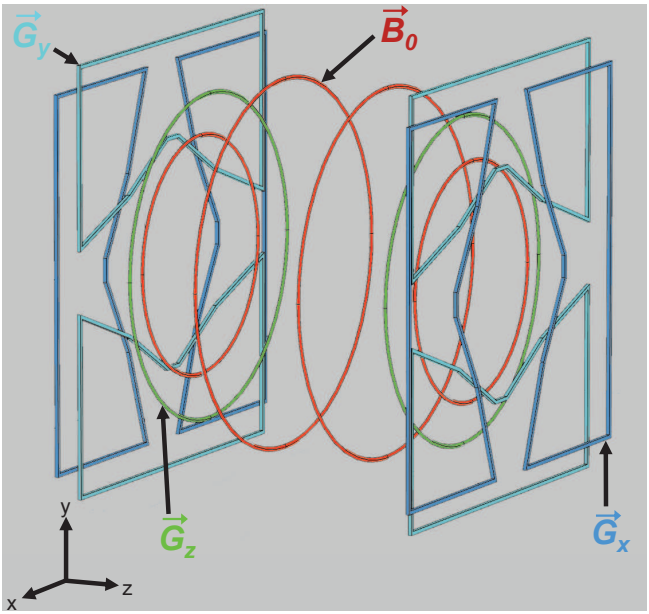

Figure 5.8.: Comsol implementation of the coil system (except $\vec{B}_1$ and $\vec{B}_P$ coils)

In contrast to the exact quantity of the magnetic field strength, for the gradients the linearity in presence of the other coils is of interest. The Comsol implementations of the $\vec{G}_x$ and $\vec{G}_y$ coils vary in shape to the eventually realized coils. This is owed to the fact, that the shape of the simulated coils were not producible. Due to the concave shape of the individual coils, the coil wire had to be guided in machined grooves in the PVC body to stay in shape. The resulting real coil shape, however, would be very complex

to implement into Comsol and due to the complex geometry, the simulation time would be increased drastically. Therefore, the $\vec{G}_x$ and $\vec{G}_y$ coils are implemented according to the optimized Matlab design and deviations between measured and simulated gradient strength can be expected. Since the linearity of the gradient is given by the coil shape, which is preserved to a great extent, the simulation results are still representative for the performance of the gradient coil. Figure 5.8 shows a colorized screen shot of the graphics window of Comsol. The individual coils belonging together are colored for clarity ($\vec{B}_0$ coil: red, $\vec{G}_z$ coils: green, $\vec{G}_y$ coils: turquoise, $\vec{G}_x$ coil: blue). Figure 5.9 summarizes the principal simulation results (same coordinate system as in Fig. 5.8): (a) shows the B_z component of the measurement field $\vec{B}_0$, (b) - (d) shows the B_z component of the gradient magnetic fields and (e) and (f) show the resulting B_z components once all fields are turned on for two different projection planes. During the simulations (a) - (d), only the corresponding coils were current biased (1 A), however, the other coils were physically present. The effect of the presence of the unpowered coils can be seen clearly in (a) and (b) (and are not present if the coils are simulated separately). The B_z component of B_0 exhibits some small distortions and over the whole area of interest field deviations on the order of $\approx 5\,\mu$T appear. Apart from that, all gradients (especially G_z) show a very high linearity.

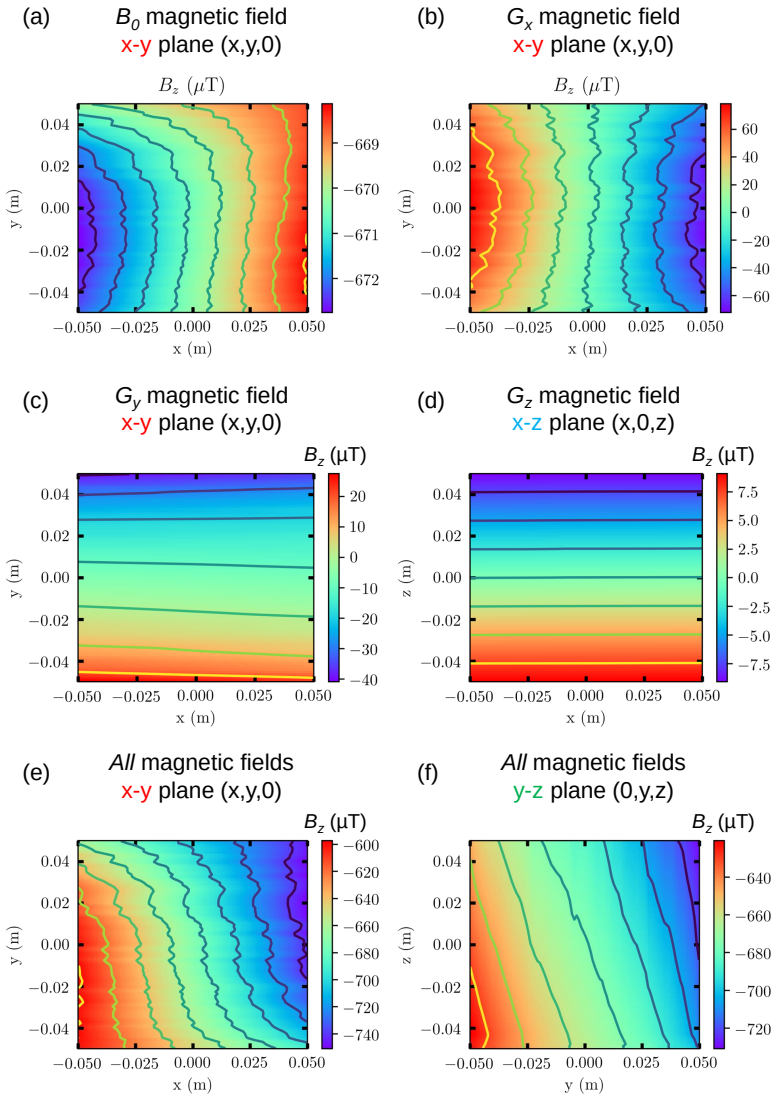

Figure 5.9.: Comsol evaluation of the coil system. (a) B_z component of the measurement field $\vec{B}_0$, (b) - (d) B_z component of the gradient magnetic fields, (e) - (f) Resulting B_z components once all fields are turned on for two different projection planes.

Once all coils are current biased, a two dimensional gradient map of B_z is obtained. The resulting gradient strength vary from the calculated values presented in chapter 5.2. This is caused by the fact that in the Comsol simulation only one coil winding (determined by the geometry of the coil) and a different current was used. However this is not critical because only the linearity of the gradients is of interest (as stated above) while its quantity simply scales with the current.

5.3. Sample container

To bring the pH_2 in contact with the catalyst and the target molecule in a controlled manner, a small sample container was designed that allows for convenient handling during experiments. Figure 5.10(a) shows a cross section of the realized sample container. It is made of PEEK. It has a lateral side length $l_o = 25\,\text{mm}$ and a total heigth $h_o = 30\,\text{mm}$. The inner volume has a diameter $\varnothing_i = 10\,\text{mm}$ and an inner height $h_i = 24.5\,\text{mm}$, giving a sample volume $V = 1.9\,\text{ml}$.

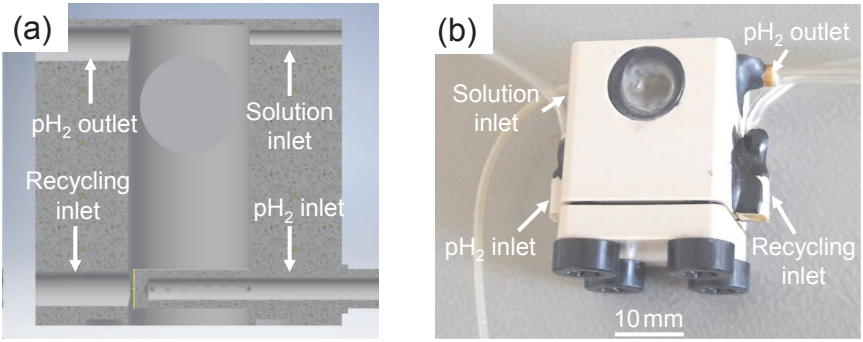

Figure 5.10.: (a) Cross section of the CAD drawing of the sample container. (b) Photograph of the fully assembled container.

A pH_2 inlet is located at the right bottom side of the container. To achieve a homogenous distribution of the pH_2 gas within the catalyst, a spray nozzle containing 14 outlets (pH_2 outlet diameter $\varnothing\,0.5\,\text{mm}$) is implemented. At the top side, there are two differently sized holes. The smaller one (cf. Fig. 5.10(a) on the right side) is the solution inlet (so-

lution inlet diameter ⌀ 1.5 mm). A PTFE hose glued (glue used: Stycast 2850 FT [Hen17]) into the solution inlet is connected to a syringe which is used to both press the solution into the container as well as a solution storage reservoir for long term measurements where refilling of the container is necessary on a regular basis. The larger hole on the opposite side has a diameter ⌀ 3.0 mm and is used as the pH_2 outlet. A PUR hose glued (glue used: Stycast 2850 FT) into the pH_2 outlet leads to a collecting basin. The basin is an indispensable feature of the sample container. Due to the slight excess pressure within the container, the solution is getting pushed out of the pH_2 outlet. This fluid is collected in the collecting basin. The basin is wide enough, that the solution will stay, but the exhaust pH_2 gas can escape. At the basin, there is a second PUR hose connected, which is running to the hole on the bottom left in Fig. 5.10(a). This allows pushed out solution to flow back from the basin to the container. This measure increased the required container refilling intervals drastically (compared to prototype container implementations which did not have the recycling system). In the middle of the container, a PMMA window is glued (glue used: Stycast 2850 FT) (cf. 5.10(b)). The window allows a visual inspection of the filling level during the filling process or measurements.

5.4. Low noise helium dewar

To provide the temperature environment for the SCS to operate ($T < T_{c,Nb} = 9.26\,K$), a glass-fiber reinforced plastic (GFRP) dewar (cf. Fig. 5.11) and liquid helium is employed. The dewar, type LH-11.5-NTE from the company Cryoton [Cry17], holds up to 11.5 l of liquid helium and has a helium boil-off rate $\cong$ 1.5 l/day (for isolation vacuum pressures $p < 1.0 \times 10^{-5}$ mbar). It offers an ultra-low noise performance of $S_B^{1/2} < 0.5\,fT/Hz^{1/2}$. The residue magnetic field noise arises from noise currents present in the one-layer gold platted Mylar thermal insulation foil which is incorporated in the dewar. The dewar is slightly customized specifically for our setup. It has a 25 cm long tail (standard value 20 cm) at the bottom where the gradiometric pickup coil is located. The enlarged length of the tail allows to place the dewar right next to the center of the coil system where the sample is located. In combination with the short hot-to-cold distance $d_{hc} = 12$ mm minimum signal loss can be achieved.

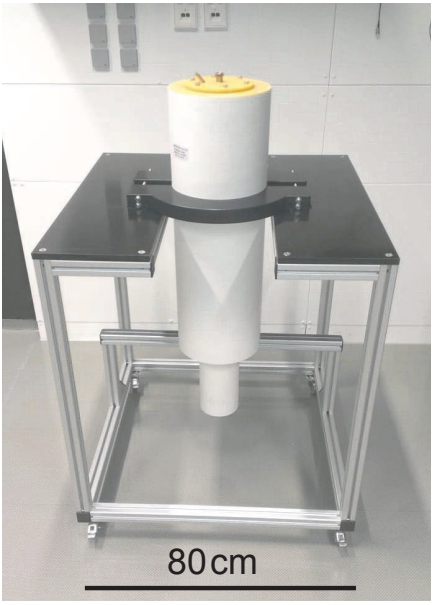

Figure 5.11.: Low noise helium dewar mounted on its storing trolley.

5.5. SQUID based sensor assembly

The sensor assembly consists of two parts: the SQUID based current sensor and the pickup coil. A photograph of the completely assembled sensor mounted to the dip stick can be seen in Fig. 5.12.

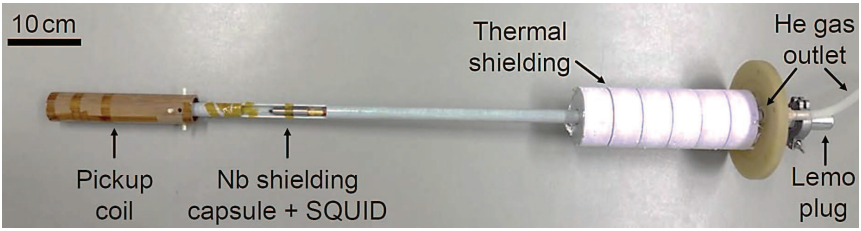

Figure 5.12.: Complete SQUID based sensor assembly

The dip stick is made of GFRP as far as possible. A thermal shielding, made of polystyrene (purple parts) is implemented to minimize the heat input into the dewar to maximize the holding time between refilling the dewar. At the top end, besides a ^{4}He gas outlet made of PEEK, a female Lemo plug socket (plug socket part number EGG.3B.324.CLL) is mounted where the Magnicon XXF-1 SQUID electronics will be inserted. From the Lemo plug socket, the feed lines for the SQUIDs (shielded against RF interference by stainless steel braid) are running down into the Nb shielding capsule (Magnicon NC-1). Inside of the Nb capsule, a commercially available current sensor (Magnicon single-stage current sensor, type C6L1, serial number: S0115, sensor ID: C633_B12) is mounted (Magnicon CAR-1). The current sensor is equipped with a connected Q spoiler, employs APF, has a nominal input inductance $L_{\mathrm{in}} = 400\,\mathrm{nH}$, an input coupling $1/M_{\mathrm{in}} = 0.516\,\mu\mathrm{A}$, a transfer coefficient $V_\Phi = 660\,\mu\mathrm{V}/\Phi_0$ and an equivalent flux noise density $S_\Phi^{1/2} = 0.8\,\mu\Phi_0/\sqrt{\mathrm{Hz}}$ in the frequency range of interest ($> 1000\,\mathrm{Hz}$).

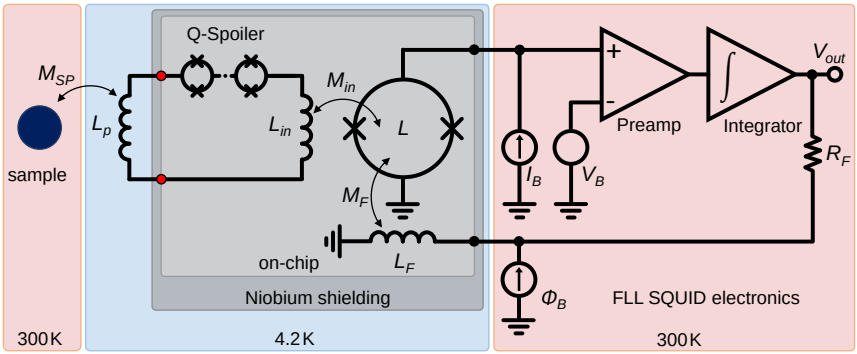

Figure 5.13.: Measurement and feedback scheme for the direct readout single stage FLL operation of a SQUID. The sample (dark blue dot) is located at $T = 300\,\mathrm{K}$ in close vicinity to the pickup coil L_p. The components inside the blue box are at cryogenic temperatures, some of them are magnetically shielded by a superconducting niobium shield (grey box). The red dots indicate the superconducting screw terminal to connect L_p to the SCS. The readout electronics (Magnicon XXF-1 [CB04, DHB06, Mag13a]) is at $T = 300\,\mathrm{K}$ and connected to the SQUID via normal conducting copper wires.

At the lower end of the dip stick, the pickup coil is connected. The pickup coil is realized by a wire-wound second-order axial gradiometer. The gradiometer body is made of a phenolic paper tube and has four machined grooves to guide the wire. It is wound from enameled niobium wire with a diameter $\varnothing = 50\,\mu\text{m}$ (Goodfellow NB005100). Both the loop diameter d_{grad} as well as the gradiometer baseline b_{grad} are $d_{\text{grad}} = b_{\text{grad}} = 42\,\text{mm}$, respectively. The DC resistance at room temperature is $R_{\text{grad,DC}} = 108\,\Omega$. Using equation (A.4), the effective area is found to be $A_{\text{eff}} = 5.4\,\text{mm}^2$. The system transfer function $V_{\Phi,\text{sys}}$ was found to be $V_{\Phi,\text{sys}} = 0.44\,\text{V}/\Phi_0$. Even though a first-order gradiometric pickup coil has also been realized ($d_{\text{grad}} = b_{\text{grad}} = 60\,\text{mm}$), the presented measurements where performed only using the second-order gradiometer due to its superior noise suppression.

5.6. Magnetic shielding

To shield the SQUID sensor and the sample from low frequency magnetic fields (e.g. magnetic fields originating from the moving elevator $\approx 10\,\text{m}$ from the setup or from quasi static magnetic fields like the earth's magnetic field), the coil system and the low noise helium dewar containing the SCS are submerged in a μ-metal barrel. The μ-metal barrel is an item on loan from the PTB in Berlin, department 8.2 biosignals. It has a wall thickness of $d_\mu = 2\,\text{mm}$, a height $h_\mu = 140\,\text{cm}$ and an inner diameter $\varnothing_\mu = 780\,\text{mm}$. μ-metal is an alloy composed mainly of nickel and iron, however additions of copper, chromium and molybdenum are quite common. Unfortunately, the exact μ-metal alloy composition is not known, thus the permeability, its frequency dependence and resulting shielding factors are unknown. Additionally, the static field within the barrel is also determined by the previous history of the barrel. It increases with increasing shielding factor and is determined by the magnetization of the μ-metal. A shielding factor of 500 for low frequencies $f < 100\,\text{Hz}$ and quasi static magnetic fields for the single μ-metal layer was estimated [Koc16].
Due to the close vicinity of the μ-metal walls to the pickup loop, depending on the used pickup coil configuration, severe additional noise components can be expected. Since the μ-metal barrel is at a temperature $T = 300\,\text{K}$, the motion of thermally agitated electric charges in the shielding itself produce Nyquist noise. The resulting power spectrum density of the thermal magnetic flux density noise at the distance z above the conductor (i.e. the

μ-metal wall) with the thickness d_μ ($d_\mu << z$) and the electrical conductivity σ can be approximated using the formula [BDK+07]

$$S_B = \frac{\mu_0^2 \, k_B \, T \, \sigma \, d_\mu}{8 \, \pi \, z^2} \Bigg/ 1 + \left(\frac{2 \, f}{\pi \, f_c} \right)^2 \tag{5.7}$$

with $f_c = 1/(4\mu_0 \sigma z d_\mu)$ and $\sigma = 1.82 \times 10^6 \, \mathrm{S/m}$ [Ant15]. It can be seen

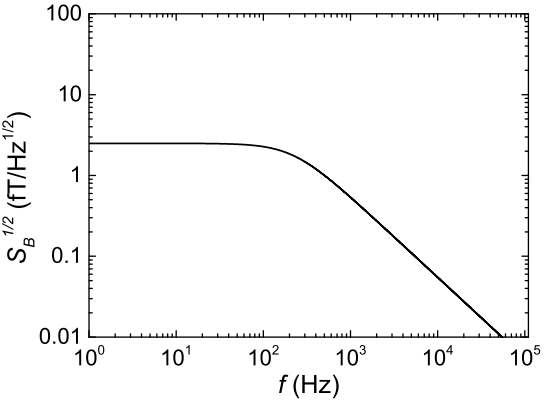

Figure 5.14.: Magnetic field noise estimate originating from the μ-metal barrel.

in Fig. 5.14 that the field noise contribution of the μ-metal barrel is $S_{B,\mu}^{1/2} = 2.5 \, \mathrm{fT/Hz^{1/2}}$, however it cuts off at $f_{-3dB} = 230 \, \mathrm{Hz}$. Since a gradiometric pickup coil is used, this contribution should be canceled out and can be neglected in the present setup, however it has to be taken into account if magnetometer pickup coils will be employed in future experiments. Another problem is the close vicinity of the gradient coils to the μ-metal walls. When fast gradient pulses are run, eddy currents will be induced in the μ-metal. The eddy currents can have long decay times thus interfering with the experimentally applied magnetic fields. A solution to this problem would be the use of a shielding chamber consisting of μ-meta,l since here the coil-wall-distance can be increased drastically.

5.7. pH_2 Generator

To perform NMR experiments using hyperpolarized contrast agents, the experiment ideally should be supplied with $\approx 100\%$ enriched pH_2 to maximize the signal enhancement. Fig. 5.15 shows the oH_2/pH_2 equilibrium composition for a given temperature [WSB48]. A high conversion rate thus can be obtained when the oH_2 will be cooled to cryogenic temperatures. For this purpose a pH_2 generator has been developed by C. Back that allows for convenient pH_2 production in a laboratory environment. Various pH_2 generator designs are suggested in literature [JCK02, HKS+14] or are even commercially available [Bru17a]. All generator implementations employ a cryo cooled paramagnetic catalyst that gets in contact with oH_2. The generator layout follows the design of Juarez et al. [JCK02]. Figure 5.16 shows the schematic layout of the pH_2 generator.

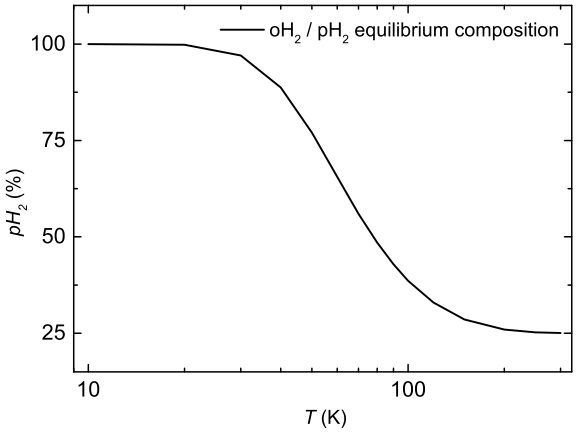

Figure 5.15.: oH_2/pH_2 equilibrium composition for a given temperature [WSB48]

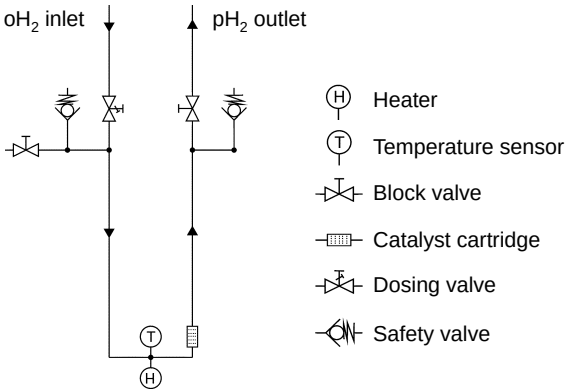

Figure 5.16.: Schematic layout the dip stick implementation of the pH_2 generator.

It is designed as a dip stick which can be flanged (flange type: KF25) and immersed into a liquid helium transport vessel. At the oH_2 inlet a precision dosing valve is mounted (Parcom M6A-H1L-V-SS-TC [Par17]) for gas flow regulation. At the outlet of the generated pH_2 a block valve is mounted (cf. Fig. 5.16) that seals the generator air-tight when not in use. The catalyst is housed in a cartridge located at the bottom of the stick in the outlet pipe. A temperature sensor and a heater resistor are located close to the catalyst cartridge. Two safety valves, one in the inlet branch and one in the outlet branch, ensure a save operation. A block valve connected to the inlet pipe allows for convenient evacuation of the generator. A technical drawing of the dip stick implementation can be seen in Fig. 5.17. The riser pipe consists of two stainless steel pipes nested into each other ($\varnothing_{\text{inner}} = 12\,\text{mm}$ and a wall thickness $d_{\text{inner}} = 0.25\,\text{mm}$ as well as $\varnothing_{\text{outer}} = 18\,\text{mm}$ and $d_{\text{outer}} = 0.5\,\text{mm}$). At the lower end of the inner pipe (i.e. the start of the outlet pipe), a cartridge made of brass is screw mounted. The cartridge has a volume of $\approx V_{\text{cat}} = 3\,\text{cm}^3$ and houses the catalyst granulate (Iron(III)Oxide hydrate, mesh size $30 - 50\,\mu\text{m}$, Sigma-Aldrich 371254-50G [Sig17]). The bottom end is perforated by 4 holes ($\varnothing = 3\,\text{mm}$) which allow the oH_2 to enter the cartridge. The holes are covered by a metal mesh to prevent the catalyst granulate from pouring out of the cartridge. The cartridge is nested in a cup made of brass that is screwed onto the outer riser pipe.

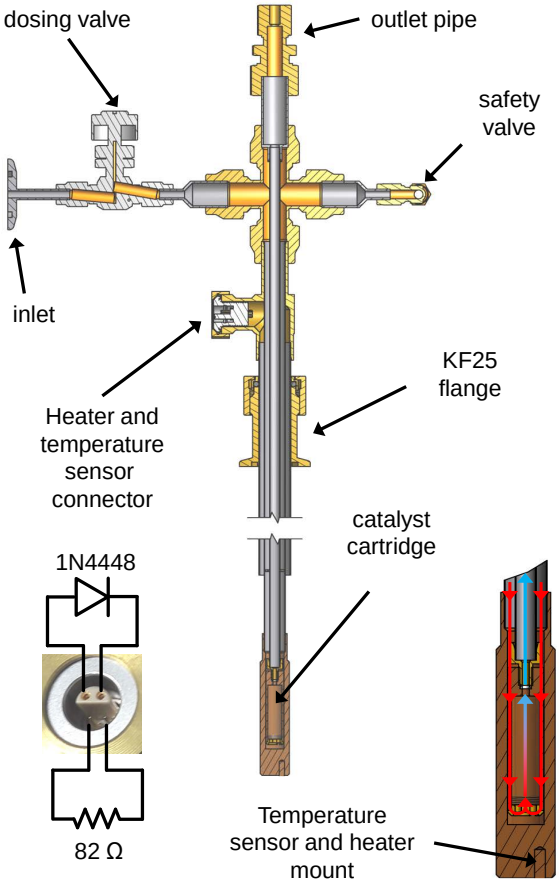

Figure 5.17.: Technical drawing of the pH_2 generator. The zoomed section on the bottom right shows the catalyst cartridge. The inflowing oH_2 (red) passes the cartridge and subsequently enters it from the bottom. Within the cartridge, the oH_2 gets converted and leaves as pH_2 (blue).

Between cartridge and cup there is a small gap which allows oH_2 gas to pass the cartridge and enter it by the bottom holes. The cooled, converted gas is streaming upwards in the inner riser pipe, thereby cooling the pipe which subsequently cools in inflowing oH_2 (cf. the bottom right

part of Fig. 5.17. Thereby the introduced heat due to the inflowing oH_2 is minimized. A temperature diode (standard 1N4448 diode, calibrated by C. Back) and a heater resistor are glued (glue used: GE Varnish VGE7031 [CMR17]) into the bottom of the cup covering the cartridge. The heater and the temperature diode are connected to a Lemo plug socket (type Lemo HGP.1S.306.CLLSV) by enameled copper wire, located right below the oH_2 inlet (cf. Fig. 5.17). The catalyst temperature is monitored and controlled by a home-made temperature controller unit.
The conversion efficiency of the generator was determined by a home-made thermal conductivity detector (TCD) (built from a reworked standard light bulb, thermally insulated using Armaflex) in combination with a prototype pH_2 generator (designed and built by the institute of inorganic chemistry of the University of Tübingen, not presented in this work) which used activated charcoal as catalyst operated at $T = 77\,\mathrm{K}$. The prototype pH_2 generator was used for the reference measurement of the TCD since at $T = 77\,\mathrm{K}$ the oH_2/pH_2 equilibrium composition is 50.2%.

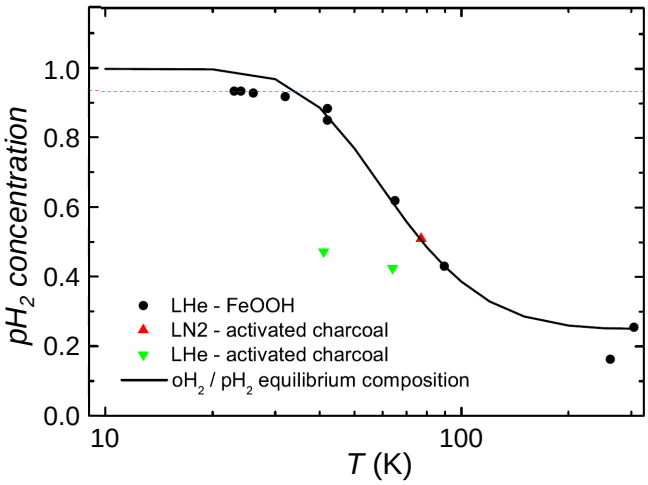

Figure 5.18.: Temperature dependent conversion efficiency of the build pH_2 generator for the two catalysts used. The Iron(III)Oxide hydrate catalyst achieved an pH_2 concentration above 90%, while the activated charcoal only reached $\approx 50\%$.

The reference measurement was performed at a H_2 flow rate of $dV/dt = 1.5\,l/h$. By having an activated charcoal volume of $V_{cat} \approx 500\,cm^3$, a H_2-catalyst contact time of $t_{contact} = 20\,min$ was achieved. Assuming, that after 20 min contact time the conversion was saturated, the voltage output of the TCD was set as the reference value for oH_2/pH_2 of 50.2%. Subsequently, the pH_2 generator described above was characterized by operating it with the same flow rate as the reference measurement at various temperatures while acquiring the TCD voltage output. By fitting the resulting data points to the oH_2/pH_2 equilibrium composition curve using the reference measurement, Fig. 5.18 was received. Fig. 5.18 indicates a maximum pH_2 concentration of 93.6% for the Iron(III)Oxide hydrate catalyst while activated charcoal only achieved a pH_2 concentration of 48%. Hövener et al. also reported a much higher conversion efficiency after replacing activated charcoal with Iron(III)Oxide hydrate [HKS+14]. The pH_2 concentration was not maximized any further by means of larger Iron(III)Oxide hydrate catalyst volumes. During measurements the typical flow rate was $dV/dt = 1.2 - 1.5\,l/h$, thus the pH_2 concentration was at least 90%.

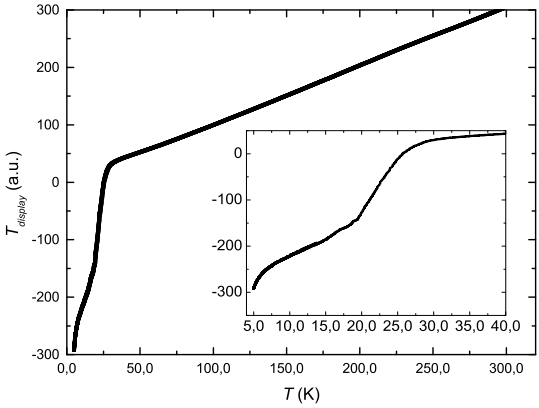

Figure 5.19.: Temperature response of the $1N4448$ diode, showing a very linear temperature response over a wide temperature range. At $T \approx 30\,K$ the diode leaves the linear temperature response regime and the forward voltage increases drastically when lowering the temperature any further.

An important note for the operation of the pH_2 generator is the fact that the temperature control unit is not controlled by a microcontroller but it is built completely using analog electronics. Therefore the temperature diode forward voltage is not calibrated to actual temperature readings. The display used for showing the target temperature and the current temperature, respectively, shows the scaled forward voltage drop across the temperature diode. While the $1N4448$ diode used has a very linear temperature response over a wide temperature range where the temperature reading coincides with the actual temperature (cf. Fig. 5.19), at $T \approx 30\,\mathrm{K}$ the diode leaves the linear temperature response regime and the forward voltage increases drastically when lowering the temperature any further. This leads to negative temperature readings for $T < 30\,\mathrm{K}$ (cf. inset of Fig. 5.19). For this reason, the ordinate in Fig. 5.19 has the dimension of arbitrary units. Maximum conversion rates and safe operation of the generator can be expected for *current temperature* reading (and therefore temperature setpoints) at the temperature control unit between 30 and −65. To ensure that the hydrogen stays in the gas phase, the *current temperature* reading of the temperature control unit must not become smaller than −85.

5.8. Magnetic field noise

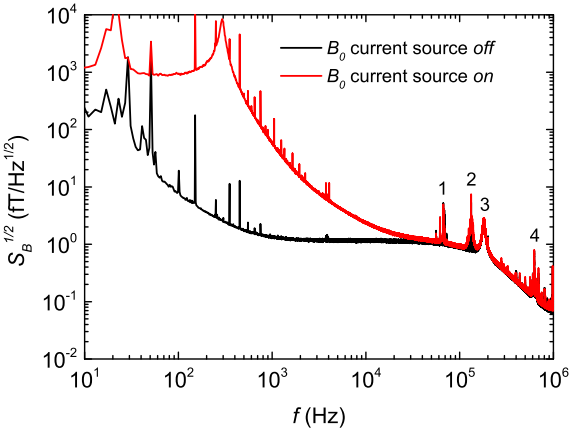

Figure 5.20.: Magnetic field noise $S_B^{1/2}$ performance of the coil system. The black curve shows the pure noise floor with all current sources turned off. The red curve shows the noise floor during measurements, where the B_0 current source is running constantly. The numbered peaks refer to the peaks reproduced by an equivalent circuit model of the input circuitry that aims to understand the roll-off of the spectrum (see below).

The magnetic field noise performance of the coil system, submerged into the μ-metal shielding and surrounded by a RF shielding chamber, can be seen in Fig. 5.20. The black curve shows the pure noise floor with all current sources turned off, which yields a white magnetic field noise level $S_B^{1/2}(B_0\,\text{off}) = 1.15\,\text{fT}/\text{Hz}^{1/2}$. Once the B_0 current source is turned on, the noise level is increased drastically in the low-frequency region of the spectrum (red curve) and practically no white noise region is present anymore. The noise level in the frequency range of interest ($f > 5\,\text{kHz}$ increases slightly but is still below $S_B^{1/2}(B_0\,\text{on}) = 5\,\text{fT}/\text{Hz}^{1/2}$. The red spectrum also shows very large peaks at $f = 25, 50, 100, 300\,\text{Hz}$ which can be attributed to the three-phase mains power connection of the B_0 current source and corresponding harmonics. Even though there are large peaks

at $f \approx 50\,\mathrm{kHz}$ and $f \approx 100\,\mathrm{kHz}$ the measurements are not disturbed since the Larmor frequency ω_0 can be tuned to peak-free regions of the spectrum due to the use of a SCS. The spectrum rolls off at $f_{-3\mathrm{dB}} \approx 160\,\mathrm{kHz}$, where it exhibits a resonant peak. Both the roll-off and the resonance peak are caused by the very complex LCR-network formed by L_p, L_{in} and its RC shunts, the inductance L_{tp} and the capacitance C_{tp} of the twisted pair cable used to wound L_{in} as well as stray inductance L_{stray} and capacitance C_{stray} of the superconducting screw terminals including the niobium bonds.

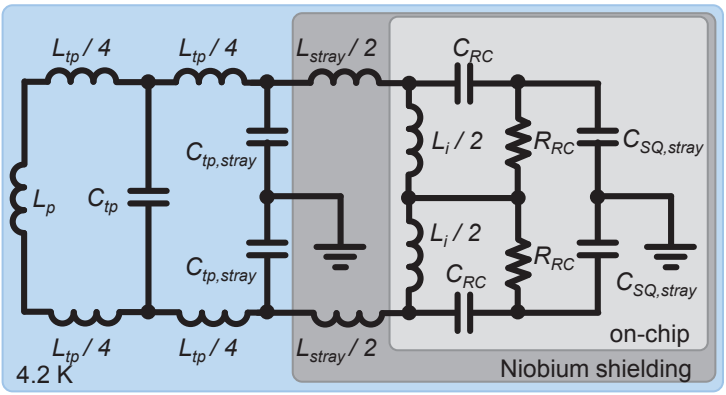

Figure 5.21.: Equivalent circuit used to model the input circuit.

The derived equivalent circuit model of the complete input circuit can be seen in Fig. 5.21. It facilitates parasitic inductances of the pickup coils twisted pair wire L_{tp} and a corresponding parasitic capacitance between the wires C_{tp}, stray capacitances of the twisted pair wires to the environment (the environment is modeled as ground) $C_{\mathrm{tp,stray}}$, stray inductances L_{stray} caused by the wire screw terminals on the chip carrier as well as parasitic stray capacitance $C_{\mathrm{SQ,stray}}$ of the SQUID chip to the environment. It was not possible to reproduce the positions of $f_{-3\mathrm{dB}}$, f_{res} and the shape of the transfer function of the system exactly since L_{tp}, L_{stray}, C_{tp}, $C_{\mathrm{tp,stray}}$, and $C_{\mathrm{SQ,stray}}$ are hard to estimate. However, when inserting feasible quantities into the equivalent circuit and simulate its transfer function, it qualitatively reproduces four distinct peaks that can be seen in the recorded spectrum and it also leads to a roll-off behavior (cf. Fig. 5.22). The slight fall-off of

the transfer function at low frequencies could not be observed in recorded spectrum due to the presence of $1/f$ noise.

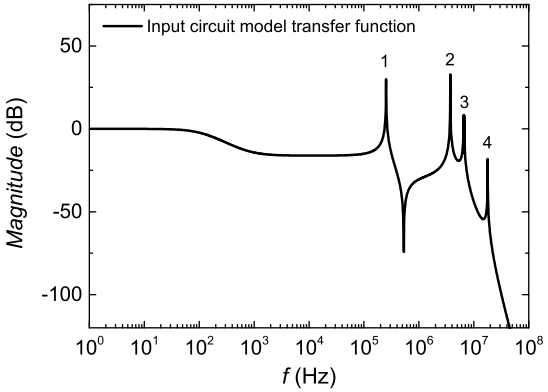

Figure 5.22.: Transfer function of the equivalent circuit model of the input circuit. Values used: $L_p = 900\,\mathrm{nH}$, $L_{\mathrm{tp}}/4 = 10\,\mathrm{nH}$, $L_{\mathrm{stray}}/2 = 10\,\mathrm{nH}$, $L_{\mathrm{in}}/2 = 200\,\mathrm{nH}$, $C_{\mathrm{tp}} = 1200\,\mathrm{nF}$, $C_{\mathrm{tp,stray}} = 50\,\mathrm{nF}$, $C_{\mathrm{RC}} = 50\,\mathrm{pF}$, $C_{\mathrm{SQ,stray}} = 10\,\mathrm{nF}$, $R_{\mathrm{RC}} = 100\,\Omega$.

5.9. First NMR signals

The first measurements have been performed on a tap water sample in combination with the large first-order gradiometric pickup coil. An ordinary lockable plastic cup with a volume of $V_{\text{cup}} = 150\,\text{ml}$ was chosen as sample container. Since the system was completely unknown a large sample volume was chosen to ensure a relatively large signal. Fig. 5.23(a) shows one of the first measured NMR peaks recorded using this setup at $|\vec{B}_0| = 2\,\text{mT}$ and 100 averages and took 7 minutes. The line width, with a FWHM $<$ 40 Hz is relatively broad. However, this can most likely be attributed to the size of the used sample container since its physical size reaches out of the very homogenous $\vec{B}_0$ field region. A good benchmark for comparing peaks is the signal-to-noise ratio (SNR). It is defined by

$$\text{SNR} = \frac{\text{peak height}}{\frac{1}{\Delta f}\int_{\Delta f} S_{B,w}^{1/2}}, \tag{5.8}$$

where Δf is the width of a chosen white frequency band in the vicinity of the peak under investigation.

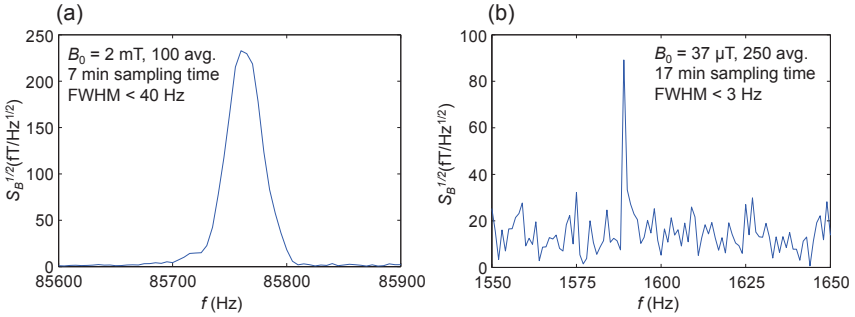

Figure 5.23.: (a) First NMR signals measured with the home made NMR system. The signal was recorded using a FID sequence. The FWHM $<$ 40 Hz at $|\vec{B}_0| = 2\,\text{mT}$. (b) shows a signal recorded at $|\vec{B}_0| = 37\,\mu\text{T}$. The line width drastically reduced to $<$ 3 Hz.

When moving to smaller $\vec{B}_0$ fields (cf. Fig. 5.23(b)) the line width reduces drastically, here to FWHM $<$ 3 Hz. The SNR, however, also reduces

and it needed 250 averages (and 17 minutes) to clearly distinct the signal from the noise. The reasons therefore are the reduced sample polarization and the elevated noise floor in the specific frequency range of the spectrum.

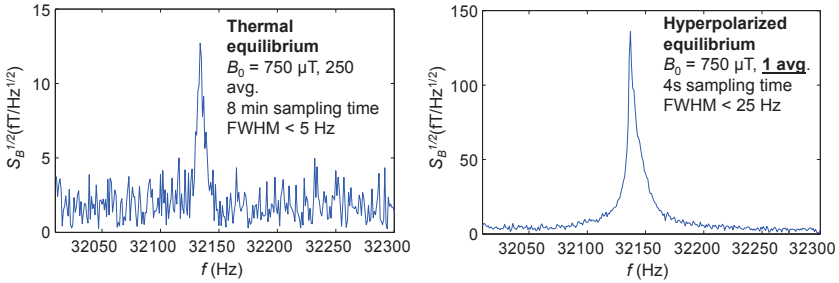

Figure 5.24.: Comparison of thermal equilibrium polarization (a) and the corresponding hyperpolarized equilibrium polarization (b) of pyridine. The hyperpolarized signal was acquired using one single measurement only.

When moving to hyperpolarized samples, the situation changes enormously. Figure 5.24 shows results of a pyridine sample soluted in methanol in combination with 2 mmol of the iridium based IMes catalyst [HSL$^+$13], comparing the thermally polarized (a) and hyperpolarized sample (b) at $|\vec{B}_0| = 750\,\mu$T. The data have been acquired using a FID sequence. The sample was not located in the sample container described above since it was just a prove of principle measurement. It was filled into a syringe which subsequently was glued to the dewar using scotch tape. To supply pH_2 a thin hose was squeezed into the syringe through a small hole drilled into the piston of the syringe. Even though the experimental conditions where rather undefined, the results are quite impressive. While the thermally polarized sample shows a very low SNR ≈ 3 after 250 averages, the hyperpolarized pyridine shows a SNR ≈ 30 after only 1 average. The FWHM of the hyperpolarized sample is increased by a factor of 5 compared to the thermally polarized measurement. The reason is most likely, again, the physical size of the syringe and thus the broad distribution of the sample within the $\vec{B}_0$ field.

Combining hyperpolarization with prepolarization of the sample even further increases the signal (cf. Fig. 5.25, solenoid $\vec{B}_P$ coil used). Here,

a pyridine sample of the same mixture as above in combination with the presented sample container was measured. The sample prepolarization was performed using the first implementation of a prepolarization coil. The data have been recorded at $|\vec{B}_0| = 50\,\mu\mathrm{T}$ using a spin echo sequence with preceding prepolarization pulse $\vec{B}_P = 8\,\mathrm{mT}$.

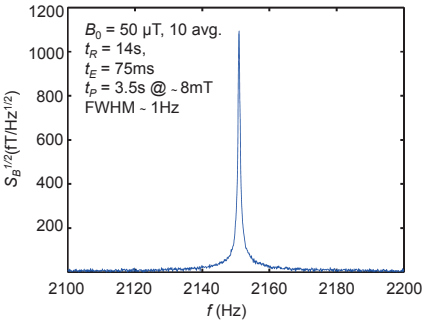

Figure 5.25.: Hyperpolarization combined with prepolarization

Due to the very low $\vec{B}_0$ field strength of $|\vec{B}_0| = 50\,\mu\mathrm{T}$, the line width becomes very narrow. In the presented measurement, the FWHM $\approx 1\,\mathrm{Hz}$ and a very high SNR ≈ 100 could be achieved.

5.10. Discussion

After complete set up, the system shows very promising results. It exhibits a very low white magnetic field noise floor $S_B^{1/2} = 1.15\,\mathrm{fT/Hz^{1/2}}$ which is comparable to already existing systems [MHM+06]. In combination with the SQUID based magnetic field sensor, a very sensitive detector has been realized which is able to detect NMR signals of water samples employing $\vec{B}_0$ fields down to $|\vec{B}_0| = 37\,\mu\mathrm{T}$ (which is smaller than the earth magnetic field). First measurements using hyperpolarized pyridine show a signal amplification of ≈ 200 compared to thermally polarized pyridine, which is in compliance with reports by other groups [HSL+13, HKS+14]. The gradient coils have not been characterized or used due to the lack of VCCS, however during the writing this thesis, the VCCS listed above have been arrived and show promising results [Ant17].

6 | Results

After successfully setting up the system and performing a full characterization, measurements of various target molecule systems were performed. The sample container was placed in the iso center of the coil system (cf. Fig. 5.7(b)) and subsequently connected to the pH_2 generator. The substrate solution evaporation rate was increased drastically by the bubbling pH_2. During a full characterization session of one type of target molecule (measurement time $\approx 2-3\,\mathrm{h}$) with a pH_2 flow rate of $\approx 1.5\,\mathrm{l/h}$, roughly $3-4\,\mathrm{ml}$ of the solution evaporated. Therefore the collecting basin of the sample container (cf. chapter 5.3) was typically filled with additional $5-6\,\mathrm{ml}$ of substrate solution. While measurements were performed, the sample container was in direct contact with the dewar bottom (which is at room temperature), thus the sample temperature was assumed to be at room temperature and constant over time. For signal acquisition a FID sequence with preceding, variable prepolarization amplitude $\vec{B}_P$ and time $t_{\vec{B}_P}$ was used (cf. Fig. 6.1). To investigate the hyperpolarizability of ^{1}H and ^{19}F atoms under ULF conditions, 3,5-bis(trifluoromethyl)pyridine, ethyl-5-fluoronicotinic acid and 3-fluoropyridine were used as target molecules. They were chosen because they showed promising results using the SABRE technique in combination with a high field NMR system. To transfer the spin order from pH_2 to the target molecules, the iridium based catalyst [Ir(COD)(IMes)(Cl)] was employed [CAA$^+$11] for all target molecules. The catalyst and the target molecules were soluted in methanol. The solution prepared for all three different target molecules consisted of 7 mg [Ir(COD)(IMes)(Cl)] and 0.23 mmol of the fluorinated pyridine derivative (i.e. the targets), soluted in 10 ml methanol and they were not degassed.
The readout magnetic field $\vec{B}_0$ was set to $|\vec{B}_0| = 150\,\mu\mathrm{T}$, which leads

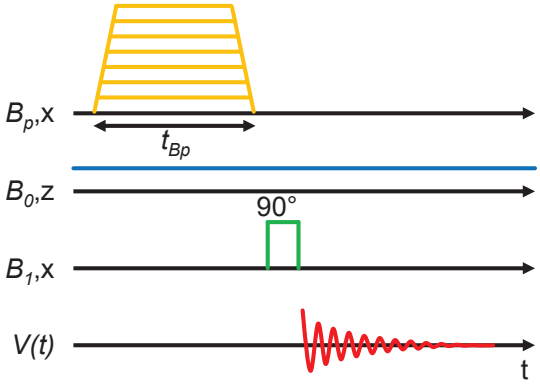

Figure 6.1.: FID sequence with preceeding prepolarization $\vec{B}_P$ for the time $t_{\vec{B}_P}$

to $f_L(^1\mathrm{H}) = \omega_L/2\pi = 6140\,\mathrm{Hz}$ for $^1\mathrm{H}$ ($\gamma_{^1\mathrm{H}}/2\pi = 42.576\,\mathrm{MHz\,T^{-1}}$) and $f_L(^{19}\mathrm{F}) = 5770\,\mathrm{Hz}$ for $^{19}\mathrm{F}$ ($\gamma_{^{19}\mathrm{F}}/2\pi = 40.053\,\mathrm{MHz\,T^{-1}}$). $|\vec{B}_0| = 150\,\mu\mathrm{T}$ was chosen because the noise spectra was not deteriorated by noise peaks originating from external noise sources in this frequency range. Even though the methanol used to solute all substances is MR active, the resulting signal is much smaller than the signal received from hyperpolarized target molecules. This was determined by measuring NMR signals from the solution with no pH_2. Therefore it was not necessary to use deuterated methanol. Between the measurement sessions of the individual target molecules, the whole tubing system of the sample container was cleaned and flushed carefully using ethanol and methanol.

6.1. Magnetic field dependence of the SABRE efficiency

To investigate the influence of the magnetic field strength on the signal enhancement of SABRE, the prepolarization field $\vec{B}_P$ was employed. The amplitude of $\vec{B}_P$ was swept between $|\vec{B}_{P,\mathrm{min}}| = 144\,\mu\mathrm{T}$ ($\approx |\vec{B}_0|$) and $|\vec{B}_{P,\mathrm{max}}| = 10.3\,\mathrm{mT}$. The prepolarization time $t_{\vec{B}_P}$ was varied (cf. table 6.1), depending on the nuclei of interest due to different T_1 times. After

performing the FID sequence (single frequency excitation), the area-under-peak was determined. Therefore, the recorded voltage time trace $V(t)$ will be Fourier transformed. Using the system transfer function $V_{\Phi,\mathrm{sys}}$, this leads to the magnetic field noise power spectrum S_B with the dimension T^2/Hz. Integrating S_B in the frequency range $f_L \pm \delta f$, with $\delta f = 10\,\mathrm{Hz}$ and subsequent extracting of the square root yields the area-under-peak in dimensions of $\mathrm{T}/\mathrm{Hz}^{1/2}$. Subsequently, the measurement was repeated n_{avg} times, while waiting for t_R between subsequent measurements. Table 6.1 summarizes the used parameters for the area-under-peak investigation. The results are shown in Fig. 6.2.

Table 6.1.: Sequence parameters used for the $\vec{B}_P$ sweep

Substance	n_{avg}	t_R (s)	$t_{\vec{B}_P}$ (s)	$\lvert\vec{B}_P\rvert$ (mT)	$f(\vec{B}_1)$ (Hz)	Nucleus
Ethyl-5-fluoronicotinic acid	5	6.5	2	0.144 - 10.3	5775	^{19}F
3-Fluoro-pyridine	5	6.5	2	0.144 - 10.3	5775	^{19}F
3,5-Bis (trifluoromethyl) pyridine	50	3.5	2	0.144 - 10.3	5775	^{19}F
Ethyl-5-fluoronicotinic acid	5	8.5	4	0.144 - 10.3	6140	^{1}H
3-Fluoro-pyridine	5	8.5	4	0.144 - 10.3	6140	^{1}H
3,5-Bis (trifluoromethyl) pyridine	5	8.5	4	0.144 - 10.3	6140	^{1}H

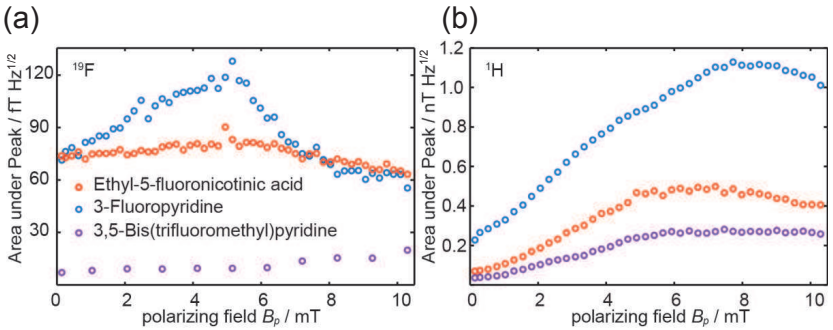

Figure 6.2.: Integrated area-under-peak signal vs. $|\vec{B}_P|$ for the three different target molecules for ^{19}F (a) and ^{1}H (b).

The resulting signal amplification indicates a $\vec{B}_P$ amplitude dependence which varies in intensity depending on the both the target molecule and investigated nuclei. Qualitatively, almost all substances show an increased signal for increasing $\vec{B}_P$ amplitude until a maximum is reached. Further increasing of $\vec{B}_P$ yields smaller signal amplification. The maximum amplification varies drastically, not only between the different target molecules but also for ^{19}F and ^{1}H of each individual target molecules. This also holds for the $\vec{B}_P$ amplitude yielding maximum signal amplification. The signal arising from Ethyl-5-fluoronicotinic acid's single ^{19}F shows only a small $\vec{B}_P$ dependence compared to the corresponding ^{1}H signal (cf. red circles). Of all investigated substances, 3-fluoropyridine (blue circles) shows the largest $\vec{B}_P$ dependence both for ^{19}F and ^{1}H, while 3,5-Bis(trifluoromethyl)pyridine shows a very unpronounced effect. Interestingly, the ^{19}F nuclei of 3,5-Bis(trifluoromethyl)pyridine shows practically no $\vec{B}_P$ dependence. The signal increases slightly, however, the reason for this can be attributed to increasing noise for increasing $\vec{B}_P$ fields. Possible reasons for the elevated noise are Joule heating during the prepolarization process, heating up the coil wire drastically. This leads to an increased current and voltage noise that translates directly into magnetic field noise. This applies to all samples, however it is only visible for 3,5-Bis(trifluoromethyl)pyridine due to the overall small area-under-peak.
More information can be extracted by plotting the recorded spectra in the close vicinity to f_L as a function of $\vec{B}_P$ (c.f. Fig. 6.3, 6.4 and 6.5). The spec-

tra reveal various peaks which are owed to J-coupling. For 3-fluoropyridine

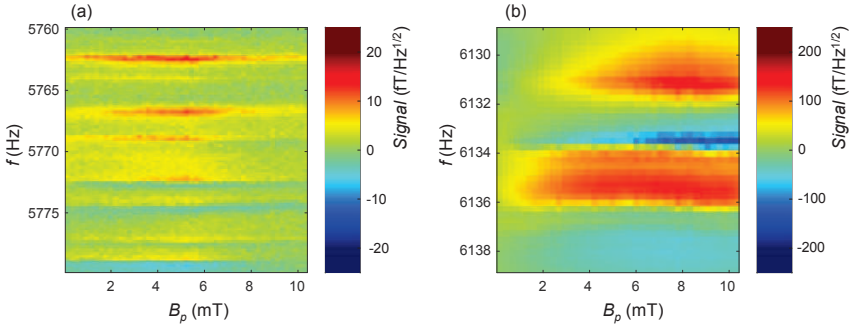

Figure 6.3.: Spectra of 3-fluoropyridine as a function of $\vec{B}_P$ for ^{19}F (a) and ^{1}H (b).

all signal amplitudes of all resonances correlate which means that they roughly have the same $\vec{B}_P$ dependence with respect to their peak amplitude (cf. Fig. 6.3(a) for ^{19}F and (b) for ^{1}H). This behavior also holds for ^{1}H of 3,5-bis(trifluoromethyl)pyridine (cf. Fig. 6.4(b)). The ^{19}F peak seems

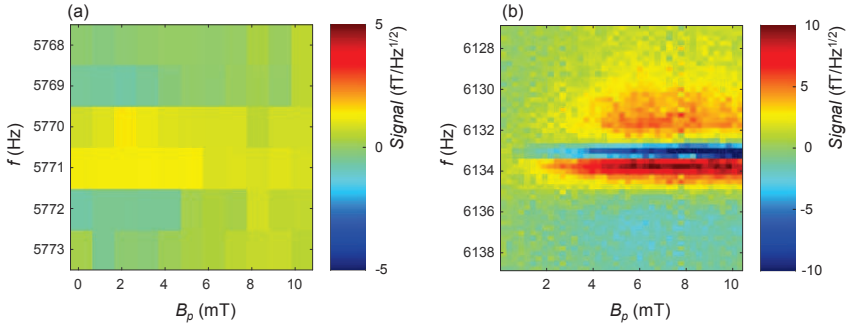

Figure 6.4.: Spectra of 3,5-bis(trifluoromethyl)pyridine as a function of $\vec{B}_P$ for ^{19}F (a) and ^{1}H (b). In (a), a small peak is visible for low $\vec{B}_P$ amplitudes which gets burried within the noise floor for increasing $\vec{B}_P$ amplitudes.

to stay at a constant value. For low $\vec{B}_P$ amplitudes, it can be distinct from the noise floor. However due to the increased noise floor level for higher B_p

values, the small peak gets burried in the noise. For ethyl-5-fluoronicotinic acid the correlation between the peaks only holds for the ^{1}H peaks. The wave-like structure in Fig. 6.5(b) is caused by a $\vec{B}_0$ drift caused by a output current drift of the $\vec{B}_0$ coil current source. While for ^{19}F the peaks below 5771 Hz and between $5773 - 5776$ Hz seem to correlate (cf. Fig. 6.5(a)), the peak amplitudes at 5772 Hz (between the dashed lines) and 5778 Hz (between the dotted lines) exhibit a sign change that can be attributed to a phase change of the signal.

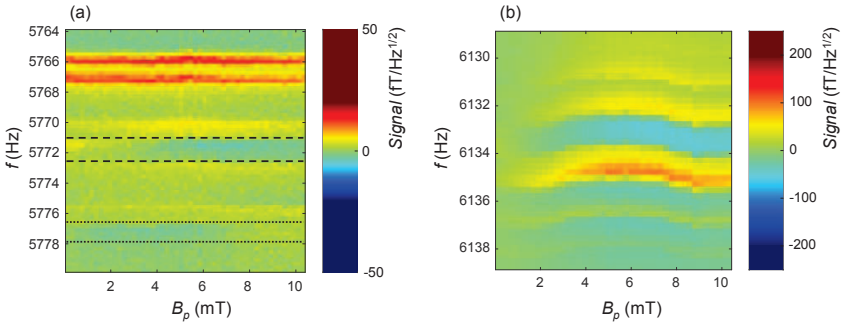

Figure 6.5.: ^{19}F (a) and ^{1}H spectra of ethyl-5-fluoronicotinic acid as a function of $\vec{B}_P$. While all peaks are positive below $|\vec{B}_P| = 1$ mT, the peaks at 5772 Hz and 5777 Hz experience a sign change that can be attributed to a phase change.

6.2. Dependence of the hyperpolarization time $t_{\vec{B}_P}$ on the SABRE efficiency

The next set of measurements investigates the influence of the hyperpolarization time $t_{\vec{B}_P}$ on the SABRE induced signal enhancement. Therefore, for each individual target molecule and the two corresponding nuclei, respectively, the $\vec{B}_P$ amplitudes were fixed to the individual values that obtained the maximum signal enhancement in the previous section. Subsequently, $t_{\vec{B}_P}$ was varied in $\delta t_{\vec{B}_P} = 1$ s steps. Table 6.2 summarizes the parameters of the measurement session. Figure 6.6 shows the yielded data. The individual data sets have been fitted using the exponential saturation

Table 6.2.: Sequence parameters used for the $t_{\vec{B}_P}$ and t_R sweeps

Substance	n_{avg}	t_R (s)	$t_{\vec{B}_P}$ (s)	$\vec{B}_P$ (mT)	$f(\vec{B}_1)$ (Hz)	Nucleus
Ethyl-5-fluoronicotinic acid	10	1.6 - 10.6	0 - 10	3.1	5775	^{19}F
3-Fluoro-pyridine	10	1.6 - 10.6	0 - 10	5.2	5775	^{19}F
3,5-Bis (trifluoromethyl) pyridine	25	1.6 - 10.6	1.5 - 10.5	0.144	5775	^{19}F
Ethyl-5-fluoronicotinic acid	10	1.6 - 10.6	0 - 10	6.2	6140	^{1}H
3-Fluoro-pyridine	10	1.6 - 10.6	0 - 10	7.7	6140	^{1}H
3,5-Bis (trifluoromethyl) pyridine	10	1.6 - 10.6	0 - 10	7.7	6140	^{1}H

function

$$M(t_{\vec{B}_P}) = M_{\text{HP}} \left(1 - \exp\left(-\frac{t_{\vec{B}_P} - t_0}{t_{\text{HP}}}\right)\right), \tag{6.1}$$

where $M(t_{\vec{B}_P})$ is the sample magnetization which is proportional to the area-under-peak, M_{HP} is the saturation magnetization corresponding to an infinite polarization time, t_{HP} is the magnetization build-up time and t_0 is a offset time needed to fit the data properly. t_{HP} of the individual substrates depends both on the longitudinal relaxation time T_1 (which depends on the $\vec{B}_P$ amplitude since in general T_1 is field dependent [Lev08]) and likewise on the hyperpolarization build-up time and is governed by the shorter time constant of both processes, since it is linked to a broader line width within the spectrum. The received fitting values of t_{HP} for ^{19}F and ^{1}H are presented in table 6.3. The results indicate, that the chemical surrounding can lead to variable t_{HP} for the investigated nu-

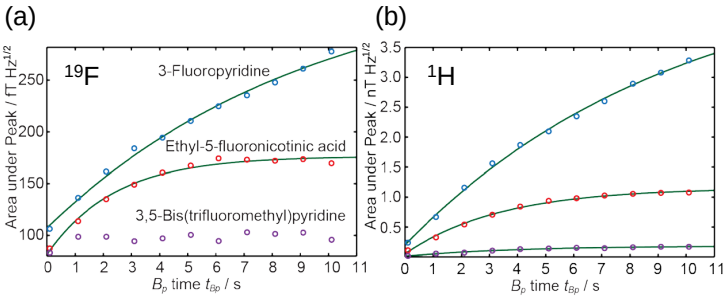

Figure 6.6.: Integrated area-under-peak signal vs. $t_{\vec{B}_P}$ for the three different target molecules (symbols) and fits of equation (6.1) (solid lines) is shown for ^{19}F (a) and ^{1}H (b).

Table 6.3.: Build-up time constants for the ^{19}F and ^{1}H of 3,5-bis(trifluoromethyl)pyridine, ethyl-5-fluoronicotinic acid and 3-fluoropyridine in the ULF regime.

Substance	Nucleus	t_{HP} (s)
Ethyl-5-fluoronicotinic acid	^{19}F	2.4 ± 0.5
3-fluoropyridine	^{19}F	9.4 ± 3.9
3,5-bis(trifluoromethyl)pyridine	^{19}F	-
Ethyl-5-fluoronicotinic acid	^{1}H	3.4 ± 0.5
3-fluoropyridine	^{1}H	9.7 ± 2.4
3,5-bis(trifluoromethyl)pyridine	^{1}H	3.4 ± 1.0

clei. 3-fluoropyridine shows for both ^{19}F and ^{1}H rather long hyperpolarization times which coincide clearly within the uncertainty of the fitting parameters. However, both other substances show a quite different behavior. $t_{\mathrm{HP}}(^{1}\mathrm{H})$ for both 3,5-bis(trifluoromethyl)pyridine and ethyl-5-fluoronicotinic acid is only approx. a third of 3-fluoropyridine's $t_{\mathrm{HP}}(^{1}\mathrm{H})$. With respect to the ^{19}F nucleus, $t_{\mathrm{HP}}(^{19}\mathrm{F})$ is, on the one hand, drastically shorter compared to $t_{\mathrm{HP}}(^{19}\mathrm{F})$ of 3-fluoropyridine. On the other hand, it is also shorter than $t_{\mathrm{HP}}(^{1}\mathrm{H})$ of the corresponding ^{1}H nucleus. While $t_{\mathrm{HP}}(^{19}\mathrm{F})$ of the ethyl-5-fluoronicotinic acid is approx. 1 s shorter than the corresponding $t_{\mathrm{HP}}(^{1}\mathrm{H})$, 3,5-bis(trifluoromethyl)pyridine's $t_{\mathrm{HP}}(^{19}\mathrm{F})$ was too short to achieve a suitable fit (cf. the purple circles in Fig. 6.6(a)).

6.3. Hyperpolarized high resolution spectra

Until now, for each target molecule and the corresponding nuclei the $\vec{B}_p$ amplitude and t_{HP} were determined, which will lead to the maximum signal enhancement. Therefore, it is now possible to record high resolution spectra that yield a maximum SNR. This allows to investigate the hyperpolarization mechanism by resolving the spectral peaks associated to J-coupling. To be able to discriminate hyperpolarization induced effects in the spectra from peaks arising from standard thermal equilibrium polarization simulations of the NMR spectra both for high and ultra-low fields have been performed.

Table 6.4.: Sequence parameters used for the acquisition of hyperpolarized high resolution spectra.

Substance	n_{avg}	t_R (s)	$t_{\vec{B}_P}$ (s)	$\lvert\vec{B}_P\rvert$ (mT)	$f(B_1)$ (Hz)	Nucleus
Ethyl-5-fluoronicotinic acid	50	9.5	9.5	0.144	5775	^{19}F
3-Fluoro-pyridine	50	9.5	4	5.2	5775	^{19}F
3,5-Bis (trifluoromethyl) pyridine	200	5.25	5.25	0.144	5775	^{19}F
Ethyl-5-fluoronicotinic acid	50	9.5	4	6.2	6140	^{1}H
3-Fluoro-pyridine	50	9.5	4	7.7	6140	^{1}H
3,5-Bis (trifluoromethyl) pyridine	100	10.1	5	7.7	6140	^{1}H

For simulations of high field spectra the software Bruker Topspin was used, while for the ultra-low field spectra the software package VeSPA was employed [Bru17b, VeS17]. The results of high field simulations have been

performed by M. Paumann of the University of Magdeburg and are not presented in this work.

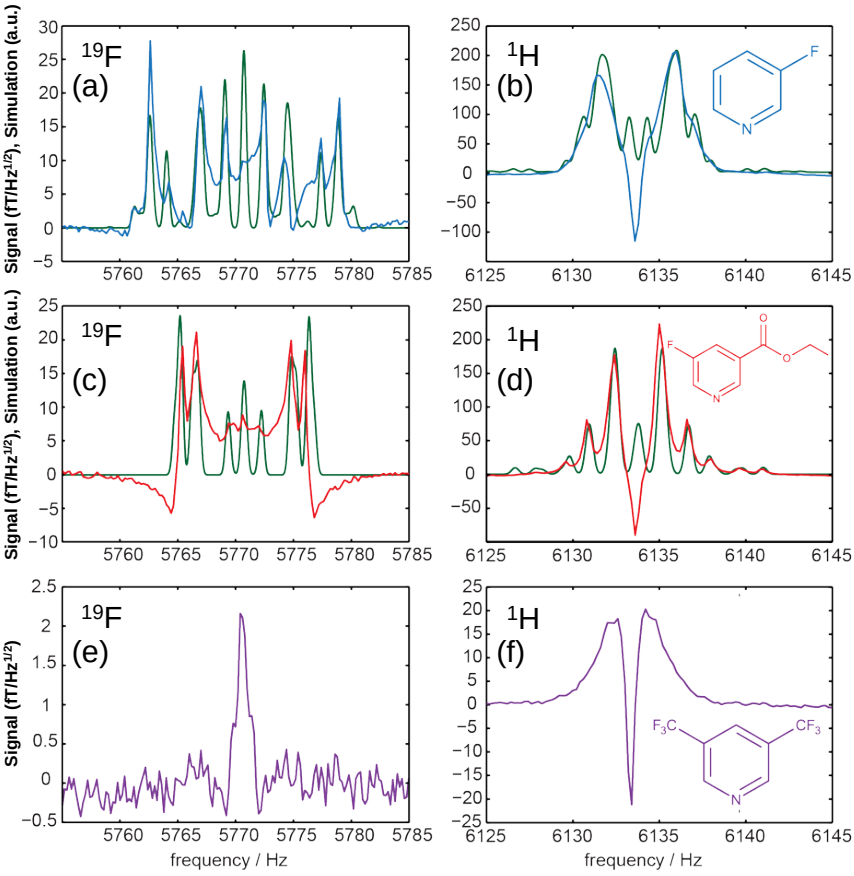

Figure 6.7.: Spectra of 3-fluoropyridine for ^{19}F (a) and for ^{1}H (b). Ethyl-5-fluoronicotinic acid is presented in (c) for ^{19}F and (d) for ^{1}H while the results for 3,5-bis(trifluoromethyl)pyridine can be seen in (e) for ^{19}F and (f) for ^{1}H. VeSPA low field simulation results are shown in green.

Additionally, the J-coupling constants of all three target molecules for both ^{19}F and ^{1}H, soluted in deuterated methanol, have been experimentally determined by means of high field spectra acquired at 7 T by M. Paumann. The parameters for the used FID sequence are summarized in table 6.4. To achieve a very high spectral resolution, the frequency resolution was set to $\Delta f = 0.125\,\mathrm{Hz}$. The high resolution spectra of all three target molecules for both ^{19}F and ^{1}H and the corresponding VeSPA based ultra-low field simulations are presented in Fig. 6.7. The simulation results are shown in green.
While for 3-fluoropyridine and ethyl-5-fluoronicotinic acid J-coupling resonances are clearly resolved, for 3,5-bis(trifluoromethyl)pyridine only single peaks are visible. The measured peak structure is in very good agreement with the thermal simulations. For 3-fluoropyridine in (a) the expected peak at 5770 Hz is split up into seven separate peaks. The splitting is caused by J-coupling between the five ^{1}H nuclei and the ^{19}F nucleus. The peak structure of the ^{1}H spectrum of 3-fluoropyridine (b) is centered around $f_{L,^1\mathrm{H}} = 6134\,\mathrm{Hz}$ which is dominated by ^{1}H-^{1}H coupling as well as ^{1}H-^{19}F coupling. Ethyl-5-fluoronicotinic in (c) exhibits the same qualitative behavior. The expected ^{19}F peak at 5770 Hz is split up into separate peaks, also caused by J-coupling between the ^{1}H nuclei and the ^{19}F nucleus. J-coupling can also be observed in the peak structure of the ^{1}H spectrum of ethyl-5-fluoronicotinic (d). As in (b), the expected ^{1}H signal around $f_{L,^1\mathrm{H}} = 6134\,\mathrm{Hz}$ is split up by ^{1}H-^{1}H coupling as well as ^{1}H-^{19}F coupling. Neither the ^{19}F spectra of 3,5-bis(trifluoromethyl)pyridine nor the ^{1}H signal show J-coupling at all. Although the effect of hyperpolarization has to be present, because no signal originating from unhyperpolarized ^{19}F can be detected at ultra-low fields, J-coupling seems not to be the only responsible hyperpolarization mechanism. Another interesting detail is the fact that all ^{1}H related main peaks exhibit an inverted signal as compared to the simulation. The inverted signal is most probably caused by hyperpolarized methanol. Finally, when a multi spectral B_1 pulse is applied to the hyperpolarized target, e.g. 3-fluoropyridine, that excites both the ^{19}F and the ^{1}H nuclei, the resulting spectrum shows resonance peaks of both nuclei (cf. Fig. 6.8). Such a measurement would not be possible using a conventional coil for the signal detection and demonstrates the superiority of a SQUID based current sensor.

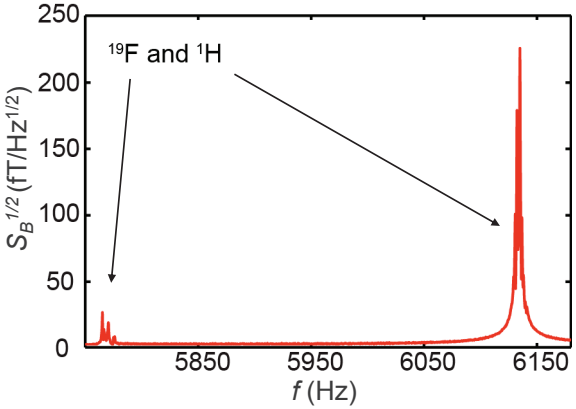

Figure 6.8.: Spectrum of 3-fluoropyridine when applying a multi spectral B_1 pulse. The SQUID based current sensor is clearly able to resolve both peaks originating from ^{19}F and the ^{1}H, respectively.

6.4. Discussion of the SABRE based measurements

The obtained data strongly underpin the potential of the hyperpolarization scheme SABRE in combination with a SQUID based readout scheme for multi-nuclear investigations in the ULF NMR regime. Low spin density samples, like the highly diluted solutions used, as well as low sensitivity nuclei like ^{19}F can be reliably detected using continuous hyperpolarization, which allows for repeating experiments various times and thereby leading to larger SNRs.

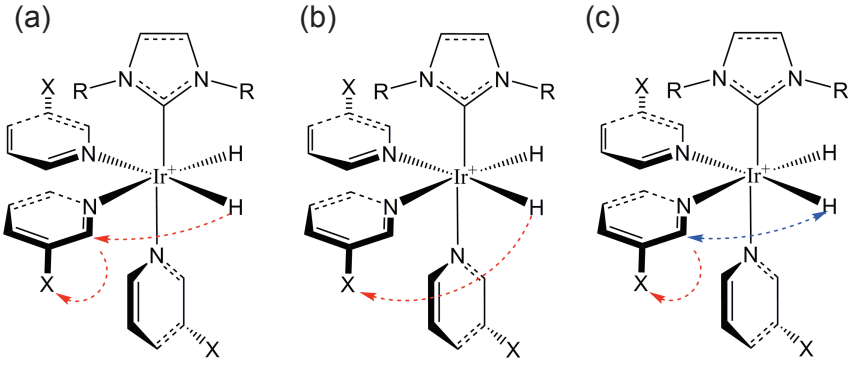

Figure 6.9.: Possible polarization transfer mechanisms to spin-1/2 heteronuclei of pyridine derivatives. (a) shows the indirect polarization transfer, where the polarization is transferred to a ^{1}H of the target molecule and subsequently a transfer to the corresponding heteronucleus X, e.g. ^{19}F. (b) illustrates the direct transfer, where the polarization is transferred directly to the corresponding heteronucleus X of the exchangeable target molecule. (c) shows the polarization transfer via ^{1}H exchange. ^{1}H of a pyridine target in ortho-position exchange during the SABRE reaction. This would also enable a direct polarization transfer path from polarized hydrogen atoms to the corresponding heteronucleus X of the target (e.g. ^{19}F).

The results also proof that J-coupling is not the only mechanism leading to hyperpolarization, thus hypothesize that the theory behind SABRE is not understood completely yet. The J-coupling based polarization transfer mechanism can not be used to explain the discrepancies of the $\vec{B}_P$ depen-

dencies of the signal amplification of ^{1}H and ^{19}F observed for all three target molecules.

The expected behavior can be caused by a polarization transfer to a ^{1}H of the target molecule and subsequently a transfer to the ^{19}F (cf. Fig. 6.9(a)). This, in turn, would lead to a correlation between the ^{1}H and ^{19}F $\vec{B}_P$ dependence which was clearly disproved. Due to the fact, that the polarization transfer takes place in the vicinity of the catalyst, it is possible that other coupling mechanisms like dipole-dipole coupling have to be considered. If the intramolecular dipole-dipole coupling does not get averaged out to zero, as it can be observed in isotropic liquids [Lev08], a direct polarization transfer could result (cf. Fig. 6.9(b)). A possible further explanation relies on a proton-proton exchange reaction (cf. Fig. 6.9(c)) [BKK^{+}14]. Here, a hydrogen atom originating from a pH_2 molecule is transferred to the target molecule where a intramolecular polarization transfer to the ^{19}F can occur. The presented results have been published in journal Scientific Reports [BRB^{+}17].

7 | Summary and outlook

7.1. Summary

The goal of this work was twofold: the development and realization of a low cost ULF NMR/MRI setup for the investigation of hyperpolarization techniques as well as the development of SQUID based current sensors.

The development of SQUID-based current sensors involved two sensor layouts. One approach involved three individual SQUIDs sensing the signal of one single pickup coil. Since the voltage noise of each SQUID is uncorrelated with respect to the other SQUIDs involved, using cross correlation methods of the sensed signals of the individual SQUIDs should considerably lower the environmentally caused noise. This could offer an approach to minimize the measurement time for a desired SNR which is desirable when, e.g., performing invivo measurements using hyperpolarization techniques. To realize such a sensor approach, trilayers based on SNS and SIS junctions have been employed. Due to a very high current density of the SNS fabrication process, only small SQUIDs could be developed which drastically reduces the input sensitivity of such a current sensor. Therefore, the fabrication process was modified in favor of a low current density process based on SIS type junctions. This change significantly improved the input sensitivity since larger SQUIDs could be implemented. Unfortunately, due to fabrication issues the yield was very low and cross correlation measurements could not be performed. Therefore, the feasibility of such a sensor arrangement could not be evaluated. In addition to the multi-SQUID approach, a common single SQUID current sensor was developed. This sensor approach incorporated the possibility to use a current lock loop (CLL) feedback scheme. This feedback scheme is mandatory

when setting up a multi channel SQUID sensor arrangement to increase the field-of-view or to investigate larger samples. However, this design also suffered from a very low yield caused by an insulation problem between the two Nb layers involved. Due to the fabrication problems no systematic optimization of the sensors has been performed.

To investigate the pH_2 based SABRE hyperpolarization technique, the complete infrastructure needed to perform continuous hyperpolarization NMR measurements in a very controlled and well defined manner was built from scratch within the framework of our collaboration. It started with the design and optimization of the coil system using numerical methods with the main goal of achieving a very homogenous measurement field $\vec{B}_0$ and highly linear gradient magnetic fields performed by the author. The $\vec{B}_0$ field is realized by a tetracoil which leads to highly homogenous magnetic fields. This was shown both by numerical simulations and very narrow line width of measured NMR peaks. The gradient coils only have been evaluated numerically and could not be characterized by the author due to a lack of appropriate current sources. A SQUID based magnetic field sensor has been built using a commercially available SQUID based current sensor and a second-order axial gradiometric pickup coil. In combination with a RF shielding chamber and magnetic shielding using μ-metal barrels, the system shows a very low magnetic field noise density $S_B^{1/2} = 1.15\,\mathrm{fT/Hz^{1/2}}$. This very low field noise environment enables the detection of unhyperpolarized ^{1}H signals in measurement fields below $40\,\mu$T without using the prepolarization coil.

The investigation of the SABRE hyperpolarization technique was very successful. First pyridine, soluted in methanol in combination with the iridium based IMes catalyst has been examined to reproduce results reported in literature [HSL$^+$13]. The hyperpolarizability of pyridine has been confirmed and a signal amplification of ≤ 200, compared to thermally polarized pyridine, was obtained. Based on this result further samples have been investigated: 3,5-bis(trifluoromethyl)pyridine, ethyl-5-fluoronicotinic acid and 3-fluoropyridine. They where chosen because they showed promising results in the high field SABRE NMR system at the University of Magdeburg. All samples contain both ^{1}H and ^{19}F nuclei, respectively. For 3-fluoropyridine and ethyl-5-fluoronicotinic acid J-coupling resonances has been resolved clearly, which underpins the validity of the J-coupling based polarization transfer theory. 3,5-bis(trifluoromethyl)pyridine, how-

ever, neither shows J-coupling induced splitting of the NMR peaks for ^{1}H nor for ^{19}F. Hyperpolarization, especially of the ^{19}F nucleus, however, has to be present because ^{19}F peaks of thermally polarized 3,5-bis(trifluoromethyl)pyridine can not be resolved. Thus, J-coupling seems not to be the responsible hyperpolarization mechanism and other possible mechanisms like direct or indirect transfer of the spin order from the pH_2 nuclei to the ^{19}F or a ^{1}H exchange and subsequent direct polarization transfer have to considered.

7.2. Outlook

The parahydrogen based hyperpolarization technique shows very promising results with respect of the signal amplification of different target molecules which could turn ultra-low field MRI into a cheap alternative for the high field implementations. Still, many problems and open questions remain. The two most obvious issues that have to be addressed concern the *in vivo* suitability of the needed substances and the pH_2 supply. Currently investigated target molecules and transfer catalyst have to be soluted in highly concentrated methanol or ethanol, respectively, which is very problematic for living organisms due to its inherent toxicity to cells. Therefore, water-soluble transfer target molecules have to be developed first. Recently, first positive results regarding water-soluble target molecules have been achieved by Rovedo *et al.* [RKB^{+}16], however still more effort has to be put into the molecule development. For a combination of an Ir based IMes catalyst and nicotinamide as target molecule, Rovedo *et al.* were able to show a signal amplification of ≈ 10000 in human cell cultures. However, as soon as blood was added, no amplification could be observed anymore. The second hurdle concerns the pH_2 supply. Up to now, it has not been solved how to supply the mandatory pH_2 to the organism under test in a sufficient amount. The most obvious approach involves pH_2-enriched air which could simply be inhaled by the patient/organism via a facial mask. It has been demonstrated in *in vivo* experiments on humans that after 20 min of inhaling air enriched with 3% of molecular H_2, a peak concentration of $\approx 25\,\mu$mol/l could have been found in the arterial blood [ONA^{+}12]. In principle, the hydrogen concentration could be increased by using higher enriched air, however the concentration in the blood would still be very small and the effectiveness of the SABRE induced signal amplification is not predictable. Due to those two

prominent drawbacks, the main focus in future experiments will be moved towards Overhauser dynamic nuclear polarization. Overhauser DNP is a technique that combines NMR and electron spin resonance (ESR), where the spin polarization of free electrons is transferred to the nuclei. This technique is a promising candidate for possible *in vivo* applications, especially since it relies on biocompatible substances. Zotev et at. reported the successful realization of an ULF MRI system to perform Overhauser dynamic nuclear polarization experiments [ZOM+10]. They were able to obtain *ex vivo* MRI images of a cactus at $|\vec{B}_0| = 46\,\mu\mathrm{T}$ employing Overhauser DNP after injecting a substance containing the free electrons needed (in form of radicals). Due to the use of ESR, microwave excitation pulses have to be applied to the sample ($\gamma_e/2\pi = 28.024\,\mathrm{GHz/T}$). The flexible and open design of our setup easily allows for the implementation of the needed loop antenna. In combination with recently delivered gradient coil current sources, not only Zotev's measurements have been reproduced but first DNP based MRI results with sub-mm voxel size have been achieved by our master student Paul Antkowiak [Ant17]. Soon, first DNP based *in vivo* experiments on rodents can be performed.

A VACOSHIELD magnetic and RF shielding chamber from Vacuumschmelze has been installed in the meantime which offers an ideal environment for upcoming measurements. Since the coil arrangement now does not have to be submerged into the μ-metal barrels, two advantages arise instantly. First, the system is very open now which allows for easy and convenient sample handling. Second, due to the size of the chamber, the metal walls now are farther away from the pickup coil and the coil system. This minimizes the field noise contribution arising from the μ-metal sensed by the pickup coil. Additionally this also allows faster magnetic field ramps since the back action of eddy currents within the shielding caused by such field ramps (e.g. gradient magnetic fields) is reduced due to the larger coil-wall distance.

O. Kieler from the PTB Braunschweig put a lot of effort into fighting the layer insulation problem. Two wafers have been produced since. They already have arrived and are waiting for their characterization. Two new magnetic field sensor dip sticks have already been built which only have to be equipped with the new sensor generation: one for the cross correlation measurements using multiple SQUIDs sensing one single pickup coil as well as a three-channel approach involving three first-order gradiometric pickup

coils for measurements with increased scan area, which is ideally suited to cover the whole rodent body during *in vivo* measurements.

A | Appendix A: SQUID characterization techniques

To determine both the transport and noise characteristics of a SQUID, it needs to be electrically connected and cooled down below its critical temperature T_c in an environment that is ideally free of magnetic field. Usually, the device under test (DUT) is glued onto a sample holder made of FR4 printed circuit board (PCB) material using double sided adhesive tape. The sample holder contains copper lines used to electrically connect the DUT by ultrasonic wire bonding (aluminium wire, $\varnothing = 25\,\mu$m). Subsequently, the sample holder is mounted at the end of a dip stick and is enclosed by a shielding package consisting of a copper cup for RF shielding and a high permeable Cryoperm®-10 cup for magnetic shielding, respectively. The residual magnetic field B_{res} at the DUT is of the order of $B_{res} \approx 100\,$nT. The dip stick then is immersed into a helium dewar, which is placed in a RF shielding chamber. Both the transport and the noise characterization are performed at $T = 4.2\,$K, respectively. Depending on the intended measurements, two different measurement schemes and read out electronics have to be used.

A.1. Transport measurements

The transport characteristics are determined by acquiring $I(V)$-, $I_c(\Phi_a)$- as well as $V(\Phi_a)$-curves using the scheme depicted in Fig. A.1. The current biasing of the DUT as well as the flux biasing is done by battery powered, voltage controlled low noise current sources. The voltage drop of the DUT is measured differentially by a battery powered high input impedance low

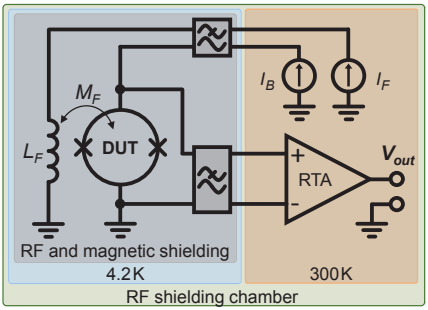

Figure A.1.: Schematic diagram of the low magnetic field setup used for DC transport measurements. The DUT is electromagnetically shielded and immersed in a helium transport vessel, cooling it to $T = 4.2\,\mathrm{K}$. Additionally, the vessel is located in a RF shielding chamber. All feed lines that connect the DUT with the bias current sources and the RTA are low pass filtered.

noise room temperature amplifier (RTA) with an input noise voltage density $S_V^{1/2} \approx 6\,\mathrm{nV}/\sqrt{\mathrm{Hz}}$. All signals are passed through cooled low pass filters with a cutoff frequency $f_{-3dB} \approx 13.5\,\mathrm{kHz}$, realized by a first-order T-filter topology (indicated by the boxes consisting a striked out and a not striked out wave, see Fig. A.1). This is mandatory since external RF radiation can have a radical influence on the SQUID performance [INS+93]. RF interference can be modeled as an additional RF bias current and RF flux bias superimposed to the DC biasing. Koch et al. showed by numerical simulations, that both RF flux or bias current noise causes a rounding of the IV- and $V(\Phi)$ curves which leads to a reduced transfer function or even render the SQUID inoperative [CB04, KFR+94].
The control of the current sources as well as the data acquisition is done by a DAC/ADC system of the company National Instruments.

A.2. Noise characterization

The characterization of the voltage noise density $S_V^{1/2}$ of a DUT and therefore its equivalent flux noise density $S_\Phi^{1/2} = S_V^{1/2} / V_\Phi$ is typically performed by employing a two-stage read out configuration in combination with a SQUID read out electronics allowing a FLL read out scheme (cf. Fig.

A.3). As has been shown in chapter 2.4, a nonhysteretic SQUID exhibits a periodic voltage response to applied flux Φ_a. When the SQUID is operated at its optimum working point W, its response is linear for small flux changes $\delta\Phi_a$ of the order of a view percent of Φ_0 [Dru16].

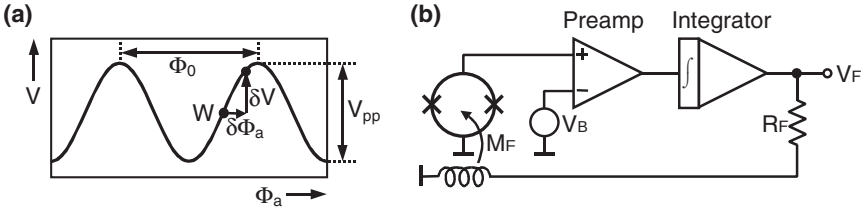

Figure A.2.: (a) $V(\Phi_a)$ characteristics with indicated optimum working point W. Without negative feedback, a positive change in applied flux $\delta\Phi_a$ results in a voltage response δV and a deviation away from W. (b) illustrates the basic flux locked loop (FLL) scheme which establishes negative feedback to maintain the working point W despite possible flux changes $\delta\Phi_a$. Adapted from [CB04]

If, however, $\delta\Phi_a$ exceeds the linear region, the flux sensitivity of the SQUID decreases drastically since $\partial V/\partial\Phi$ now depends on Φ_a, thus shifting the working point away from its optimum (cf. Fig. A.2(a)). To linearize the SQUID response to an applied flux Φ_a and therefore keeping the working point at its optimum W, a negative feedback scheme called FLL is used (cf. Fig. A.2(b)). The SQUID is biased at its optimum working point W where the voltage drop across the SQUID is V_B. For an ideal system any deviation from V_B, caused by $\partial\Phi_a$, is amplified by the preamplifier (infinite gain) and integrated. Via a feedback resistor R_F, the integrated voltage is fed back to the SQUID by a coil that is inductively coupled to the SQUID via the mutual inductance M_F. This effectively counteracts any deviation from W by compensating the applied flux: $\Phi_F = -\Phi_a$, thus 'locking' the flux penetrating the SQUID to a constant value. This leads to the FLL condition

$$V_\mathrm{F} \quad = \quad \frac{\Phi_\mathrm{F} R_\mathrm{F}}{M_\mathrm{F}} = -\frac{\Phi_\mathrm{a} R_\mathrm{F}}{M_\mathrm{F}}. \tag{A.1}$$

Thereby it is ensured that $S_\Phi^{1/2}$ is independent of Φ_a [CB04]. The resulting transfer coefficient of the FLL electronics therefore is given by $G_{FLL} = \partial V_F/\partial\Phi_a = -R_F/M_F$ [Dru16].

In real systems (which suffer from non ideal effects like loop delays, finite preamplifier gain and preamplifier input noise voltage), the preamplifier input noise voltage density $S_{V,PA}^{1/2}$ limits the overall system performance since its noise voltage density is usually larger than $S_{V,\mathrm{SQUID}}^{1/2}$. For example, a SQUID with $S_{\Phi}^{1/2} = 500\,\mathrm{n}\Phi_0/\sqrt{\mathrm{Hz}}$ in the white region and $V_\Phi = 200\,\mu\mathrm{V}/\Phi_0$ exhibits $S_{V,\mathrm{SQUID}}^{1/2} = 100\,\mathrm{pV}/\sqrt{\mathrm{Hz}}$. This is much lower than $S_{V,\mathrm{RTA}}^{1/2} \approx 6\,\mathrm{nV}/\sqrt{\mathrm{Hz}}$ of the RTA used for DC characterization and still ≈ 3.3 times larger as $S_{V,\mathrm{XXF}}^{1/2} = 330\,\mathrm{pV}/\sqrt{\mathrm{Hz}}$ of the used Magnicon XXF-1 FLL electronics. To overcome this limitation and to be able to determine the noise characteristics of the DUT, a cryogenic preamplifier in form of a SQUID series array (SSA) is employed [WM91]. A SSA consists

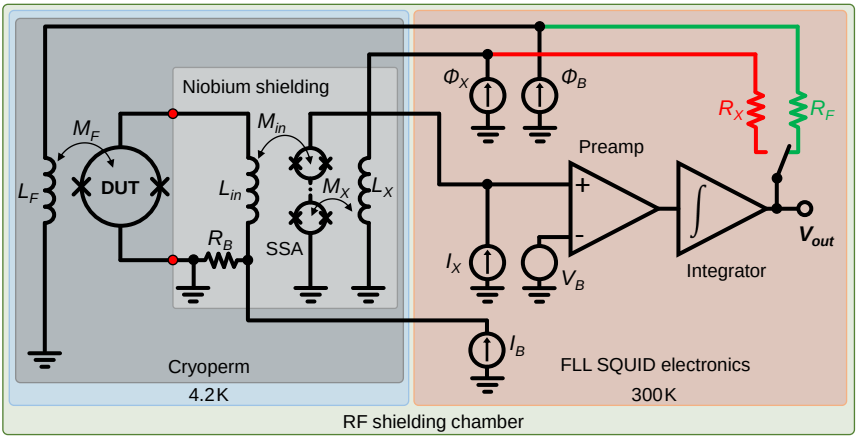

Figure A.3.: Setup for the characterization of the equivalent flux noise density $S_\Phi^{1/2}$ using a two-stage FLL scheme. The DUT is voltage biased by a current sent through R_B ($R_B \ll R_{DUT}$). Current noise $S_I^{1/2}$ of the DUT is coupled to the SSA cryogenic preamplifier via M_i where it gets amplified and integrated. After integration, the signal is fed back either to the DUT or the SSA.

of a series connection of N shunted SQUIDs, each equipped with a equally dimensioned signal input coil. Given that all SQUIDs are identical and the input signal is coupled uniformly into each of the N SQUIDs, the response of all individual array SQUIDs is equal and the voltage response adds up

coherently. Therefore, the response of the SSA to an input signal is single-SQUID like, but the voltage drop is N times the voltage drop of a single array SQUID. Additionally, since $S_{V,i}^{1/2}$ of each array SQUID is uncorrelated, the total $S_{V,\text{SSA}}^{1/2}$ scales $\propto \sqrt{N}$, thus $S_{\Phi,\text{SSA}}^{1/2} \propto 1/\sqrt{N}$ [Dru16]. To effectively couple the DUT to the SSA, the DUT is biased with a constant voltage established by the bias resistor $R_B = 0.2\,\Omega$ (cf. Fig. A.3). A superconducting coil L_{in} is connected in series with the DUT and acts as the input coil for the SSA. The SSA is current and flux biased to its optimum working point W (with the voltage V_B) via I_X and Φ_X, respectively. Any applied flux Φ_a or noise current originating from the DUT itself modulates the current through the DUT and therefore the current through L_{in}. Via M_{in} it is coupled to the SSA which leads to a voltage deviation from V_B. This deviation, as already explained above, is amplified, integrated and fed back to the system. The XXF-1 FLL electronics allows for two feedback modes. On the one hand the feedback can be applied to the DUT via R_F and the feedback coil L_F with the mutual inductance M_F and leaving the SSA open loop (green feedback path in Fig. A.3). On the other hand the feedback can be applied to the SSA via R_X and L_X with the mutual inductance M_X while leaving the DUT open loop (red feedback path in Fig. A.3). For the gain of the two-stage configuration in FLL mode follows $G_{2S} = V_\Phi M_k \,/\, R_k$, with k being either F or X, depending on the chosen feedback path.
The system noise is made up of three components

$$S_{\Phi,\text{tot}}^{1/2} = \left(S_\Phi + \frac{S_{V,\text{XXF}}}{V_\Phi^2} + S_{I,\text{XXF}} \cdot M_{dyn}^2 \right)^{1/2}, \tag{A.2}$$

where $S_{I,\text{XXF}}^{1/2}$ is the noise current density of the XXF-1 input stage and $M_{\text{dyn}} = R_{\text{dyn}} \,/\, V_\Phi$ is the current sensitivity of the DUT.

A.3. Determination of A_{eff} and the system transfer coefficient $V_{\Phi,\text{sys}}$

The effective area A_{eff} is defined by the ratio of magnetic flux Φ_S applied to the SQUID by a magnetic field B applied to the pickup coil L_{P}. It is a measure of the efficiency of the SQUID for picking up magnetic flux [CB04]. The determination of A_{eff} of the SCS is straight forward. A calibrated coil

L_{cal} is placed coaxially next to the lowest loop of the gradiometric pickup coil in a well defined manner (i.e. the distance between the two loops is well known and they are positioned as parallel as possible). Using Matlab, the mutual inductance M_{cal} between L_{cal} and the gradiometric pickup coil L_{P} is calculated. The calculation takes into account the other loop (first-order gradiometer)/loops (n^{th}-order gradiometer) of the pickup coil when calculating the mutual inductance. By applying a current I_{cal} to L_{cal}, flux Φ_{cal} is applied to the pickup coil: $\Phi_{\mathrm{cal}} = B_{\mathrm{cal}} A_{\mathrm{P}} = M_{\mathrm{cal}} I_{\mathrm{cal}}$, where A_{P} is the area of one loop of the pickup coil. Φ_{cal} induces the screening current $I_{\mathrm{in}} = \Phi_{\mathrm{cal}}/(L_{\mathrm{P}} + L_{\mathrm{in}})$ in the superconducting input circuit. By knowing the mutual inductance M_{in}, the flux Φ_{S} applied to SQUID can be calculated:

$$\Phi_{\mathrm{S}} \quad = \quad M_{\mathrm{in}} I_{\mathrm{in}} = \frac{M_{\mathrm{in}} A_{\mathrm{P}}}{L_{\mathrm{P}} + L_{\mathrm{in}}} B_{\mathrm{cal}} = A_{\mathrm{eff}} B_{\mathrm{cal}}. \tag{A.3}$$

For an easy evaluation, e.g. by the use of an oscilloscope, I_{cal} is set such, that Φ_{S} fulfills $\Phi_{\mathrm{S}} = n\Phi_0$ ($n \in \mathbb{N}$). Rearranging equation (A.3) for A_{eff} leads to the final expression:

$$A_{\mathrm{eff}} \quad = \quad \frac{\Phi_{\mathrm{S}}}{B_{\mathrm{cal}}} = \frac{n\Phi_0 A_{\mathrm{P}}}{M_{\mathrm{cal}} I_{\mathrm{cal}}} \tag{A.4}$$

The calibration coil L_{cal} can also be used to determine the system transfer coefficient $V_{\Phi,\mathrm{sys}}$, i.e. the voltage output change ΔV_{F} of the FLL electronics to a flux change $\Delta\Phi_a$ applied to the pickup coil $V_{\Phi,\mathrm{sys}} = |\Delta V_{\mathrm{F}}/\Delta\Phi_a|$. First, the FLL electronics is operated in open loop mode. A current I_{cal} is applied to L_{cal} that produces exactly $1\,\Phi_0$ in the SQUID. Now, the FLL will be locked and the same current will be applied to the calibration coil. The resulting voltage output of the FLL electronics equals the system transfer coefficient $V_{\Phi,\mathrm{sys}}$. At this point, by using the equation for the FLL condition (A.1), the equation for A_{eff} (A.4) and the obtained system transfer coefficient, any output voltage change can be translated to a magnetic field B_{sig} that originates from a signal source:

$$B_{\mathrm{sig}} \quad = \quad -\frac{V_{\Phi,\mathrm{sys}} M_{\mathrm{F}}}{A_{\mathrm{eff}} R_{\mathrm{F}}}. \tag{A.5}$$

List of acronyms

AC	alternating current
ADC	analog-to-digital conversion
APF	additional positive feedback
CLL	current lock loop
CMRR	common mode rejection ratio
CMP	chemical-mechanical polishing
CRC	clean room center
DAC	digital-to-analog conversion
DC	direct current
DNP	dynamic nuclear polarization
DUT	device under test
EBL	electron beam lithography
ESR	electron spin resonance
FFT	fast Fourier transform
FID	free induction decay
FLL	flux locked loop
FOV	field of view
fMRI	functional magnetic resonance imaging
FWHM	full width at half maximum
GFRP	glass-fiber reinforced plastic
GL	Ginzburg-Landau
IBE	ion beam etching
IR	inversion recovery
JJ	Josephson junction
LAC	level anti-crossing
mK	milli Kelvin
MOSFET	metal-oxide-semiconductor field-effect transistor
MEG	Magnetoencephalography

MPI	Max-Planck institute
MRI	magnetic resonance imaging
NMR	nuclear magnetic resonance
oH_2	orthohydrogen
PCB	printed circuit board
PE	Polyethylene
PECVD	plasma enhanced chemical vapor deposition
PEEK	polyether ether ketone
pH_2	parahydrogen
PHIP	parahydrogen induced polarization
PMMA	polymethylmethacrylate
PTB	Physikalisch-Technische Bundesanstalt
PTFE	polytetrafluoroethylene
PUR	polyurethane
PVC	polyvinyl chloride
Q factor	quality factor
Q spoiler	Circuitry to spoil the quality factor of a superconducting input circuit, i.e. a controllable current limiting circuitry in the input circuit
RC	resistor capacitor
RCSJ	resistively and capacitively shunted junction
RF	radio frequency
RIE	reactive ion etching
RMS	root mean square
RTA	room temperature amplifier
SABRE	signal amplification by reversible exchange
SAR	specific absorption rate
SEM	scanning electron microscope
SCS	SQUID-based current sensor
SIS	superconductor-insulator-superconductor
SNR	signal-to-noise ratio
SNS	superconductor-normal conductor-superconductor
SQUID	Superconducting Quantum Interference Device
SSA	SQUID series array
TCD	thermal conductivity detector
TTL	transistor-transistor logic
ULF	ultra-low field
UV	ultraviolet
VCCS	voltage controlled current source
VIA	vertical interconnect access

List of Figures

Bibliography

[AAA+09] Ralph W Adams, Juan A Aguilar, Kevin D Atkinson, Michael J Cowley, Paul I P Elliott, Simon B Duckett, Gary G R Green, Iman G Khazal, Joaquín López-Serrano, and David C Williamson. Reversible interactions with para-hydrogen enhance NMR sensitivity by polarization transfer. *Science (New York, N.Y.)*, 323(5922):1708–11, mar 2009.

[ABA17] ABACUS electronics, https://www.abacus-electronics.de/produkte/verstarker/60-120d/60-120d-dolifet.html. *Abacus 60-120D DOLIFET SE*, 5 2017.

[Abr57] A. A. Abrikosov. On the magnetic properties of superconductors of the second group. *Zh. Eksp. i Teor. Fiz*, 32:1442, 1957.

[ALFG+03] J. Ardenkjær-Larsen, B. Fridlund, A. Gram, G. Hansson, L. Hansson, M. Lerche, R. Servin, M. Thaning, and K. Golman. Increase in signal-to-noise ratio of $>$ 10,000 times in liquid-state NMR. *Proceedings of the National Academy of Sciences*, 100(18):10158–10163, 2003.

[Ant15] Paul Antkowiak. Optimization of an electromagnetic shielding chamber for prepolarized ultra-low-field MRI, Bachelor's thesis, 2015.

[Ant17] Paul Antkowiak. From Spectrum to Image - Implementation of imaging Gradients for ULF MRI, Master's thesis, 2017.

[AR63] P. W. Anderson and J. M. Rowell. Probable observation of the josephson superconducting tunneling effect. *Phys. Rev. Lett.*, 10:230–232, Mar 1963.

[BCH+14] R.W. Brown, Y.C.N. Cheng, E.M. Haacke, M.R. Thompson, and R. Venkatesan. *Magnetic Resonance Imaging: Physical Principles and Sequence Design*. Wiley Blackwell, 2014.

[BCS57] J. Bardeen, L. N. Cooper, and J. R. Schrieffer. Microscopic theory of superconductivity. *Phys. Rev.*, 106:162–164, Apr 1957.

[BDK+07] J. Beyer, D. Drung, A. Kirste, J. Engert, A. Netsch, A. Fleischmann, and C. Enss. A magnetic-field-fluctuation thermometer for the mk range based on squid-magnetometry. *IEEE Transactions on Applied Superconductivity*, 17(2):760–763, June 2007.

[BFSM12] L. Buljubasich, M. B. Franzoni, H. W. Spiess, and K. Münnemann. Level anti-crossings in Para Hydrogen Induced Polarization experiments with Cs-symmetric molecules. *Journal of Magnetic Resonance*, 219:33–40, 2012.

[BHM+12] Sarah Busch, Michael Hatridge, Michael Mössle, Whittier Myers, Travis Wong, Michael Mück, Kevin Chew, Kyle Kuchinsky, Jeffry Simko, and John Clarke. Measurements of T1-relaxation in ex vivo prostate tissue at 132 uT. *Magnetic Resonance in Medicine*, 67(4):1138–1145, 2012.

[BHP46] F. Bloch, W. W. Hansen, and Martin Packard. Nuclear induction. *Phys. Rev.*, 69:127–127, Feb 1946.

[BK13] W. Buckel and R. Kleiner. *Supraleitung: Grundlagen und Anwendungen*. Lehrbuch Physik. Wiley, 2013.

[BKK+14] Danila A. Barskiy, Kirill V. Kovtunov, Igor V. Koptyug, Ping He, Kirsten A. Groome, Quinn A. Best, Fan Shi, Boyd M. Goodson, Roman V. Shchepin, Aaron M. Coffey, Kevin W. Waddell, and Eduard Y. Chekmenev. The Feasibility of Formation and Kinetics of NMR Signal Amplification by Reversible Exchange (SABRE) at High Magnetic Field (9.4 T).

Journal of the American Chemical Society, 136(9):3322–3325, 2014.

[BRB+17] K. Buckenmaier, M. Rudolph, C. Back, T. Misztal, U. Bommerich, P. Fehling, D. Koelle, R. Kleiner, H. A. Mayer, K. Scheffler, J. Bernarding, and M. Plaumann. SQUID-based detection of ultra-low-field multinuclear NMR of substances hyperpolarized using signal amplification by reversible exchange. *Scientific Reports*, 7:13431, Oct 2017.

[BRD+15] S. Bechstein, F. Ruede, D. Drung, J.-H. Storm, O. F. Kieler, J. Kohlmann, T. Weimann, and T. Schurig. HfTinanoSQUID gradiometers with high linearity. *Applied Physics Letters*, 106(7):072601, 2015.

[Bru17a] Bruker BioSpin, https://www.bruker.com/products/mr/nmr/accessories/hyperpolarization/parahydrogen-generator/overview.html. *Parahydrogen pH_2 Generator*, 6 2017.

[Bru17b] Bruker Corporation, https://www.bruker.com/products/mr/nmr/nmr-software/nmr-software/topspin/overview.html. *Topspin*, 7 2017.

[BSB+96] Peter Bachert, Lothar R. Schad, Michael Bock, Michael V. Knopp, Michael Ebert, Tino Grobmann, Werner Heil, Dirk Hofmann, Reinhard Surkau, and Ernst W. Otten. Nuclear magnetic resonance imaging of airways in humans with use of hyperpolarized ^{3}He. *Magnetic Resonance in Medicine*, 36(2):192–196, 1996.

[BSH+13] Robert Borowiak, Niels Schwaderlapp, Frank Huethe, Thomas Lickert, Elmar Fischer, Sébastien Bär, Jürgen Hennig, Dominik Von Elverfeldt, and Jan Bernd Hövener. A battery-driven, low-field NMR unit for thermally and hyperpolarized samples. *Magnetic Resonance Materials in Physics, Biology and Medicine*, 26:491–499, 2013.

[BWW+15] A. Buchter, R. Wölbing, M. Wyss, O. F. Kieler, T. Weimann, J. Kohlmann, A. B. Zorin, D. Rüffer, F. Matteini,

G. Tütüncüoglu, F. Heimbach, A. Kleibert, A. Fontcuberta i Morral, D. Grundler, R. Kleiner, D. Koelle, and M. Poggio. Magnetization reversal of an individual exchange-biased permalloy nanotube. *Phys. Rev. B*, 92:214432, Dec 2015.

[CAA+11] Michael J. Cowley, Ralph W. Adams, Kevin D. Atkinson, Martin C. R. Cockett, Simon B. Duckett, Gary G. R. Green, Joost A. B. Lohman, Rainer Kerssebaum, David Kilgour, and Ryan E. Mewis. Iridium n-heterocyclic carbene complexes as efficient catalysts for magnetization transfer from para-hydrogen. *Journal of the American Chemical Society*, 133(16):6134–6137, 2011. PMID: 21469642.

[CB04] J. Clarke and A.I. Braginski, editors. *The SQUID Handbook Volume: Vol. 1 Fundamental and technology of SQUIDs and SQUIDs Systems*. Wiley-VCH, 2004.

[CHM07] John Clarke, Michael Hatridge, and Michael Mößle. Squid-detected magnetic resonance imaging in microtesla fields. *Annual Review of Biomedical Engineering*, 9(1):389–413, 2007. PMID: 17328671.

[CMR17] CMR-Direct, http://www.cmr-direct.com/en/cmr-gevar-25ml. *GE Varnish VGE7031*, 6 2017.

[COM17] COMSOL Multiphysics GmbH, https://www.comsol.com. *Comsol Multiphysics*, 6 2017.

[CRD+91] R. Cantor, T. Ryhanen, D. Drung, H. Koch, and H. Seppa. Design and optimization of DC SQUIDs fabricated using a simplified four-level process. *IEEE Transactions on Magnetics*, 27(2):2927–2931, Mar 1991.

[Cry17] Cryoton, www.cryoton.org. *Cryoton LH-11.5-NTE*, 6 2017.

[DAB+05] D. Drung, C. Assmann, J. Beyer, M. Peters, F. Ruede, and T. Schurig. dc SQUID readout electronics with up to 100 MHz closed- loop bandwidth. *Ieee Trans.Appl.Superconduct.*, 15(2):777–780, 2005.

[DAB+07] D. Drung, C. Aßmann, J. Beyer, A. Kirste, M. Peters, F. Ruede, and Th. Schurig. Highly sensitive and easy-to-use SQUID sensors. *IEEE Transactions on Applied Superconductivity*, 17(2):699–704, 2007.

[DHB06] Dietmar Drung, Colmar Hinnrichs, and Henry-Jobes Barthelmess. Low-noise ultra-high-speed dc SQUID readout electronics. *Superconductor Science and Technology*, 19(5):S235, 2006.

[Dr.17] Dr. Hubert, http://drhubert.de/a-1110-16-qe-4-quadrantenspannungs-stromverstaerker.html. *Dr. Hubert A1110-16-QE*, 5 2017.

[Dru16] Dietmar Drung. Introduction to Nb-Based SQUID Sensors. (April):1–33, 2016.

[DS15] D. Drung and J. H. Storm. Private communication. 2015.

[DSZN05] R. Dolata, H. Scherer, A. B. Zorin, and J. Niemeyer. Single-charge devices with ultrasmall Nb/AlOx/Nb trilayer Josephson junctions. *Journal of Applied Physics*, 97(5):054501, 2005.

[ESK93] K. Enpuku, Y. Shimomura, and T. Kisu. Effect of thermal noise on the characteristics of a high Tc superconducting quantum interference device. *Journal of Applied Physics*, 73(11):7929–7934, 1993.

[Fin59] H.J. Fink. New absolute noise thermometer at low temperatures. *Canad. J. Phys*, 37:1397, 1959.

[Gig17] Gigavac, http://www.gigavac.com/products/gr3bja335. *Gigavac GR3BJA335*, 6 2017.

[GL50] V. Ginzburg and L. Landau. Toward the superconductivity theory. *Zhurnal Eksp. Yheoret. Physics*, 29, 1950.

[GM12] R. Gross and A. Marx. *Festkörperphysik*. Festkörperphysik. De Gruyter, 2012.

[GMA+03] G Gottardi, P Mesirca, C Agostini, D Remondini, and F Bersani. A four coil exposure system (tetracoil) producing a highly uniform magnetic field. *Bioelectromagnetics*, 24(2):125–33, feb 2003.

[HC85] C. Hilbert and J. Clarke. DC SQUIDs as radiofrequency amplifiers. *Journal of Low Temperature Physics*, 61(3):263–280, 1985.

[HCH+09] Jan Bernd Hövener, Eduard Y. Chekmenev, Kent C. Harris, William H. Perman, Larry W. Robertson, Brian D. Ross, and Pratip Bhattacharya. PASADENA hyperpolarization of 13C biomolecules: equipment design and installation. *Magma (New York, N.Y.)*, 22:111–121, 2009.

[HCSH85] C. Hilbert, J. Clarke, T. Sleator, and E. L. Hahn. Application of a dc SQUID to rf amplification: NQR. *SQUID '85: Superconducting quantum interference devices and their applications*, 1985.

[HDC+13] Q. Herreros, H. Dyvorne, P. Campiglio, G. Jasmin-Lebras, A. Demonti, M. Pannetier-Lecoeur, and C. Fermon. Very low field magnetic resonance imaging with spintronic sensors. *Review of Scientific Instruments*, 84(9):095116, 2013.

[Hen17] Henkel Adhesives, http://www.henkel-adhesives.com/product-search-1554.htm?nodeid=8802585018369. *LOCTITE STYCAST 2850FT*, 6 2017.

[Hig13] Ruth Highton. *Using SABRE in NMR and MRI*. PhD thesis, 2013.

[Hig17] HighFinesse GmbH, http://www.highfinesse.com/en/precisioncurrentsources/27/bcs-series. *HighFinesse BCS 5/75*, 5 2017.

[HKS+14] Jan-Bernd Hövener, Stephan Knecht, Niels Schwaderlapp, Jürgen Hennig, and Dominik von Elverfeldt. Continuous Re-hyperpolarization of Nuclear Spins Using Parahydrogen:

Theory and Experiment. *ChemPhysChem*, 15(12):2451–2457, 2014.

[HSL+13] Jan-Bernd Hövener, Niels Schwaderlapp, Simon B Lickert, Thomas and. Duckett, Ryan E. Mewis, Louise A. R. Highton, Stephen M. Kenny, Gary G. R. Green, Dieter Leibfritz, Jan G. Korvink, Jürgen Hennig, and Dominik von Elverfeldt. A hyperpolarized equilibrium for magnetic resonance. *Nature communications*, 4:2946, 2013.

[IBS+13] Ben Inglis, Kai Buckenmaier, Paul Sangiorgio, Anders F Pedersen, Matthew Nichols, and John Clarke. MRI of the human brain at 130 microtesla. *Proceedings of the National Academy of Sciences of the United States of America*, 110(48):19194–201, 2013.

[INS+93] N. Ishikawa, K. Nagata, H. Sato, N. Kasai, and S. Kiryu. Effect of RF interference on characteristics of DC SQUID system. *IEEE Transactions on Applied Superconductivity*, 3(1):1910–1913, March 1993.

[JCK02] A. M. Juarez, D. Cubric, and George C. King. A compact catalytic converter for the production of para-hydrogen. *Measurement Science and Technology*, 13(5):N52–N55, 2002.

[Jin98] Jianming Jin. *Electromagnetic analysis and design in magnetic resonance imaging.* Biomedical Engineering. CRC Press, 1998.

[JK81] J. M. Jaycox and M. B. Ketchen. Planar coupling scheme for ultra low noise dc SQUIDs. *IEEE Trans. Magn.*, 17:400–403, 1981.

[JLSM64] R. C. Jaklevic, J. Lambe, A. H. Silver, and J. E. Mercereau. Quantum interference effects in Josephson tunneling. *Phys. Rev. Lett.*, 12:159, 1964.

[Joh28] J.B. Johnson. Thermal agitation of electricity in conductors. *Physical Review*, 32:97–109, 1928.

[Jos62] B.D. Josephson. Possible new effects in superconductive tunneling. *Physics Letters*, 1(7):251 – 253, 1962.

[KAT87] Jukka Knuutila, Antti Ahonen, and Claudia Tesche. Effects on DC SQUID characteristics of damping of input coil resonances. *Journal of Low Temperature Physics*, 68(3):269–284, 1987.

[KBF15] Katarzyna Krupa and Monika Bekiesinska-Figatowska. Artifacts in magnetic resonance imaging. *Polish Journal of Radiology*, 80:93 – 106, 2015.

[KE16] A. Kirste and J. Engert. A squid-based primary noise thermometer for low-temperature metrology. *Philosophical Transactions of the Royal Society of London A: Mathematical, Physical and Engineering Sciences*, 374(2064), 2016.

[KEMV14] R.H. Kraus, M. Espy, P. Magnelind, and P. Volegov. *Ultra-Low Field Nuclear Magnetic Resonance: A New MRI Regime*. OUP USA, 2014.

[Kep17] Kepco, Inc., http://www.kepcopower.com/bop.htm. *Kepco BOP 100-4 ML*, 5 2017.

[Ket87] M. Ketchen. Integrated thin-film dc squid sensors. *IEEE Transactions on Magnetics*, 23(2):1650–1657, Mar 1987.

[KFR+94] R. H. Koch, V. Foglietti, J. R. Rozen, K. G. Stawiasz, M. B. Ketchen, D. K. Lathrop, J. Z. Sun, and W. J. Gallagher. Effects of radio frequency radiation on the dc SQUID. *Applied Physics Letters*, 65(1):100–102, 1994.

[Kha03] M.M. Khapaev. 3D-MLSI: The program for extraction of 3D inductances of multilayer superconductor circuits. *Programm und Benutzerhandbuch*, 2003.

[Kie17] Oliver Kieler. *Pulsgetriebenes AC-Josephson-Spannungsnormal - Josephson Arbitrary Waveform Synthesizer*. PhD thesis, Technische Universität Ilmenau, 2017.

[KJ82] M. B. Ketchen and J. M. Jaycox. Ultra-low-noise tunnel junction dc SQUID with a tightly coupled planar input coil. *Appl. Phys. Lett.*, 40:736–738, 1982.

[KKM07] Oliver F Kieler, Johannes Kohlmann, and Franz MÃ¼ller. Improved design of superconductor/normal conductor/superconductor Josephson junction series arrays for an ac Josephson voltage standard. *Superconductor Science and Technology*, 20(11):S318, 2007.

[KKS+88] Jukka Knuutila, Matti Kajola, Heikki Seppä, Risto Mutikainen, and Jorma Salmi. Design, optimization, and construction of a dc SQUID with complete flux transformer circuits. *Journal of Low Temperature Physics*, 71(5):369–392, 1988.

[KMD+14] M. Khabipov, B. Mackrodt, R. Dolata, T. Scheller, and A. Zorin. Investigation of nonlinear superconducting microwave resonators including Nb Josephson junctions and SQUID arrays. *Journal of Physics: Conference Series*, 507(4):042016, 2014.

[KMK+07] J. Kohlmann, F. Muller, O. Kieler, R. Behr, L. Palafox, M. Kahmann, and J. Niemeyer. Josephson series arrays for programmable 10-v sinis josephson voltage standards and for josephson arbitrary waveform synthesizers based on sns junctions. *IEEE Transactions on Instrumentation and Measurement*, 56(2):472–475, April 2007.

[KML+93] D. Koelle, A. H. Miklich, F. Ludwig, E. Dantsker, D. T. Nemeth, and John Clarke. dc SQUID magnetometers from single layers of $YBa_2Cu_3O_{7-x}$. *Applied Physics Letters*, 63(16):2271–2273, 1993.

[KO11] H. Kamerlingh-Onnes. The disappearance of the resistivity of mercury. *Communications of the Physical Laboratory of Leiden*, 1911.

[Koc16] Stuart Koch. A Practical Guide to Low Frequency Magnetic Shielding. Technical report, Amuneal Manufacturing Corp. Philadelphia, PA, 2016.

[KRE+14] A. Kirste, M. Regin, J. Engert, D. Drung, and T. Schurig. A calculable and correlation-based magnetic field fluctuation thermometer. *Journal of Physics: Conference Series*, 568(3):032012, 2014.

[LAB+12] Lyrelle S. Lloyd, Ralph W. Adams, Michael Bernstein, Steven Coombes, Simon B. Duckett, Gary G. R. Green, Richard. J. Lewis, Ryan E. Mewis, and Christopher J. Sleigh. Utilization of SABRE-Derived Hyperpolarization To Detect Low-Concentration Analytes via 1D and 2D NMR Methods. *Journal of the American Chemical Society*, 134(31):12904–12907, 2012.

[LAB+14] Lyrelle S. Lloyd, Aziz Asghar, Michael J. Burns, Adrian Charlton, Steven Coombes, Michael J. Cowley, Gordon J. Dear, Simon B. Duckett, Georgi R. Genov, Gary G. R. Green, Louise A. R. Highton, Alexander J. J. Hooper, Majid Khan, Iman G. Khazal, Richard. J. Lewis, Ryan E. Mewis, Andrew D. Roberts, and Amy J. Ruddlesden. Hyperpolarisation through reversible interactions with parahydrogen. *Catal. Sci. Technol.*, 4:3544–3554, 2014.

[LDH06] Zhongming Liu, Lei Ding, and Bin He. Integration of eeg/meg with mri and fmri. *IEEE Engineering in Medicine and Biology Magazine*, 25(4):46–53, July 2006.

[Lev08] M.H. Levitt. *Spin Dynamics: Basics of Nuclear Magnetic Resonance*. Wiley, 2008.

[Lin] Linear Technology Corporation, www.linear.com. *LTspiceIV*.

[LL35] F. London and H. London. Zur Theorie der Supraleitung. *Zeitschrift für Physik*, 96:359–364, 1935.

[LMM+05] Seung Kyun Lee, Michael Mössle, Whittier Myers, Nathan Kelso, Andreas H. Trabesinger, Alexander Pines, and John Clarke. SQUID-detected MRI at 132 uT with T1-weighted contrast established at 10 uT-300 mT. *Magnetic Resonance in Medicine*, 53(1):9–14, 2005.

[Mag13a] Magnicon GmbH, www.magnicon.de. *High Performance dc SQUID Electronics XXF-1 Manual*, 11 2013. v3.3.11.

[Mag13b] Magnicon GmbH, www.magnicon.de. *Magnicon Single-stage current sensors*, 11 2013.

[Mar96] A. Marx. *Niederfrequentes 1/f-Rauschen in Josephson-Kontakten aus Hochtemperatur-Supraleitern.* PhD thesis, Eberhard-Karls-Universität Tübingen, 1996.

[MC96] J. McDonald and John R. Clem. Theory of flux penetration into thin films with field-dependent critical current. *Phys. Rev. B*, 53:8643–8650, Apr 1996.

[McC68] D. E. McCumber. Effect of ac Impedance on dc Voltage-Current Characteristics of Superconductor Weak-Link Junctions. *Journal of Applied Physics*, 39(7):3113–3118, 1968.

[Mec13] Johannes Maximilian Meckbach. *Superconducting Multilayer Technology for Josephson Devices.* PhD thesis, Karlsruhe Institute of Technology, 2013.

[MHM+06] Michael Mößle, Song I. Han, Whittier R. Myers, Seung Kyun Lee, Nathan Kelso, Michael Hatridge, Alexander Pines, and John Clarke. SQUID-detected microtesla MRI in the presence of metal. *Journal of Magnetic Resonance*, 179:146–151, 2006.

[MJC83] B. Muhlfelder, W. Johnson, and M. Cromar. Double transformer coupling to a very low noise squid. *IEEE Transactions on Magnetics*, 19(3):303–307, May 1983.

[MMR55] H. M. McConnell, A. D. McLean, and C. A. Reilly. Analysis of Spin-Spin Multiplets in Nuclear Magnetic Resonance Spectra. *The Journal of Chemical Physics*, 23(6):1152–1159, 1955.

[MO33] R.W. Meissner and R. Ochsenfeld. Ein neuer Effekt bei Eintritt der Supraleitfähigkeit. *Die Naturwissenschaften, Volume 21, Issue 44, pp.787-788*, 21:787–788, November 1933.

[MPGM+16] María José Martínez-Pérez, Diego Gella, Benedikt Müller, Viacheslav Morosh, Roman Wölbing, Javier Sesé, Oliver Kieler, Reinhold Kleiner, and Dieter Koelle. Three-Axis Vector Nano Superconducting Quantum Interference Device. *ACS Nano*, 10(9):8308–8315, 2016. PMID: 27332709.

[MS11] Kerstin Münnemann and Hans Wolfgang Spiess. The art of signal enhancement. *Nature Physics*, 7(7):522–523, 2011.

[Mye06] Whittier Ryan Myers. *Potential Applications of Microtesla Magnetic Resonance Imaging Detected Using a Superconducting Quantum Interference Device*. PhD thesis, 2006.

[Nat17a] National instruments, http://sine.ni.com/nips/cds/view/p/lang/de/nid/207417. *NI PXIee-6363*, 5 2017.

[Nat17b] National instruments, http://www.ni.com/de-de/support/model.pxi-6723.html. *NI PXIee-6723*, 5 2017.

[NBX+13] J. Nagel, A. Buchter, F. Xue, O. F. Kieler, T. Weimann, J. Kohlmann, A. B. Zorin, D. Rüffer, E. Russo-Averchi, R. Huber, P. Berberich, A. Fontcuberta i Morral, D. Grundler, R. Kleiner, D. Koelle, M. Poggio, and M. Kemmler. Nanoscale multifunctional sensor formed by a ni nanotube and a scanning nb nanosquid. *Phys. Rev. B*, 88:064425, Aug 2013.

[Nyq28] H. Nyquist. Thermal agitation of electric charge in conductors. *Physical Review*, 32:110–113, 1928.

[ONA+12] Hirohisa Ono, Yoji Nishijima, Naoto Adachi, Masaki Sakamoto, Yohei Kudo, Kumi Kaneko, Atsunori Nakao, and Takashi Imaoka. A basic study on molecular hydrogen (H2) inhalation in acute cerebral ischemia patients for safety check with physiological parameters and measurement of blood H2 level. 2(1):21, 2012.

[Par17] Parcom Präzisionsarmaturen GmbH, http://www.parcom.de/. *Precision needle valve Parcom M6A-H1L-V-SS-TC*, 6 2017.

[PIY+15] Andrey N. Pravdivtsev, Konstantin L. Ivanov, Alexandra V. Yurkovskaya, Pavel A. Petrov, Hans Heinrich Limbach, Robert Kaptein, and Hans Martin Vieth. Spin polarization transfer mechanisms of SABRE: A magnetic field dependent study. *Journal of Magnetic Resonance*, 261:73–82, 2015.

[Pol99] Effect of an input coil microwave resonance on dynamics and noise properties of a dc superconducting quantum interference device operating close to the hysteretic mode. *Review of Scientific Instruments*, 70(3):1713–1718, 1999.

[PSS16] Rolf Pohmann, Oliver Speck, and Klaus Scheffler. Signal-to-noise ratio and mr tissue parameters in human brain imaging at 3, 7, and 9.4 tesla using current receive coil arrays. *Magnetic Resonance in Medicine*, 75(2):801–809, 2016.

[PTP46] E. M. Purcell, H. C. Torrey, and R. V. Pound. Resonance absorption by nuclear magnetic moments in a solid. *Phys. Rev.*, 69:37–38, Jan 1946.

[PYV+13] Andrey N. Pravdivtsev, Alexandra V. Yurkovskaya, Hans Martin Vieth, Konstantin L. Ivanov, and Robert Kaptein. Level anti-crossings are a key factor for understanding para-hydrogen-induced hyperpolarization in SABRE experiments. *ChemPhysChem*, 14(14):3327–3331, 2013.

[Qua] Quantum Design, http://www.qdusa.com/sitedocs /productBrochures/squid3.pdf. *Model 50 DC SQUID SENSOR.*

[RKB+16] Philipp Rovedo, Stephan Knecht, Tim Bäumlisberger, Anna Lena Cremer, Simon B. Duckett, Ryan E. Mewis, Gary G. R. Green, Michael Burns, Peter J. Rayner, Dieter Leibfritz, Jan G. Korvink, Jürgen Hennig, Gerhard Pütz, Dominik von Elverfeldt, and Jan-Bernd Hövener. Molecular MRI in the Earth's Magnetic Field Using Continuous Hyperpolarization of a Biomolecule in Water. *The Journal of Physical Chemistry B*, 120(25):5670–5677, 2016.

[RKLG92] R. P. Robertazzi, R. H. Koch, R. B. Laibowitz, and W. J. Gallagher. $Y_1Ba_2Cu_3O_7/MgO/Y_1Ba_2Cu_3O_7$ edge Josephson junctions. *Applied Physics Letters*, 61(6):711–713, 1992.

[RNM+12] M. Rudolph, J. Nagel, M. Meckbach, M. Kemmler, M. Siegel, D. Koelle, and R. Kleiner. DC Superconducting quantum interferometers with asymmetric shunt resistors. *Applied Physics Letters*, 101, 2012.

[RRFE13] D. Rothfuß, A. Reiser, A. Fleischmann, and C. Enss. Noise thermometry at ultra low temperatures. *Applied Physics Letters*, 103(5):052605, 2013.

[Rud12] Matthias Rudolph. Asymmetrische dc SQUIDs. Diploma thesis, University of Tübingen, 2012.

[Rue08] Frank Ruede. *Hochempfindliche Stromsensoren auf DC-SQUID-Basis für den Betrieb in elektromagnetisch gestörter Umgebung.* PhD thesis, Technische Universität Berlin, 2008.

[S.A] S.A.R.L TSF, http://www.sarltsf.com/products/chemis/reny.html. *Glass-fiber-reinforced polyamide screws.*

[SCO+05] Katarzyna Suchanek, Katarzyna Cieslar, Zbigniew Olejniczak, Tadeusz Palasz, Nateusz Suchanek, and Tomasz Dohnalik. Hyperpolarized 3 He gas production by metastability exchange optical pumping. *Optica Applicata*, 35(2):263–276, 2005.

[Sep96] R. E. Sepponen. Low-Field MR Imaging – Development in Finland. *Acta Radiologica*, 37(3P2):446–454, 1996.

[Sig17] Sigma Aldrich, http://www.sigmaaldrich.com/catalog/product/aldrich/371254. *Sigma Aldrich Iron(III)Oxide hydrate catalyst*, 6 2017.

[SKSR37] L. V. Shubnikov, V. I. Khotkevich, Yu. D. Shepelev, and Yu. N. Ryabinin. Magnetic properties of superconducting metals and alloys. *Zh. Eksper. Teor. Fiz.*, 7:221–237, 1937.

[Smy67] William Ralph Smythe. *Static and dynamic electricity.* New York : McGraw-Hill, 3rd ed edition, 1967. Includes bibliographies.

[SR87] H. Seppa and T. Ryhanen. Influence of the signal coil on DC-SQUID dynamics. *IEEE Transactions on Magnetics*, 23(2):1083–1086, Mar 1987.

[Sta17a] Star Cryoelectronics, https://starcryo.com/wp-content/themes/education-pro/brochures/SQUID-Guide.pdf. *S-Series Low-T_c dc SQUIDs*, 5 2017.

[Sta17b] Star Cryoelectronics, www.starcryo.com. *STAR Cryoelectronics foundry service*, 2017.

[Ste68] W.C. Stewart. Current-voltage characteristics of josephson junctions. *Applied Physics Letters*, 12:277, 1968.

[Supa] Supracon AG, www.supracon.com. *Superconducting switch modell SW1.*

[Supb] Supracon AG, http://www.supracon.com/de /stromsensoren.html. *Various current sensors.*

[TC77] C. D. Tesche and J. Clarke. DC SQUID: Noise and optimization. *J. Low Temp. Phys.*, 29:301–331, 1977.

[TE 17] TE Connectivity Corporation, http://www.te.com/deu-de/product-2-1904058-5.html. *TE Connectivity 2-1904058-5*, 6 2017.

[tes17a] tesch-emc, http://www.tesch.de/english/durchfuehrungsfilter/html/000011-1. *Tesch 02000203*, 6 2017.

[tes17b] tesch-emc, http://www.tesch.de/english/durchfuehrungsfilter/html/000012-1. *Tesch 02000207*, 6 2017.

[Tex] Texas Instruments Incorporated, http://www.ti.com/product/LF398-N. *LF 398 monolithic sample and hold circuit.*

[Tin96] M. Tinkham. *Introduction to Superconductivity.* McGraw-Hill Inc., 2 edition, 1996.

[VAE+13] Denis Vasyukov, Yonathan Anahory, Lior Embon, Dorri Halbertal, Jo Cuppens, Lior Ne'eman, Amit Finkler, Yehonathan Segev, Yuri Myasoedov, Michael L. Rappaport, Martin E. Huber, and Eli Zeldov. A scanning superconducting quantum interference device with single electron spin sensitivity. *Nature Nanotechnol.*, 8:639–644, 2013.

[VeS17] *VeSPA - Versatile Simulation, Pulses, and Analysis.* https://scion.duhs.duke.edu/vespa/, 7 2017.

[VNZ+13] Panu T. Vesanen, Jaakko O. Nieminen, Koos C J Zevenhoven, Juhani Dabek, Lauri T. Parkkonen, Andrey V. Zhdanov, Juho Luomahaara, Juha Hassel, Jari Penttilä, Juha Simola, Antti I. Ahonen, Jyrki P. Mäkelä, and Risto J. Ilmoniemi. Hybrid ultra-low-field MRI and magnetoencephalography system based on a commercial whole-head neuromagnetometer. *Magnetic Resonance in Medicine*, 69:1795–1804, 2013.

[WM91] Richard P. Welty and John M. Martinis. A series array of DC SQUIDs. *IEEE Transactions on Magnetics*, 27(2 pt IV):2924–2926, 1991.

[WSB48] H W Woolley, R B Scott, and F G Brickwedde. Compilation of thermal properties of hydrogen in its various isotopic and ortho-para modifications. *Journal of research of the National Bureau of Standards*, 41(5):379–475, 1948.

[ZA14] Koos C J Zevenhoven and Sarianna Alanko. Ultra-low-noise amplifier for ultra-low-field MRI main field and gradients. *Journal of Physics: Conference Series*, 507(4):042050, 2014.

[ZMV+07] Vadim S Zotev, Andrei N Matlashov, Petr L Volegov, Algis V Urbaitis, Michelle A Espy, and Robert H Kraus Jr. SQUID-based instrumentation for ultralow-field MRI. *Superconductor Science and Technology*, 20(11):S367–S373, 2007.

[ZOM+10] Vadim S. Zotev, Tuba Owens, Andrei N. Matlashov, Igor M. Savukov, John J. Gomez, and Michelle A. Espy. Microtesla MRI with dynamic nuclear polarization. *Journal of Magnetic Resonance*, 207(1):78–88, 2010.

Danksagung

Abschließend möchte ich mich bei einigen Personen bedanken, durch die es zu einer sehr angenehmen und kurzweiligen Promotion gekommen ist.
Zu allererst möchte ich mich bei den beiden Chefs, Prof. Dieter Kölle und Prof. Reinhold Kleiner, bedanken. Durch das von Euch beiden entgegengebrachte Vertrauen in meine Arbeit bzw. in meine Arbeitsweise konnte ich sehr frei arbeiten und auch eigene Ideen verfolgen, wodurch ich einiges über SQUIDs lernen konnte. Dass man bei jeglichen Problemen, die bei der Arbeit auftauchen, immer völlig spontan und unförmlich bei Euch vorbei kommen konnte und ihr Euch immer direkt Zeit für die Anliegen genommen habt, schätze ich sehr.
Für die Sicherstellung der Kaffeebohnen- und Milchversorgung der gesamten Arbeitsgruppe, aber vor allem für die Abnahme von jeglichen bürokratischen und organisatorischen Angelegenheiten möchte ich mich besonders herzlich bei unserer Sekretärin, Marie-Luise Fenske, bedanken. Ohne mich zu weit aus dem Fenster zu lehnen kann ich vermutlich behaupten, dass die gesamte Arbeitsgruppe die selbe Meinung vertritt und allen bewusst ist, was Du für eine super Arbeit machst!
Auf technischer Seite nimmt Christoph Back in der Arbeitsgruppe eine vergleichbar wichtige Rolle ein. Deine Hilfsbereitschaft und fachliche Kompetenz macht Dich nicht nur für mich zu einem der wichtigsten Ansprechpartner innerhalb der Arbeitsgruppe, wenn es gilt technische Probleme jeglicher Art zulösen. Vielen Dank für deine Hilfe in vielen Belangen! Unbedingt müssen Manne und Helmut aus der Feinwerkstatt erwähnt werden. Die von Euch einwandfrei ausgeführte Fertigung von Bauteilen und Eure Flexibilität, wenn es mal zeitlich eng wurde und spontan was erledigt werden musste, war unerlässlich für meine Arbeit.
Als nächstes möchte ich meinem direkten Betreuer, Kai Buckenmaier, danken. Zum einen, dass Du mich auf das Niederfeld-Projekt geholt hast und weiter für die extrem angenehme Arbeitsatmosphäre und lustige, kurzweilige Zeit, die ständig im Labor vorherrschte. Diese war selbstverständlich nicht nur Kai zu verdanken, sondern auch den beiden anderen Mitgliedern der Niederfeld-Gruppe, Paul Fehling und Juri Rudin!
Ein herzliches Dankeschön möchte ich an das Team des Reinraumzentrums der PTB Braunschweig richten, welches für die Fertigung der SQUIDs verantwortlich war. Besonders richtet sich mein Dank an Judith Felgner, Rüdiger Wendisch, Thomas Weimann, Kathrin Störr und Viacheslav Mo-

rosh. Speziell möchte ich aber noch Oliver Kieler hervor heben. Das von Dir aufgebrachte, hohe Maß an Hilfsbereitschaft, Deine extrem akkribische Arbeit, sei es bei der Suche nach möglichen Fehlerquellen bei der SQUID-Herstellung oder die Flexibilität bei der Bearbeitung meiner Layouts waren wirklich eine sehr große Hilfe.
Meinen Kommilitonen und Freunden Andreas Pooch, Benedikt Ferdinand, Tobias Schwarz, Fabian Rudau, Benedikt Müller, vor allem aber Michael Augustus Gschwender und Matthias Körber danke ich für die vielen fachspezifischen, fachfremden, ernsten, sinnlosen und witzigen Diskussionen (auch bei dem einen oder anderen Bierchen) sowohl an als auch abseits der Uni!
Ein weiterer Dank gilt meiner Schwester und meinen Eltern, die mich stets moralisch [und meine Eltern auch finanziell;-)] unterstützt haben und damit wesentlich zum erfolgreichen Abschluss der Promotion beigetragen haben.
Zuletzt möchte ich mich bei meiner Freundin Jennifer bedanken. Deine Unterstützung während des gesamten Studiums und der Promotion sowie die schöne Zeit abseits der Uni ist unbezahlbar und bedeuten mir unendlich viel!